The Utilization of Templated Porous Electrodes in Electrochemical Applications

A DISSERTATION
SUBMITTED TO THE FACULTY OF THE GRADUATE SCHOOL
OF THE UNIVERSITY OF MINNESOTA
BY

Melissa Ann Fierke

IN PARTIAL FULFILLMENT OF THE REQUIREMENTS
FOR THE DEGREE OF
DOCTOR OF PHILOSOPHY

Andreas Stein, Advisor

September 2013

Acknowledgements

I would like to thank everyone who has helped me get to where I am today. I would not be here without all of the love and support offered by all. Extra special thanks to the following people:

My advisor, Andreas Stein. For your kindness, encouragement, support, understanding, and never-ending patience when I needed it the most. Thank you.

My (unofficial) second advisor, Philippe Bühlmann. You were also there for me from the very beginning (less than a month after I began working for Andreas in June 2006). I appreciate all of the help you provided, the unlimited access to your lab, and making me feel like part of your group.

Professor Bill Smyrl, for being generous with your time and knowledge, and for unrestricted access to your labs.

My Bühlmann group collaborators (and friends) Dr. Chun-Ze Lai and Dr. Eric Olson. It was truly a pleasure to work with both of you. Additional thanks are offered on the following pages.

My Stein group colleagues and friends. Dr. Nicholas Ergang, for passing along his battery project wisdom; Dr. Zhiyong Wang, for his generosity with his time and knowledge; Dr. Nicholas Denny, for the doses of reality when I needed them; Dr. Fan Li, for inspiring me to always do my best; Dr. Won Cheol Yoo, for English time; Dr. Matthew Dubay, for being a great friend; Dr. Anh Vu, for putting a smile on my face when I needed it; David Josephson, for the lab music and the laughs; Nicholas Petkovich, for his knowledge, friendship, and support; Yuqian Qian for always being there with a question; Stephen Rudisill, for giving me the opportunity to build Fort Passive-Aggressive; Benjamin Wilson, for being my early morning office buddy; and Lynne Johnsrud, for her support and encouragement.

The members of the Bühlmann group, for letting me traipse through the lab, use your equipment, pick your brains, and made me feel like a member of your group. I was lucky enough to have two graduate school families.

My Hamline University colleagues, for your friendship, encouragement, support, and patience.

My family and friends, for their encouragement and support through this process. I love you.

Special Acknowledgement for Chapter Three

The work in this chapter was completed during a multi-year collaboration with Chun-Ze Lai from Philippe Bühlmann's group. While my focus was the synthesis and characterization of the 3DOM carbon solid contacts as well as the electrochemical investigation of the sensors and related constructs, Chun-Ze prepared the sensing membranes, assembled the complete sensor constructs, and performed all of the detection limit and stability measurements. I would like to take this opportunity to thank her for her help in making this project a success for both of us. Without her, this work would not have been possible.

Special Acknowledgement for Chapter Four

The work in this chapter was completed as part of a collaboration with Eric Olson from Philippe Bühlmann’s group. My focus was the synthesis, modification, and characterization of the electrodes. Eric synthesized the electrolyte, and performed all of the square-wave voltammetry experiments. We worked as a team to do the rest of the electrochemical testing of the electrodes. I would like to thank Eric for all of his hard work making this project a success. I truly appreciate his help.

Abstract

The unifying theme within this work is three-dimensionally ordered macroporous (3DOM) carbon. This material consists of an ordered array of pores surrounded by a skeleton of amorphous carbon with nanometer-scale dimensions. 3DOM carbon offers several advantages that make it ideal for use in electrochemical applications. It has a high surface area, an interconnected pore structure, it is electrically conductive and chemically inert, the surface chemistry can be modified and characterized using slight modifications of well-established techniques, and robust monoliths can be produced. Here, 3DOM carbon was utilized in three distinct electrochemical applications.

A three-dimensional interpenetrating lithium ion battery with a 3DOM carbon anode and a mixed vanadia/ruthenia cathode was investigated. Optimization of the synthesis of the polymeric separator layer and the ruthenia component of the cathode were carried out. The synthesis conditions and post-synthesis treatment greatly affect the degree of ruthenia deposition within the porous structure and the extent of hydration of the product.

An ion-selective electrode system with 3DOM carbon as the solid contact was developed. 3DOM carbon was covered with an ionophore-based sensing membrane, allowing for selective detection of K^+ or Ag^+. This system exhibited very low detection limits (4.3 ppt for Ag^+), unprecedented electrode stability, and little-to-no response to common interferents (such as carbon dioxide and light). The reasons for this excellent performance were investigated using a variety of characterization methods (with an

emphasis on electrochemical techniques). The high surface area and low concentration of surface functional groups on 3DOM carbon are important factors.

A receptor-based sensor for explosives detection was also developed. The pore walls of 3DOM carbon were modified with a receptor for 2,4-dinitrotoluene (DNT) using a series of chemical and electrochemical modification steps. Only 3DOM carbon that had been modified with the receptor exhibited a response to the presence of DNT. This selective detection of DNT was also possible in the presence of interfering molecules. However, the high capacitance of the 3DOM carbon led to poor limits when using cyclic voltammetry as the detection method. When square wave voltammetry was used, which eliminates the capacitive currents, much improved detection limits (10 μM) were achieved.

Table of Contents

1. Introduction to Porous Carbon Electrodes

2. Optimization of a Ruthenia Cathode in an Interpenetrating Electrochemical Cell Utilizing Three-Dimensionally Ordered Macroporous Carbon as the Anode Material

3. Design and Investigation of Ion-Selective Electrodes with Three-Dimensionally Ordered Macroporous Carbon Solid Contact and Low Detection Limits

4. Receptor-Based Detection of 2,4-Dinitrotoluene Using Modified Three-Dimensionally Ordered Macroporous Carbon Electrodes

5. Summary and Outlook

List of Tables

List of Figures

Abbreviations and Symbols

2,4-DNT	2,4-dinitrotoluene
3DOM	three-dimensionally ordered macroporous
A	Ampere, SI unit of electrical current
AC	alternating current
AES	Auger-electron spectroscopy
AFM	atomic force microscopy
AMPD	2,2′-azobis-(2-methylpropionamidine) dihydrochloride
ATR	attenuated total reflectance
BET	Brunauer-Emmett-Teller
°C	degrees Celsius (centigrade temperature scale)
CPE	constant phase element
cryo-SEM	cryo-scanning electron microscopy
CV	cyclic voltammetry
CVD	chemical vapor deposition
CWE	coated-wire electrode
DNT	2,4-dinitrotoluene
E°	initial (electrical) potential
EDS	energy dispersive X-ray spectroscopy
EIS	electrochemical impedance spectroscopy
EMF	electromotive force

eV	electron volt
FTIR	Fourier-transform infrared spectroscopy
g	gram
h	hour
HOPG	highly oriented pyrolytic graphite
i.d.	inner diameter
ISE	ion-selective electrode
IUPAC	International Union of Pure and Applied Chemistry
K	Kelvins (Kelvin temperature scale)
KTFPB	potassium tetrakis[3,5-bis-(trifluoromethyl)phenyl]borate
LiOAC	lithium acetate
M	molarity (molar concentration in moles·L^{-1})
m	meter
MMA	methyl methacrylate
m (prefix)	milli ($\times 10^{-3}$)
min	minute
n (prefix)	nano ($\times 10^{-9}$)
NaTFPB	sodium tetrakis[3,5-bis(trifluoromethyl)phenyl]borate
NBu_4BArF_{24}	tetrabutylammonium tetrakis[3,5-bis(trifluoromethyl)phenyl]borate
NMR	nuclear magnetic resonance
o-NPOE	2-nitrophenyl octyl ether
PANI	poly(aniline)

PMMA	poly(methyl methacrylate)
POT	poly(3-octylthiophene)
ppb	parts per billion
ppm	parts per million
ppt	parts per trillion
PPO	poly(phenylene oxide)
PPy	polypyrrole
PS	poly(styrene)
PT	poly(thiophene)
PVC	poly(vinyl chloride)
RF	resorcinol-formaldehyde
S	siemens, SI unit of electric conductance
SAM	self-assembled monolayer
SC	solid contact
STM	scanning tunneling microscopy
SW	square wave
SWCNT	single-walled carbon nanotubes
SWV	square-wave voltammetry
TGA	thermogravimetric analysis
THF	tetrahydrofuran
V	Volt, SI unit of electrical potential
XPS	X-ray photoelectron spectroscopy

μ (prefix)	micro ($\times 10^{-6}$)
ω	natural frequency (related to frequency, f, by $\omega = 2\pi f$)
Ω	Ohm, SI unit of electrical resistance

Chapter One

Introduction to Porous Carbon Electrodes

1.1. Introduction

Carbon is perhaps the most unique and ubiquitous of all of the elements. In addition to being the basis of a vast majority of all known compounds,[2] pure carbon exists as many widely varying allotropes, each with their own unique physical properties. Carbon is widely used in electrochemical applications because of its advantageous physical properties, including good electrical and thermal conductivity, a low density, low thermal expansion, low elasticity, resistance to corrosion, as well as its availability in a wide variety of structures in high purity at low cost.[3] An additional advantage of using carbon materials is the ability to tune its chemical and physical properties based on the desired properties for a specific application. This can be accomplished with the addition of porosity, either during or after carbon synthesis, or by changing the surface chemistry of the materials. The surface chemistry of carbon can be modified by altering the carbon precursor used, changing processing conditions, or functionalizing the surface post-synthesis.

Creating porous carbon materials provides a wide variety of desirable physical properties, including high surface area, large pore volume, nanoscale dimensions of pore walls, and the ability to tailor pore size, shape, and connectivity.[4-6] Carbon materials can be synthesized with a wide variety of pore sizes using many different strategies. Pores have been classified according to their width by the International Union of Pure and Applied Chemistry as micropores (<2 nm), mesopores (>2 nm, <50 nm), and macropores (>50 nm).[7] The pores within carbon materials can be ordered or disordered, depending on the synthesis method utilized. Disordered microporous carbons can by synthesized directly by pyrolysis of carbon precursors. The pore size can be controlled by altering the composition of the precursor.[8,9] Ordered microporous carbon materials have been made using zeolites as templates.[10] Mesoporous carbon materials are synthesized using several methods, including filling the void space within mesoporous hard templates (typically silica or other inorganic templates) with carbon precursors, including liquid carbon precursors or by chemical vapor deposition of volatile precursors.[11,12] The carbon precursor is then converted into carbon, followed by removal of the template.[13] Mesoporous carbon materials can also be synthesized using organic (soft) templates, including surfactants, block copolymers, polymers, and large molecules.[5,14,15] The template is burned out during the conversion of the precursor to the final product, eliminating the extra template removal step. Macroporous carbon is typically synthesized using an ordered array of spheres as a template (described in detail below), which produces ordered macroporous materials, or by inducing macrophase separation, which produces disordered, bicontinuous macroporous materials.[13,16]

An example of a carbon material that is being investigated for many electrochemical applications is three-dimensionally ordered macroporous (3DOM) carbon. This material has a designed porosity, can be easily functionalized, and can be synthesized as robust, monolithic pieces. 3DOM carbon also offers the unique advantage of an interconnected pore structure that can be filled with another phase, which allows for its use in electrochemical applications that benefit from high interfacial surface areas between phases. Because of these advantages, 3DOM carbon was investigated for several electrochemical applications in this work. The effect of altering synthesis conditions on the physical properties of 3DOM carbon (including conductivity and surface area) are investigated to allow for optimization of the carbon used for the electrochemical applications. The improvement of the conductivity of the cathode material in an interpenetrating lithium ion battery with 3DOM carbon as the anode is attempted. This system would allow for more power per unit area by utilizing the third dimension of the battery. In addition, 3DOM carbon is used as the electrode in two different types of electrochemical sensors. An ion-selective electrode system with carbon serving as a solid contact in a sensing membrane system is developed. This system shows an unprecedented detection limit for one of the analytes studied, in addition to being the sensor system with the most stable signal yet reported. The reasons for this remarkable performance as they relate to the surface chemistry and architecture of the 3DOM carbon solid contacts are investigated. In addition, an electrochemical receptor-based sensing system for explosives was developed. The receptor-based system allows for selective detection of the analyte of interest, even in the presence of common interferents.

1.2. 3DOM Materials

Three-dimensionally ordered macroporous (3DOM) materials consist of an ordered array of interconnected, macroporous spherical voids, typically with diameters of several hundred nanometers, surrounded by a solid skeleton. 3DOM materials are produced by colloidal crystal templating, in which the template consists of an ordered array of spheres. The most common templating materials include poly(styrene) (PS), poly(methyl methacrylate) (PMMA), or silica spheres.[17]

After synthesis, the spheres are typically suspended in a solvent. To make a usable template, the spheres must be ordered, and the solvent must be removed. There are several methods of ordering the spheres, including gravity sedimentation, centrifugation, vertical deposition, template deposition, electrophoresis, controlled drying, filtration, and deposition in confined spaces.[17-20]

During the synthesis of 3DOM materials, the interstitial space between the spheres of the template is filled with a precursor. During or after conversion of the precursor to the desired material, the template is removed. Polymer spheres are typically removed by combustion or dissolution, while silica is removed by etching with HF or NaOH.[21] Elimination of the template leaves solid walls surrounding the spherical voids, as shown in Figure 1.1. The walls are typically tens of nanometers thick, while the voids are usually several hundred nanometers in diameter, depending on the sphere size of the colloidal crystal used.

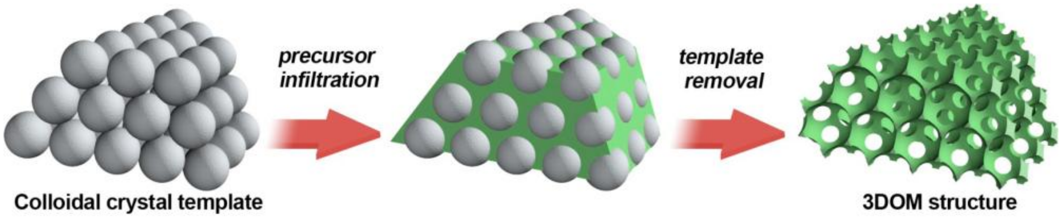

Figure 1.1. Schematic of the synthesis of 3DOM materials. A colloidal crystal template is infiltrated with a precursor material, the precursor is converted to the final product, and the spheres are removed to yield the final 3DOM structure. Figure adapted and reproduced with permission from Stein *et al.*[21] Copyright American Chemical Society 2008.

The techniques used to synthesize 3DOM materials are quite versatile, with many different compositions and morphologies possible. The materials synthesized by this technique include oxides,[22-32] non-oxides (e.g. carbon),[33-38] metals,[30,39-44] semiconductors,[33,45,46] polymers,[33,47-49] hydrogels,[50-52] and composites.[26,53-56] Depending on the template and preparation technique, 3DOM materials can be made in the form of powders,[45,53,57] thin films,[42,58-61] monoliths,[62-66] rods,[67,68] and nanosheets.[69]

3DOM materials have generated a lot of interest since they were first introduced.[25,27,34] The structures typically have open, highly periodic structures with large surface areas. In addition, the nanoscale dimensions of the pore walls lead to unique properties that have led to 3DOM materials being investigated for a wide range of applications. These applications include photonic crystals,[27,70-72] pigments,[53,73-75] sensors,[51,53,76-78] catalysis,[79,80] and electrochemical applications.[35,66,81-84]

1.3. Carbon

1.3.1. Synthesis of 3DOM Carbon

Carbon materials prepared with designed pore architectures, such as 3DOM carbon, can be prepared by several methods, typically by infiltrating a template with a carbon precursor. A common technique is to infiltrate a template composed of ordered silica or polymer spheres with precursors such as sucrose, [85] phenolic resin,[34,86] phenol-formaldehyde,[87] resorcinol-formaldehyde,[56,63] or mesophase pitch.[36] Additional methods utilizing sphere templates include melting and cyclopolymerizing arene monomers into the template,[76] chemical vapor deposition (CVD) of propylene,[34] chemical vapor infiltration of methane,[88] polymerization of phenol and formaldehyde initiated by acidic sites on a silica template,[89] and carbonization of a polystyrene and silica sphere composite (with the polystyrene acting as the template and carbon source, and small silica spheres acting as mesopore templates).[90] Macroporous silica templates (with or without mesoporous walls) are also used as templates for macroporous carbon. Synthesis methods include infiltration of the template with sucrose,[91] benzene CVD,[35] polymerization of phenol and paraformaldehyde initiated by acidic sites on the template,[92] and polymerization of divinylbenzene inside the mesopores of a macroporous/mesoporous silica template.[83]

Macroporous carbon materials without uniform, ordered macropores have also been synthesized. A porous silica or polymer template can be infiltrated with carbon precursors such as furfuryl alcohol,[93-95] and mesophase pitch.[96] Additional methods include subjecting a resorcinol-formaldehyde gel to ultrasonic radiation,[97] preparation of resorcinol-formaldehyde gels with an acid catalyst (instead of the typical base catalyst),[98] and infiltration of diatoms with sucrose.[99]

1.3.2. Synthesis of Carbon from Resorcinol-Formaldehyde

Amorphous carbons are typically synthesized by heating carbon precursors in an inert atmosphere. As mentioned above, a wide variety of precursors can be used to synthesize carbon materials. In this work, resorcinol-formaldehyde was the carbon precursor used because of its ease of use in a template system, and the ability to tune the properties of the carbon with simple alterations of the multi-step synthesis procedure. A highly porous aerogel is first formed by the sol-gel polymerization of resorcinol with formaldehyde in the presence of a catalyst, followed by aging of the gel. The gel is then dried. Depending on the drying conditions, an aerogel (a gel in which the liquid is removed without collapse of the pore structure, leaving a low density, highly porous material) or a xerogel (a gel in which the pore structure collapses, leaving a material with a higher density and much less porosity) is formed.[100] The gel is then converted into the corresponding carbon product (aerogel or xerogel) by carbonization (also known as pyrolysis), which is the process of heating the gel in an inert atmosphere.

1.3.2.1. Gel Formation and Curing

Resorcinol-formaldehyde organic gels were first synthesized by Pekala.[101] Resorcinol (1,3-benzenediol) is combined with formaldehyde (typically in a 1:2 ratio) in the presence of a catalyst. Common solvents include water, acetone, or alcohols. The catalyst activates the resorcinol, allowing addition of formaldehyde molecules in the 2-, 4-, or 6-positions on the ring in an addition reaction, forming hydroxymethyl derivatives.[102] These hydroxymethyl derivatives then undergo condensation reactions to form methylene and methylene ether bridged compounds (Figure 1.2). During the synthesis, small (7 to 10 nm) cross-linked polymer clusters form, followed by aggregation of the clusters into an interconnected structure. [102-104] The mixture must be heated during the gelation process (typically to about 80 ºC) to allow the endothermic polymerization reaction to take place. Small changes in the synthesis conditions greatly affect the structure of the gel.

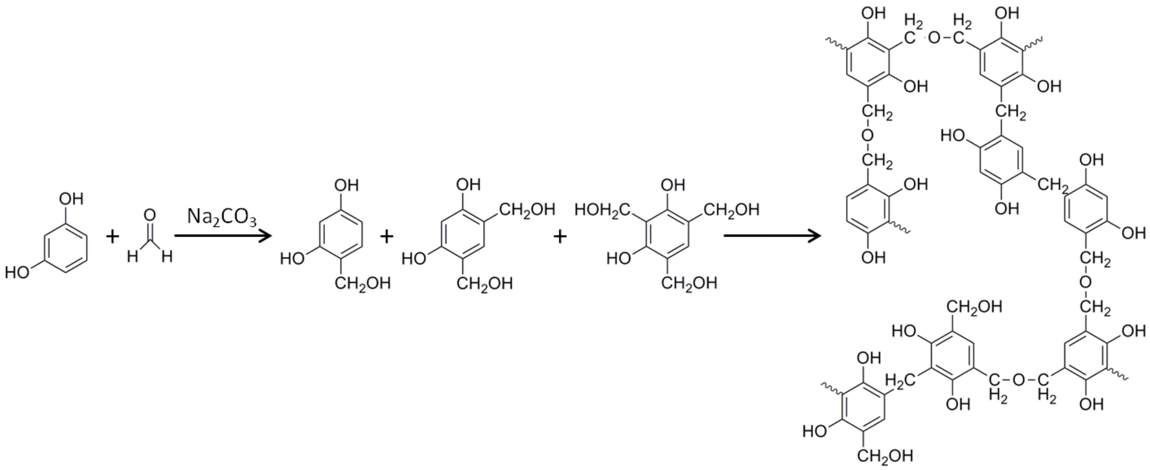

Figure 1.2. Synthesis scheme of resorcinol-formaldehyde precursor for carbon synthesis. Resorcinol and formaldehyde undergo an addition reaction to form hydroxymethyl derivatives, followed by condensation reactions which form methylene and methylene ether bridged compounds. Figure redrawn and reproduced with permission from Pekala, *et al.*[105] Copyright American Chemical Society 2003.

When the concentration of the precursors is decreased in the solution, gels with larger pores and more pore volume tend to form. This leads to an increase in the mesopore surface area of the gel. During the synthesis, small particles form before aggregating. If the concentration of precursors is low, there is more space between the aggregated particles, resulting in larger pore sizes. The lower precursor concentration also causes a decrease in the micropore surface area of the gel due to the formation of larger pores.[106,107] In addition, the concentration of precursors affects the homogeneity of the gel, with high precursor concentrations leading to homogeneous gels, and low precursor concentrations leading to inhomogeneous gels.[108,109] Higher precursor concentrations are also more likely to produce monolithic gels.[110]

The polymerization can occur with either an acid or base catalyst. If an acid catalyst is used with a low concentration of precursors, small, fractal aggregates of particles are formed that have a very high pore size distribution. However, if a high precursor concentration is used, no fractal aggregates are formed, and the pore size distribution is very narrow. In addition, the gelation time is reduced.[104,111] Base catalysts (especially sodium carbonate) are much more commonly used. Ratios of resorcinol to catalyst are typically between 50 and 300. With high catalyst concentrations, the gels formed are polymeric (composed of small network clusters), highly interconnected, have a high mechanical strength, and form quickly. If low catalyst concentrations are used, the gels tend to be colloidal (with large polymer clusters), which leads to low surface areas and mechanical strength.[104,108,112,113] The highest surface area is achieved with a resorcinol to catalyst ratio of 50, and the surface area continuously decreases if the ratio is increased.[114]

The catalyst concentration of the catalyst in the solution is used to control the pH of the solution, which has a major effect on the gelation behavior.[115] If the pH is too low, the reactants can precipitate.[101] If the pH is too high, the condensation reaction is hindered.[116] As a result, syntheses are typically carried out in a pH range of 5.4 to 7.6.[104] The pH of the gel also greatly affects the properties of the product. If the pH is increased, the surface area and pore volume of carbon aerogel products are increased. However, increasing the pH does not affect the surface area of carbon xerogels.[117]

After gel formation, the gel must be cured by heating, typically at the same temperature at which it was gelled (80–90 ºC), for several days. This process strengthens the gel by increasing the cross-linking between the small polymer particles.[104] The time necessary for the cross-linking process can be decreased by aging the gel in acid instead of the original solvent.[118]

1.3.2.2. Gel Drying

After gel formation and curing, the polymer gels must be dried before they are converted to carbon gels. Depending on the drying method and the product desired, solvent exchange may be used prior to drying in order to reduce the surface tension. If water was used as the solvent for the gelation process, it is typically replaced with an organic solvent by soaking the gels in fresh solvent several times.[101] This allows the gels to be dried without a collapse of the pore structure due to large changes in the surface tension of the solvent while drying, as typically occurs when drying gels that contain water. There are several common methods for drying gels, which each have advantages and disadvantages.

In subcritical drying, the gels are dried by directly evaporating the solvent from the wet gel, either under vacuum or at atmospheric pressure. However, this process causes large changes in the surface tension of the solvent, which leads to mechanical stresses in the gels. This stress causes the pore structure of the gel to collapse, leaving a dense xerogel.[119] The rate of drying affects the texture of the dried gels and the resulting carbon product.[120] Cracking of the gels can also occur. While this process cannot be used to synthesize an aerogel, if a xerogel is the desired product, subcritical drying is fast and inexpensive.[104]

If an aerogel is the desired product, supercritical drying, typically with CO_2, is necessary. The gels first undergo solvent exchange in which the solvent is replaced with a solvent that is miscible with liquid CO_2 (typically acetone). The new solvent is replaced by liquid CO_2, which is then converted into supercritical CO_2 before removal. The low surface tension of CO_2 allows drying of the gel without collapse of the pore structure. Supercritical drying does not completely eliminate gel shrinkage, but minimizes it, especially compared to subcritical drying techniques.[120] This process requires high pressures, takes several days, and is expensive.[106,121]

In order to alleviate some of the issues with drying using supercritical CO_2, supercritical acetone has also been utilized.[121] The same procedure as for supercritical CO_2 is used, but supercritical acetone is used instead. In this method, the solvent does not need to be replaced with liquid CO_2, and lower pressures can be used, meaning the process is much quicker. However, high temperatures are required to achieve supercritical acetone, which may cause partial pyrolysis of the gel.[121] In addition, the gels can shrink, leading to a product with a higher density.[104,121]

Ambient drying is an inexpensive method that produces similar results to supercritical drying. In this method, the solvent in wet gels is exchanged with acetone due to its low surface tension and low boiling point.[122] After complete solvent exchange, the acetone is allowed to evaporate until a dry gel is achieved. The amount of shrinkage during drying is comparable to that of supercritical drying.[123]

Another drying method used to avoid the mechanical stresses created by solvent evaporation is freeze-drying. After solvent exchange with a liquid that has a low density change upon freezing, such as *tert*-butanol, the wet gel is frozen.[124] The solvent is then removed by sublimation. This method does not completely eliminate gel shrinkage, but instead greatly reduces it, creating products that are typically mesoporous.[125]

1.3.2.3. Gel Carbonization/Pyrolysis

During pyrolysis (term used interchangeably with carbonization), the dried gels are heated under a flow of inert gas to an elevated temperature, usually between 600 and 900 ºC.[108,112] During heating, the gel is converted into carbon as most of the remaining oxygen and hydrogen atoms are removed. As a result, the gel shrinks during the carbonization process, typically up to a maximum of 50% shrinkage.[104,126] While the synthesis and drying steps control the formation of mesopores and macropores, micropores are almost exclusively formed during the pyrolysis process.[108,114] In this process, organic functional groups typically containing carbon, hydrogen, and oxygen are lost as small molecules, resulting in the formation of new micropores or enlargement of existing pores.[104,127,128] During pyrolysis, C–H and C–O bonds are broken to release the small, volatile molecules, and C–C bonds form in their place.[116,129] The volume and surface area due to micropores greatly increase during pyrolysis between 400 °C and 750 °C, after which structural changes take place in the material with little weight loss.[114,127,128] In addition to the micropore formation, the mesopore volume decreases during carbonization due to the shrinkage of the mesopores in the gel.[130]

The carbonization temperature greatly affects the properties of the resulting carbon material. Increasing the pyrolysis temperature reduces the oxygen content of the carbon formed. In addition, as the temperature is increased, the surface area and pore volume of the product is decreased, regardless of whether the starting material was an aerogel or a xerogel.[104,117] The electrical conductivity of the carbon product also depends on the carbonization temperature. The carbon does not become conductive unless the carbonization temperature is high enough, typically above 650 ºC. Once the carbon becomes conductive, the conductivity continues to increase as the carbonization temperature increases.[126]

1.3.3. Structure of Carbons from Resorcinol-Formaldehyde

While many carbon allotropes are composed of only carbon atoms, they exhibit very different physical properties dictated by the type of bonds between the carbon atoms. Diamond contains solely 4-coordinate sp^3-hybridized carbon atoms, leading to a hard, electronically insulating material. In contrast, graphite is a stack of graphene sheets (one-atom thick sheets of 3-coordinate sp^2-hybridized carbon atoms), leading to a soft, electronically conducting material. Fullerenes, such as Buckminsterfullerene (C_{60}), are closed-cage molecules consisting of 3-coordinate carbon atoms. However, due to the curved shape of the molecules, the coordination is non-planar and the hybridization is a mixture of sp^2 and sp^3.[131,132] Carbon nanotubes can be envisioned as stretched fullerenes or rolled up graphene sheets with fullerene-like end caps, and have very similar properties to fullerenes.[131-134] Both fullerenes and carbon nanotubes can be a single layer (one atom thick) or multi-layered (concentric shells or tubes), and are known as carbon onions and multi-walled carbon nanotubes, respectively.[131,133]

The structure of carbon prepared from resorcinol-formaldehyde precursors is typically described to be amorphous.[112] While the allotropes of carbon described above have well-defined structures and contain almost exclusively carbon atoms, amorphous carbon can have a widely-varying structure, and often contains atoms besides carbon. The edges of the graphene sheets are typically terminated with hydrogen or other functional groups, leading to sp^2 and sp^3 hybridization of carbon atoms in amorphous carbon.[3,135] Many structures have been proposed for amorphous carbon, but none have been universally accepted.[136] Amorphous carbons are typically composed of small, randomly arranged crystallites containing a few parallel graphene sheets (typically two or three), thus exhibiting short range order but no long range order.[2,3,137] This structure has also been compared to a ‘house of cards’ constructed of single graphene sheets.[138] Amorphous carbons have a varying degree of single graphene sheets, depending on the preparation method.[138] This random arrangement of graphene sheets leads to a lower density in amorphous carbons than in graphite. Graphite has a density of 2.25 $g \cdot cm^{-1}$, while that of amorphous carbon is approximately 1.88 $g \cdot cm^{-1}$.[3] Like graphite, amorphous carbon is also electronically conducting, although not to the same extent.[3]

1.3.4. Functionalization of Carbon Materials

The presence and quantity of functional groups on the surface of carbon materials depends on the precursor materials and preparation method of a particular sample. These surface groups can have a large effect on the properties of carbon, including hydrophobicity/wettability, catalysis, adsorption, electrical properties, and chemical reactivity.[3,139-142] Being able to characterize and modify the surface of carbon materials allows for control of the behavior of the sample and improvement of specific properties for applications.

The surface of carbon can include functional groups that contain oxygen, hydrogen, nitrogen, sulfur, halogens, etc., depending on the precursors used and the processing conditions.[3] The functionality of the carbon can be greatly altered by modification of the carbon surface by a wide variety of methods.

1.3.4.1. Activation

After carbonization of the aerogel or xerogel to produce a carbon material, additional surface area and surface functionality may be induced by surface activation. Activation can be divided into two categories: physical and chemical activation. Physical activation involves heating a sample of carbon in a non-inert atmosphere, such as CO_2, O_2, air, steam, or a combination of the above.[98,128,129,143-147] Chemical activation involves pyrolysis of the carbon precursors in the presence of chemical agents capable of activation, such as KOH and $ZnCl_2$.[148-150] A combination of chemical and physical activation may be used to further increase the surface activation.[151,152] It is also possible to catalytically activate the carbon surface by adding metal salts or organometallic compounds to the carbon precursors.[153-155]

1.3.4.2. Introduction of Functionalization During Synthesis

Depending on the carbon precursor used, carbon samples typically contain carbon, hydrogen, and oxygen. Additional atom types can be incorporated by selecting precursors with other heteroatoms. For example, nitrogen containing carbon can be produced by selecting a nitrogen containing precursor, such as polypyrrole.[156]

1.3.4.3. Post-synthesis functionalization

1.3.4.3.1. Oxidation

To increase the number of functional groups on the surface, oxidation is a popular method of surface modification as it can be controlled quite well depending on the conditions. Oxidation introduces oxygen-containing functional groups to the surface of carbon samples. These functional groups may be acidic or basic in nature. Examples of acidic oxygen-containing functional groups are hydroxyl, carboxyl, carbonyl, lactone, ether, and acid anhydride groups.[135,157,158] Basic surface oxygen-containing functional groups are not well understood.[157] The identities and quantities of the functional groups can be controlled by the choice of oxidant, as well as the concentration, temperature, and duration of oxidation.[140,159,160]

A common oxidizing agent for carbon is nitric acid.[141,146,161-164] Nitric acid is widely used because it produces a large amount of surface oxygen groups, and it is controllable. By increasing the oxidation time, oxidation temperature, or concentration of nitric acid, the number of oxygen containing functional groups is increased.[141,162,165] Examples of other oxidation methods include oxidation by ozone at 300 K, which can produce carboxyl groups (in addition to other oxygen-containing groups) without the involvement of water in the functionalization.[166] Oxygen plasma can also be used for introducing oxygen groups, but functional groups are only produced on the external surface of the sample.[161] Hypochlorite ions are a milder oxidant than nitric acid, allowing much more control over the number and type of functional groups on the surface.[162] Other possible oxidants include hydrogen peroxide, ammonium persulfate, bichromate, and permanganate.[159,162,163] In addition to chemical oxidation, carbon surfaces can also be oxidized electrochemically,[167,168] including oxidation of carbon with patterns by utilizing scanning electrochemical microscopy.[169]

1.3.4.3.2. Introduction of Other Functional Groups

Nitrogen atoms can be added to carbon surfaces by nitrogen plasma treatment, which produces a hydrophilic surface.[170] Nitrogen can also be added to the carbon surface by reaction with ammonia at elevated temperatures.[171-174] These treatments produce a wide variety of nitrogen-containing functional groups, including pyridine, amine, amide, pyrrole, lactam, etc.[171] The presence of nitrogen atoms increases the catalytic activity of the samples.[172,173] The addition of nitrogen atoms by reaction with ammonia also creates basic sites on the surface of the carbon materials.[174]

Sulfonation (addition of –SO_3H functional groups) can be achieved by treatment of carbon in concentrated sulfuric acid, typically at elevated temperatures.[175,176] Sulfonic acid groups may also be produced by contacting carbon materials with the vapor of fuming sulfuric acid.[177] Many sulfur-containing groups (including SO_3, SO_3H, SO_4, and SO_4H groups) can be created by treating carbon with a SO_2 or SO_2/H_2O plasma.[178]

Chemical methods may also be used to introduce halogens onto the surface of carbon materials. Fluorination of the surface can occur by reaction with diluted fluorine gas at various temperatures.[179] Carbon materials have been functionalized with fluorosilanes or Teflon-like coatings, in order to produce hydrophobic surfaces.[180,181] In addition to fluorinating, it is possible to chlorinate the surface of carbon. When heating carbon samples in the presence of chlorine gas, chlorine atoms replace hydrogen atoms on the carbon surface.[182-184] A similar reaction also occurs in the presence of bromine.[172]

Carbon surfaces without existing functionality can be modified by the reduction of diazonium salts on the surface of the carbon. This reduction occurs via chemical[185,186] or electrochemical[187-192] methods. During this process, the diazonium salt undergoes a one-electron reduction, followed by the formation of a covalent bond with the carbon surface.[188] In the chemical reduction method, the diazonium salts are prepared in situ, and the carbon reduces the diazonium species.[185,186] The diazonium salts used are typically aryl diazonium salts which contain a wide variety of functional groups in the para position to the diazonium group, such as nitro, cyano, carboxy, benzoyl, bromo, and carboxymethly groups.[187,188] This allows simple reduction chemistry to be used to generate many different surface functionalities. After attachment of the aryl ring to the carbon surface, the functional groups can be modified further (chemically or electrochemically) if necessary, to create the desired functionality.[187,188,192] The functional groups created by this process are stable over a wide potential range, permitting their use in electrochemical applications.[189]

Additional functional groups can be chemically attached to carbon surfaces, either by reacting molecules with the functional groups that exist after synthesis, or with those added during a prior functionalization step. For example, after fluorescein derivatives are attached to hydroxyl groups present on the surface of a carbon sample, Raman spectroscopy is used to study the distribution of hydroxyl groups present.[193] Carbon materials with hydroxyl groups present are also reacted with amines (such as 3-chloropropylamine) to directly produce amino ($-NH_2$) functionalized carbon.[194] Another method to produce amino groups involves nitrating a carbon surface, followed by chemical reduction of the nitro groups to produce amines.[195,196] The amines can then be reacted with carboxylic acids, forming amide bonds with other molecules with additional functional groups present.[196] Amide bonds are also formed by reacting amines, including diamines and polyamines, with surface bound carboxylic acid functional groups,[197-199] or by conversion of carboxylic acids to acid chloride groups, followed by reaction with amines.[200] Hydrophobic carbon surfaces are produced by reacting silane molecules with existing surface functional groups.[201]

A wide variety of surface functionalities are produced by reaction of small molecules with the localized double bonds within the carbon structure. Molecules can be directly added across a double bond using a simple microwave synthesis.[202] After addition of bromine across double bonds using wet chemical techniques, further modification occurs by substitution of the bromine atoms by molecules of interest.[202]

While most of the above functionalization techniques have been carried out on glassy carbon or activated carbon, similar techniques have been applied to porous materials with designed pore architectures,[1,203] including 3DOM carbon.

1.3.5. Characterization

A wide variety of characterization techniques are used to identify and quantify the functional groups present on the surface of carbon materials. One of the first and most popular methods for quantifying surface functional groups is acid-base titration. In this method, acidic functional groups are titrated with bases of varying strengths to determine the types and amounts of the various oxygen-containing functional groups present on the surface of the carbon.[135,157,165,204] Since the titration method of surface functionality determination was first detailed,[135] there have been several attempts to standardize all aspects of the procedure.[205,206] In addition, efforts have been made to compare the results of the titration method with other methods surface characterization.[140,207] Other titration methods include mass titration to determine the point of zero charge,[144,157,165,208] and potentiometric titration to determine the quantities of acidic and basic sites on the carbon surface.[171,207,209]

Spectroscopic techniques are also widely used. X-ray photoelectron spectroscopy (XPS), including traditional XPS and synchrotron based XPS, are used to determine the identities and amounts of surface functional groups.[144,168,171,210-212] In addition, XPS can be used to identify specific surface functional groups after derivitization with an atom that is easily identifiable using XPS.[197] A related technique, Auger-electron spectroscopy

(AES), is also used.[168] Several types of infrared spectroscopy are used, including Fourier-transform infrared spectroscopy (FTIR),[166,211] attenuated total reflectance (ATR) FTIR,[213] and diffuse reflectance FTIR.[159,207] Raman spectroscopy (sometimes after derivitization of the surface functional group of interest) is also used.[193,212,214]

A variety of microscopy techniques are also used. Examples include scanning tunneling microscopy (STM),[168] phase-contrast imaging in tapping-mode atomic force microscopy (AFM) to detect oxygen-containing functional groups,[215] and electron microscopy after surface decoration.[3]

Other characterization techniques include thermal desorption and quantification of functional groups (typically as CO, CO_2, and H_2O) using thermogravimetric analysis or temperature programmed desorption coupled with mass spectrometry,[144,157,204,207,210,211] ammonia adsorption-desorption to quantify the acidic functional groups,[204] calorimetry to determine the heat of neutralization of surface functional groups,[157,210] zeta potential measurements,[171] mercury porosimetry,[211] cyclic voltammetry to qualitatively and quantitatively investigate the functional groups on the carbon surface,[139,164] laser desorption/ionization mass spectrometry to verify the presence of surface functional groups,[197] dye adsorption to determine acidic functional groups,[198] determination of the isoelectric point of carbon materials by measuring their electrophoretic mobility while titrating with acid or base in an electrophoresis cell,[216] and elemental analysis.[144,207]

1.4. Electrochemical Applications of Carbon Electrodes

Carbon materials have previously been examined for electrochemical applications, including capacitors,[150,217,218] electrocatalyst supports,[35,89] sensor electrodes,[219] and battery electrodes.[35,220,221] Carbon aerogels and xerogels are ideal for these applications because of their monolithic shape, high surface areas, and electrical conductivity.[103] Monoliths have been shown to have a higher conductivity and capacitance than powdered carbon samples compacted into pellets.[222]

Most electrodes utilized in electroanalysis applications, including sensors, have employed flat, non-porous electrodes. However, interest in porous electrodes or porous films on flat electrodes is increasing. Porous electrodes provide many advantages, including increased surface area (providing a higher electrode/electrolyte interface, as well as an increase in reactive sites and sensitivity, which can lead to lower detection limits), enhanced mass transfer (of both the electrolyte and substrate), and a well-interconnected pore structure (allowing for effective charge transport).[223] In addition, the porous structure allows for the hosting of reactants, receptors, etc.

Carbon as a porous electrode provides several advantages over other materials (such as metals and silica), including electrochemical conductivity (allowing direct use as an electrode, instead of preconcentration of the sample followed by characterization with another technique), stability in a wide range of system/electrolyte conditions (including extreme pH conditions), ease of synthesis and surface functionalization, and long term durability. A few electrochemical applications with porous carbons as the electrode are discussed below.

1.4.1. Capacitors

In electrochemical capacitors (also called supercapacitors), charge is stored at the electrode/electrolyte interface.[224] Possible electrode materials for electrochemical double layer capacitors must meet several requirements, including high surface area, reasonable electrical conductivity and polarizability, and lack of participation in faradaic reactions.[103] Carbon materials appear to meet all of these requirements. The capacitance of many types of carbon has been examined, including carbon black, aerogels, fibers, glassy carbon, and nanostructured (including micro-, meso-, and/or macroporous) carbons.[66,103,225-228] The size and shape of the pores greatly influence the capacitance and rate performance, especially at high rates.[90,147] The capacitance of carbon materials is typically measured by electrochemical methods including cyclic voltammetry, electrochemical impedance spectroscopy, and galvanostatic cycling. The electrolytes used to measure the capacitance of carbon materials can be aqueous (acidic, basic, or neutral) or organic solutions.[229]

The functionalization and activation of the carbon surface can have a major effect on the specific capacitance. Oxidation of carbon samples, which produces hydroxyl and carboxylic groups on the surface, leads to higher specific capacitances than unoxidized carbons due to the development of pseudocapacitance and enhanced wettability of the carbon surface by aqueous electrolytes.[230,231] While a higher concentration of acidic surface groups increases the total capacitance, it also impedes the ion penetration into pores during charge and discharge of the capacitor.[232]

Other factors besides pore size and functionality affect the capacitance, including the wettability of the carbon by the electrolyte solution, conductivity, and device configuration.[233] For example, after modification by a hydrophobic surfactant, activated carbon exhibited improved wetting of the surface with the electrolyte solvent, leading to lower resistance and more surface area usage. These electrodes have higher capacitances, even at higher rates, than unmodified electrodes.[234]

1.4.2. Electrocatalyst Supports

The high surface area of porous carbon materials makes them an ideal catalyst support.[3] A variety of catalyst systems have been prepared, including supporting 2–3 nm Pt/Ru nanoparticles on porous carbon for use in methanol oxidation.[89] The porous carbon system outperformed two systems with the same nanoparticles supported on commercial carbon materials by up to 60%. A similar system with 6 nm Pt particles supported on a graphitic ordered carbon also outperformed a commercial carbon/Pt catalyst with the same Pt loading.[35] Macroporous and macro/mesoporous carbon has also been used to support Mo, Co, and CoMo catalysts for use as a hydrodesulfurization catalyst.[235] Both systems had better conversion and selectivity than systems that utilized activated carbon or alumina as the catalyst support.

1.4.3. Batteries

Batteries are electrochemical cells that are used for chemically storing and then regenerating electrical energy.[236] They consist an anode and cathode (negative and positive electrodes, respectively), as well as an electrolyte that allows for ionic conductivity and electronic insulation between the electrodes. Batteries are typically classified as primary (one-time use) or secondary (rechargeable). The careful selection of appropriate anode and cathode materials dictates the properties of the battery system.

1.4.3.1. Lithium Ion Batteries

Lithium metal possesses several characteristics that make it appealing as an anode. It is the lightest metal, which leads to a lightweight battery, and it also has a very high electrochemical reduction potential. Together, these features should provide an electrochemical cell that has a high specific energy.[236] Primary lithium cells have been widely used. There is considerable interest in using lithium as the anode in secondary batteries as this system would provide a high cell voltage and high specific energy.[224] However, there are several factors that prevent the use of lithium as an electrode for secondary batteries. When the battery is recharged, the lithium tends to replate unevenly which causes dendrites to grow as the number of recharges increases. These dendrites lead to short circuiting of the cell which can cause fires and battery failure.[236]

Lithium ion batteries seem to be a promising alternative to lithium batteries. The groundwork for Li ion batteries was laid when researchers at Oxford discovered that Li^+ could be intercalated into materials in the 1970s.[236] Intercalation is the reversible insertion of an ion into a host material.[237] In addition to the safety advantages over Li metal batteries, Li ion batteries also have other characteristics that make them attractive for use in applications. They have high gravimetric and volumetric energy densities, a high operating voltage, and excellent charge/discharge characteristics with a low self-discharge. Also, rapid recharging is possible, and the batteries do not suffer from memory effects like some other rechargeable battery systems do.[236]

Carbon is often used as an intercalation electrode in Li ion batteries. Both graphite and amorphous carbon are used, with several benefits. Carbon is readily available, has a low mass (providing a lightweight battery), is inexpensive, and can hold a sufficient amount of Li^+.[236] However, graphite tends to undergo expansion and exfoliation, which can lead to battery failure.[236] Amorphous carbon, on the other hand, cannot undergo exfoliation, and has a larger lithium capacity than graphite. This is due to the structural differences between the two types of carbon. In graphite, a ratio of one lithium ion per six carbon atoms can be achieved. However, in amorphous carbon, a higher lithium to carbon ratio can be achieved because lithium ions can occupy both sides of the graphene sheets as well as the cavities between the sheets.[138]

There are several properties that are desirable for cathode materials in Li ion batteries. First, the cathode material should have a high free energy of reaction with Li, where at least one Li^+ ion reacts per transition metal and gives a high cell voltage (3.0–3.5 V). To achieve a cell voltage this high, the cathode is usually an oxide. The reaction of the cathode with Li^+ must also be rapid, and completely reversible. Other desirables are low cost and low toxicity.[237] Carbon intercalation anodes are often used in conjunction with a cathode capable of intercalating Li^+. These cells are often called “swing cells” or “rocking chair cells” because the Li^+ ions rock or swing back and forth between the two electrodes as the cell is charged and discharged, as shown in Figure 1.3.[236]

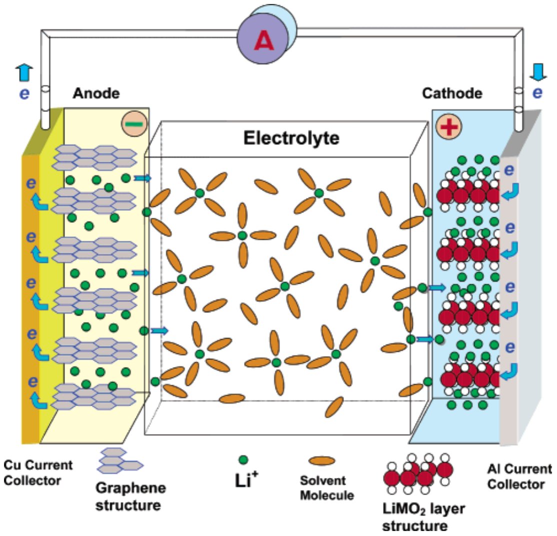

Figure 1.3. Schematic of "rocking chair" cell that contains two intercalation electrodes in which discharge is occurring. If the current was reversed, the lithium would intercalate back into the carbon anode, recharging the cell. Figure reproduced with permission from Xu, *et al.*[238] Copyright American Chemical Society 2004.

Even with many advances in battery technology, most batteries remain essentially two-dimensional, having layered anodes, cathodes, and separators. However, for some applications, a two-dimensional battery cannot provide enough energy per areal footprint size. In order to provide more energy, the third dimension of the battery must be utilized while keeping the separation between the anode and cathode small.[81]

1.4.3.2. Three-Dimensional Batteries

Several designs for three-dimensional batteries have been proposed.[81] Several three-dimensional architectures have been tested for battery applications.[239-242] One of the systems that has been tested uses a 3DOM carbon electrode. 3DOM electrodes have some features that are promising for use in electrochemical cells including a large amount of accessible surface area, a continuous network for improved conductivity, nanometer scale features, and shorter Li^+ diffusion pathlengths.[243] An additional advantage is a 1D path between the electrodes that decreases the polarization associated with mass transport.[82] The goal when designing three-dimensional batteries is to find a compromise between maximizing the power and energy density of the cell while decreasing the ion transport distance. The ion transport distance is minimized by decreasing the thickness of the electrodes and the distance between them, which lessens the amount of power loss in a cell due to slow ion transport.[81]

3DOM carbon has previously been used as the anode in an interpenetrating electrochemical cell.[239,244] A 3DOM carbon anode was coated with a thin polymer separator, electrochemically lithiated, and infiltrated with a V_2O_5 cathode. Poly(phenylene oxide) (PPO) is used as the separator between the anode and the cathode. PPO is electrochemically deposited onto the carbon anode in a self-limiting reaction, allowing for a thin (approximately 10 nm), conformal layer of polymer to form on the anode.[239,245,246] In addition, PPO is electrically insulating, preventing short circuits within the cell, but it is an ionic conductor, which allows Li^+ ions to move between the electrodes.[239,247] This system is capable of shuttling Li^+ between the electrodes and shows a modest gravimetric discharge capacity (capacity available per unit mass during discharge).[239,244]

When vanadia was used as the cathode in the interpenetrating cell, the electrical conductivity of the cathode was lower than desired.[244] The goal of this work was to improve the performance of the system by improving the conductivity of the cathode by adding another conductive phase. In order to improve the conductivity of the system, doping of the cathode with a more conductive material, RuO_2 (ruthenia), was attempted. RuO_2 has previously been used to make a variety of composites, including a V_2O_5/RuO_2 composite.[248] RuO_2 was selected because of its high conductivity (it has been demonstrated to increase the conductivity of composites by two orders of magnitude),[249-252] low synthesis temperature (in order to avoid decomposition of the polymer separator layer),[252] and the wire-like structure of RuO_2 that can form, allowing a high distribution of RuO_2 in the cell while using only a small amount of material.[252,253] RuO_2 can form wire structures within porous materials due to the autocatalytic decomposition of the precursor RuO_4 onto a RuO_2 surface, as opposed to the electrode material.[96,252] RuO_2 has been used to connect commercial intercalation materials, producing a conductive bicontinuous network, while only accounting for 1% of the electrode mass.[253] Ruthenia can exhibit pseudocapacitance, especially in the hydrous form ($RuO_2 \cdot xH_2O$).[249,251,254] In addition, it has been shown that Li ions can be stored in RuO_2, making it an ideal addition to a cathode for a Li ion battery.[255]

In the most common low-temperature ruthenia synthesis method, a ruthenium precursor (typically RuO_2 or $RuCl_3$) is dissolved in a saturated, aqueous solution of sodium periodate, forming RuO_4, which is then extracted at low temperature into an organic solvent. As the temperature is increased, RuO_4 slowly decomposes back into RuO_2, allowing for deposition of ruthenia within a porous electrode.[252,253,256] The physical properties of the ruthenia strongly depend on the post-synthesis treatment. In order for the ruthenia to be conductive, the crystalline phase must be obtained by heating. The properties depend on the atmosphere, temperature, and duration of heating.[249,250,252,253]

1.4.4. Sensors

1.4.4.1. Ion-Selective Electrodes

Ion-selective electrodes (ISEs) are widely used tools throughout many fields of science and technology. It is estimated that over a billion ISE measurements are performed yearly just in clinical applications.[257] Considering the many other fields in which ISEs are used, including process control monitoring, pollution control, water quality monitoring, food quality control, industrial pollution, research and education, as well as many others, it can be assumed that several billion measurements are carried out each year using ISEs.[258-260] ISEs are widely used because of their many advantages, including direct measurements with little sample preparation, the long lifetime of sensors, and the quickness and low cost of measurements.[261]

A general ISE system is shown in Figure 1.4. An ion-selective electrode and a reference electrode are placed in the sample solution. Ion-selective electrodes operate based on the difference between two phase boundary potentials (the solution/sensing membrane potential, and the sensing membrane/inner electrolyte potential). Since the ionic concentrations of the inner electrolyte and the membrane are known, the concentration of ions in the sample solution can be determined.[259,262,263] However, the use of an inner filling solution presents several problems, including electrode failure if the solution evaporates, the necessity of routine maintenance by trained personnel, and the inability to miniaturize the electrode.[264] In addition, the composition of the inner filling solution must be optimized to lower the detection limit of the electrode. This is typically done empirically, which can be very time consuming.[259] There is an ongoing effort to eliminate the inner filling solution from sensor systems.[265-269]

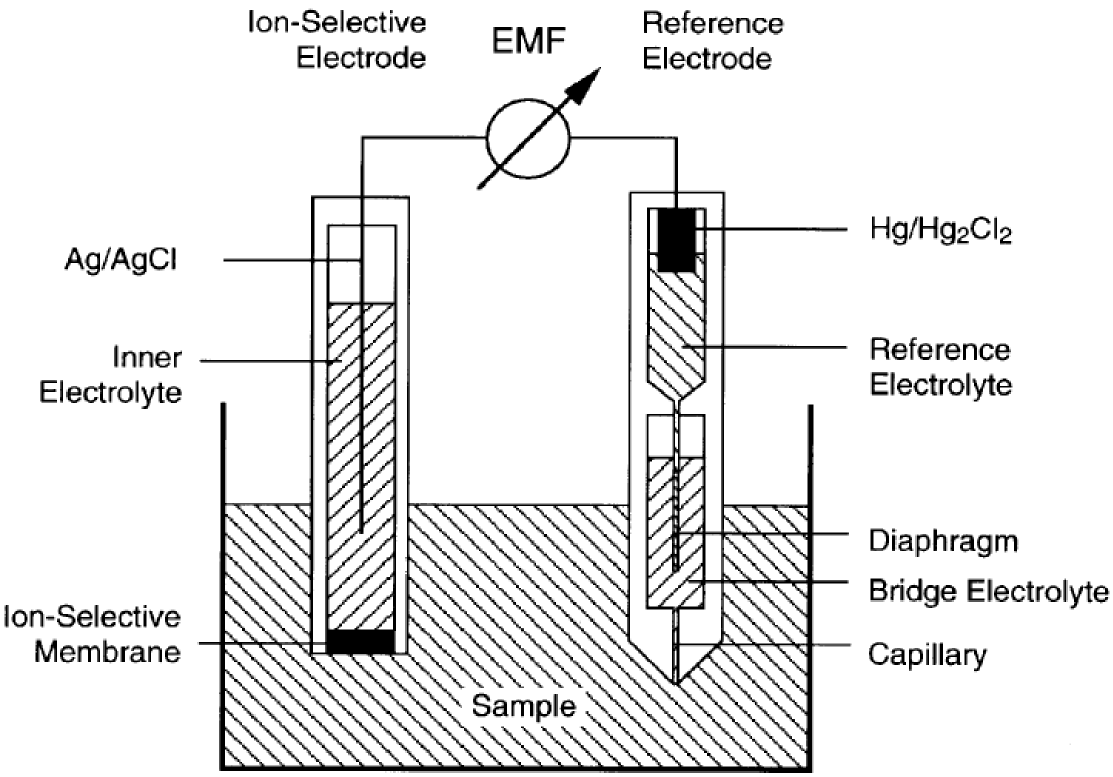

Figure 1.4. Schematic of ion-selective electrode system. Reproduced with permission from Bakker, *et al.*[259] Copyright Wiley-VCH 1999.

In order to create smaller, more robust ISEs capable of achieving lower detection limits, methods to create sensors without the use of an inner filling solution have been investigated. Electrodes without an inner filling solution have other advantages, including being able to withstand more extreme temperatures, they can be used in any orientation in space, and are often more stable electrodes with inner filling solutions, reducing the need for calibration.[264] These electrodes use a solid contact (SC) instead of an inner filling solution. The first SC-ISEs, known as coated-wire electrodes, were simply metal current collectors coated with sensing membranes.[268] While coated-wire electrodes often show higher selectivity than electrodes with inner filling solutions, they do not show long-term stability because the interface between the membrane and the metal is ‘blocked’, meaning that the phase boundary potential between the wire and the membrane is poorly defined. This prevents charge transfer between the metal and the membrane. This leads to a drifting potential, which prohibits accurate measurements and long-term measurements.[258,264,270]

In order to create a more stable electrode, insertion of an intermediate layer (a solid contact) between the sensing membrane and the metal contact has been widely investigated. An intermediate layer must be capable of conducting ions and electrons, allowing charge transfer between the metal and the membrane, creating a more stable electrode. The common intermediate layers that have been investigated are self-assembled monolayers[267] and conducting polymers such as poly(pyrrole),[266,271-277] poly(3-octylthiophene),[277-280] poly(aniline),[278,281] and poly(3,4-ethylenedioxythiophene).[282] Both of these types of solid contacts have drawbacks. The self-assembled monolayers have a low redox-capacitance, which leads to polarizability of the electrode.[283] The response from conducting polymers in ion-selective electrodes can be influenced by several factors, including pH changes (or interference from CO_2),[282,284-290] exposure to O_2,[291,292] or light (if the conducting polymer is a semiconductor with a bandgap in the visible region).[293]

In this work, 3DOM carbon is investigated as a solid contact for ISEs to eliminate these problems. 3DOM carbon is an ideal solid contact because it is redox active, allowing a well-defined phase boundary potential to be established, while avoiding the downfalls exhibited by conducting polymers and self-assembled monolayers as solid contacts.

Besides the solid contact, the composition of the sensing membrane has a large effect on the behavior of the ISE. Sensing membranes are typically composed of four components. A polymer provides the mechanical stability of the sensing membrane. Poly(vinyl chloride) (PVC) is a very common choice due to its low cost, and good mechanical properties.[257] However, since the glass transition temperature of PVC is above room temperature, it is not flexible enough to allow diffusion of ions within the membrane. In order to alleviate this issue, PVC can be plasticized. An organic solvent (plasticizer) is added to the polymer which changes its mechanical properties and makes it suitable for use as a sensor membrane.[264] The identity of the plasticizer can also affect the sensing effectiveness of the membrane.[258] The most important component of the membrane is the ionophore. An ionophore is a lipophilic ion or molecule which selectively binds to an analyte (typically an ion or specific class of ions) and lowers the free energy of ion transfer of the analyte into the membrane. The identity of the ionophore dictates what ion(s) the sensing membrane will respond to. Hundreds of ionophores have been reported in the literature, and a wide variety of analytes can be measured.[258,294-296] There are several requirements which an ionophore must meet to be effective. First, the binding of the ionophore and the analyte must be fast, leading to a shorter time to reach equilibrium and quicker response times. However, the binding between the ionophore and the analyte cannot be too strong. If the binding is irreversible, the response of the sensor will be affected. In addition, the ionophore must be lipophilic so it stays in the polymer membrane and does not leach into the aqueous phase, which limits the lifetime of the sensor.[258,259] The last component in a typical sensing membrane is ionic sites, which are ions of the opposite charge as the analyte. The ionic sites allow the analyte to enter the sensing membrane without requiring a counter-ion to enter the membrane as well.[258] Without the presence of ionic sites, the membranes are not effective ion exchangers, and do not function as sensors.[259]

1.4.4.2. Receptor-based Sensors

In addition to ion detection, sensors have been developed for small molecule detection. Instead of a sensor with an ionophore-containing sensing membrane, receptor-based detection systems have been developed. In a general sensor, after the analyte of interest has selectively interacted with the receptor, an output is produced indicating that the interaction occurred.[297-299] However, the analytes, receptors, types of interactions, and signaling mechanisms vary widely.

There are three broad categories of analytes for which receptors can be developed: cations, anions, and neutral small molecules (including organic, inorganic, and biological molecules).[299] Cations are typically metal ions, including group I and group II metals, transition metals, and lanthanides.[298,300,301] Biologically relevant cations are also common analytes, including acetylcholine.[302] Common anions include citrate,[303,304] nitrate,[305] and heparin.[306] A wide range of neutral molecules can be detected, including biologically relevant molecules (ATP and glucose), [307,308] alcohols, amines, aldehydes, and sugars.[309]

There are several types of intermolecular interactions that can occur between the receptor and the analyte, depending on the identity of the analyte. For small, neutral molecules, the most common interaction types are hydrogen bonds,[299,301] π-interactions,[301] dipole alignment,[298] van der Waals forces,[299] donor-acceptor interactions,[299] and solvophobic interactions.[298] For cations, coordination interactions are common.[301] For anions, electrostatic interactions are usually present.[299,301]

Most receptors are based on supramolecular chemistry, which focuses on the molecular assemblies based on intermolecular forces instead of covalent bonds.[299] The goal is to select a receptor that has the necessary structural and chemical features to allow it to interact selectively with the analyte of interest.[299,301] The binding sites of receptors can be described by many properties, including size, shape, conformation, chirality, reactivity, and electronic properties.[299]

Two of the most important considerations when choosing or designing a receptor are the selectivity for a particular analyte, as well a high affinity (leading to a high sensitivity).[299,310,311] For example, explosives can be detected with chemical specificity by functionalizing cyclodextrins to change the size and/or shape of the cavity.[312]

Once the receptor-analyte interaction has occurred, the signal (no matter what the mechanism is) should change significantly enough to be easily measured.[301] Examples of signaling mechanisms are changes in the electronic, ionic, optical, or conformational properties of the system.[299] The signaling mechanism can be measured by optical spectroscopy, including absorbance[297] and fluorescence.[301,304,311] In addition, electrochemical methods may be used for detection including voltammetry and potentiometry.[297] Simpler signaling mechanisms, such as color change, may also be used.[298]

1.5. Summary and Outlook

Carbon is one of the most ubiquitous and useful elements. The many allotropes of carbon have different properties that make carbon useful in a wide variety of applications. In addition, by simple changes in synthesis conditions, the properties of synthetic carbons can be optimized rather easily. After synthesis, the chemical and physical properties can be modified in many ways by surface functionalization. These properties, in addition to low cost, electrical conductivity, and high surface area, make carbon materials ideal candidates for electrochemical applications such as capacitors, battery electrodes, and sensors.

In this work, 3DOM carbon is investigated for use in electrochemical applications. In Chapter 2, the use of 3DOM carbon as an anode in an interpenetrating electrochemical cell with a ruthenium-oxide-containing cathode is discussed. Chapter 3 examines the use of 3DOM carbon as a solid contact in ion-selective electrodes, including a discussion of the source of the excellent detection limit and electrode stability that have been achieved. Chapter 4 describes the use of 3DOM carbon in receptor-based sensors designed to detect explosives and explosives analogues, such as 2,4-dinitrotoluene. Chapters 3 and 4 both contain information regarding the electrochemical properties of 3DOM carbon. Chapter 5 provides a summary of the work as a whole.

Chapter Two

Optimization of a Ruthenia Cathode in an Interpenetrating Electrochemical Cell Utilizing Three-Dimensionally Ordered Macroporous Carbon as the Anode Material

2.1. Motivation

Powering small electronic devices with high energy demands (in which the areal footprint available for a battery is small) is still an issue that needs to be addressed. One approach to increase the amount of energy that a battery can supply is to utilize the third dimension of the battery instead of increasing the size of the two-dimensional components that typically comprise batteries.[81] 3DOM carbon has been targeted as a potential electrode material and structural foundation of a three-dimensional interpenetrating lithium ion battery.[239,244] As in any lithium ion battery, an anode and a cathode (both Li^+ intercalation materials) are separated by an electrically insulating, ion conducting separator layer. When 3DOM carbon is used as the anode, the void space of the anode can be filled by a second phase (the cathode) after applying the separator layer. This design allows for a large interfacial surface area between the anode and the cathode, continuous networks for improved conductivity through the electrode materials, and shorter Li^+ diffusion pathlengths than in traditional batteries.[243]

In order to produce a three-dimensional interpenetrating Li^+ ion battery, it is necessary to have a cathode that can be prepared at mild temperatures to prevent the destruction of the polymer separator membrane. Originally, vanadia (V_2O_5) was chosen as the cathode for this system.[239,244] It offers many advantages, including a low-temperature synthesis method, ease of synthesis, low cost, and high energy density.[313] However, the low electrical conductivity of the vanadia cathode led to poor performance of the cells.[239,244] It is possible to improve the conductivity of vanadia by doping it with high conductivity materials.[248,314] Here, ruthenia (RuO_2) was selected as the dopant for several reasons. First, the crystalline form of RuO_2 is highly conductive.[251] A mixture of RuO_2 and V_2O_5 has been shown to increase both the lithium capacity and electronic conductivity of the cathode (when compared to pure V_2O_5).[248] Ruthenia has also been used alone as a cathode because it provides a high lithium capacity and coulombic efficiency.[255] In addition, ruthenia can be synthesized using a low temperature synthesis,[248,250,252] which is compatible with the presence of the polymeric separator layer. It has been shown that RuO_2 prepared by this low-temperature synthesis can self-wire throughout a porous material.[252] This would allow continuous electron flow throughout the pore structure while incorporating only a small amount of ruthenia.

The aim of this work was to construct an interpenetrating lithium ion battery with a 3DOM carbon anode and a ruthenia-doped vanadia cathode. Since it is necessary to deposit the ruthenia into the electrode before the vanadia (the vanadia cannot be heated after deposition, and heat treatment of the ruthenia after synthesis is necessary), and because the synthesis of vanadia within the pores of the 3DOM carbon anode was previously established,[244] this work focuses primarily on the ruthenia deposition. In the ruthenia synthesis, solid RuO_2 is oxidized to form a solution of RuO_4 which then undergoes a cryogenic decomposition to solid RuO_2.[248,250,252] Several approaches were tested to increase the loading of RuO_2 within the macropores of the electrode. The rate of warming of the RuO_4 solution is the critical step in the RuO_2 synthesis. The conversion of RuO_4 to RuO_2 occurs at approximately –35 °C.[252]

Here, several parameters in the construction of an interpenetrating electrochemical cell with a 3DOM carbon anode, a polymer separator layer, and a vanadia and/or ruthenia cathode are optimized. A method for making the separator layer deposition more efficient, as well as methods to increase the amount of ruthenia deposited within the macropore network and a mild route to produce anhydrous ruthenia by post-synthesis treatment are discussed.

2.2. Experimental

2.2.1. Materials

Chemicals used in these experiments were obtained from the following sources: methyl methacrylate (99%), 2,2’-azobis(2-methylpropionamidine) dihydrochloride (97%), resorcinol (99%), acetonitrile (anhydrous, 99.8), and triisopropylvanadium(V) oxide (TIVO), tetramethylammonium hydroxide pentahydrate (97%), ethylene carbonate (anhydrous, 99%), dimethyl carbonate (anhydrous, ≥99%), ruthenium(IV) oxide hydrate ($RuO_2 \cdot xH_2O$, 99.9%), and $RuCl_3$ from Sigma-Aldrich; tetrabutylammonium perchlorate (99.0%), and lithium perchlorate (99.0%) from Fluka; formaldehyde solution (37% aqueous solution) from Fisher Scientific; sodium carbonate (anhydrous, 99.7%) from J.T. Baker; Ni mesh from Dexmet Corporation, acetone and hexanes from Mallinckrodt Chemicals. All deionized water used was purified to a resistivity greater than 18 MΩ. All chemicals were used as received, except lithium perchlorate, which was dried at 140 °C under vacuum prior to use.

2.2.2. Colloidal Crystal Template Synthesis

Monodisperse poly(methyl methacrylate) (PMMA) spheres were synthesized by an emulsifier-free emulsion polymerization as previously described.[54] A 3000 mL five neck round bottom flask was placed inside of a heating mantle, and the middle neck was equipped with an Arrow lab stirrer attached to a glass stirring shaft with a Teflon stir blade. The second neck was fitted with a water cooled condenser attached to a water bubbler, while the third neck contained a thermocouple attached to a temperature controller. In order to provide an oxygen free system, a nitrogen line was attached to a glass pipet that was fitted through a rubber stopper and placed in the fourth neck of the flask. A glass stopper was placed in the fifth neck of the flask and used for addition of chemicals.

Deionized water (1600 mL) and methyl methacrylate monomer (400 mL) were added to the flask and the nitrogen was turned on to a low flow rate (approximately one bubble per second). The temperature controller was set to a temperature of 70 °C and the system was allowed to equilibrate. After the temperature stabilized, 1.50 g of the initiator (2,2’-azobis(2-methylpropionamidine) dihydrochloride) was dissolved in about 25 mL of deionized water and added to the flask and the nitrogen flow was stopped. Within several minutes, the mixture in the flask turned milky white. Over the course of the reaction the temperature rose several degrees before returning to 70 °C, signaling the end of the reaction. After cooling, the solution was filtered through glass wool into a large plastic jar in order to remove large agglomerates of polymer spheres.

In order to form a colloidal crystal template, the polymer spheres were sedimented into an ordered array. The PMMA suspension was poured to a depth of 0.8–1.2 cm in a large crystallization dish and tightly covered. The dish was placed in a location free from vibration and drafts to allow the spheres to sediment. After the spheres settled, opalescence was visible around the bottom edge of the crystallization dish. The cover was then partially removed to allow water evaporation. After all of the water evaporated, the colloidal crystal cracked into small pieces (approximately 1–2 cm on each side, and 2 mm thick) that were used as colloidal crystal templates.

2.2.3. 3DOM Carbon Synthesis

The colloidal crystal templates were used to prepare 3DOM carbon from a resorcinol-formaldehyde precursor solution as discussed in detail in Chapter 3 (section 3.2.2.). Briefly, resorcinol, formaldehyde solution, and a sodium carbonate catalyst were allowed to stir for approximately 20 minutes. The solution was then infiltrated into the PMMA colloidal crystal templates. The PMMA/resorcinol-formaldehyde composites were then heated at 85 °C for three days to allow the resorcinol-formaldehyde precursor to further crosslink. The composites were then heated under flowing nitrogen at 900 °C in order to carbonize the resorcinol-formaldehyde precursor as well as burn out the PMMA template, creating porous 3DOM carbon monoliths.

2.2.4. Electrode Fabrication

The 3DOM carbon monoliths were attached to a Ni mesh current collector to prepare the 3DOM carbon electrodes used for the electrochemical experiments as discussed in Chapter 3 (section 3.2.4.). A resorcinol-formaldehyde precursor solution (prepared as for the 3DOM carbon synthesis described above) was heated and stirred until viscous. This solution was used to attach the Ni mesh current collector to the 3DOM carbon monoliths. The electrodes were heated in a sealed container overnight at 85 °C in order to crosslink the resorcinol-formaldehyde adhesive. The resorcinol-formaldehyde adhesive is not conductive, but a strong contact between the carbon and the current collector allows for sufficient electrical conductivity.

2.2.5. Interpenetrating Cell Synthesis/Assembly

2.2.5.1. PPO Coating

An electrically insulating, ion-conducting layer between the anode and the cathode is necessary when constructing a battery. In this case, poly(phenylene oxide) (PPO) was selected as the separator. A thin, conformal coating of PPO was applied to the finished electrodes by self-limiting electropolymerization. The electropolymerization solution was air sensitive and thus was prepared in an argon filled glove box. In a glass bottle, 0.476 g phenol, 0.906 g tetramethylammonium hydroxide pentahydrate, 1.71 g tetrabutylammonium perchlorate (0.0050 mol of each component), and 50.00 mL acetonitrile were stirred for several hours. The 3DOM carbon electrode, a Pt gauze reference electrode, and a Pt foil counter electrode were inserted into a 100 mL three-neck round bottom flask. In the glove box, enough electropolymerization solution was added to the flask to fully cover the carbon and cover the bottom of the Pt electrodes. The closed flask was removed from the glove box and attached to an Arbin battery testing system. The electropolymerization was carried out by applying a potential of 1.2 V vs. Pt for 30 minutes followed by a rest period of 30 minutes, performed four times total. After washing the electrode with clean acetonitrile and allowing it to dry, the electropolymerization was repeated with new solution. The electropolymerization process was repeated until the peak current was below 0.5 mA (typically about four electropolymerization cycles).

2.2.5.2. Lithiation

Lithium ions were inserted into the carbon structure by electrochemical lithiation before infiltrating the electrode with the cathode material. Before lithiating the carbon, Li^+ was introduced into the PPO coating by soaking the electrodes in 1 M $LiClO_4$ in acetonitrile solution for two days in a dry room (<1 % relative humidity). The $LiClO_4$ solution was removed, and the electrode was allowed to dry in the dry room for 1 day. The electrode was then inserted into a three neck flask with pieces of Li foil as the reference and counter electrodes. A 1 M solution of $LiClO_4$ in propylene carbonate was added to completely cover the carbon and cover the bottom of the Li foil. The system was then allowed to equilibrate for 24 hours, after which it was attached to an Arbin battery testing system for lithiation. Lithiation was carried out by applying a current of –50 μA until the potential dropped below 10 mV vs. Li/Li^+, followed by currents of –20 μA, and

–10 μA, each time until the potential was below 10 mV. This step down procedure was used in order to insert as much Li into the carbon as possible without hindering the Li ion diffusion. After resting, the potential tends to increase slightly. In order to insert more lithium in the carbon, the above electrochemical procedure was repeated after a short rest period if the potential had indeed increased. The solution was not changed between cycles. After the lithiation was completed, the electrode was washed with 1 M $LiClO_4$ in acetonitrile to remove the propylene carbonate. The electrode was then allowed to dry overnight in the dry room.

2.2.5.3. Cathode Infiltration

Before cathode infiltration, it was necessary to place a protective coating on the Ni mesh to prevent contact between the current collector and the cathode which would short circuit the cell. To accomplish this, a flexible rubber coating (PlastiDip®) was applied to the Ni mesh and allowed to dry.

2.2.5.3.1. Vanadia

In order to create an interpenetrating cell, the macropores were filled with a cathode material. To fill with vanadia, V_2O_5, the PPO-coated, PlastiDip®-protected electrode was placed under vacuum in the dry room. After overnight evacuation, 0.3 mL triisopropylvanadium (V) oxide (TIVO) was added by a syringe under static vacuum. The carbon was soaked in the TIVO for 2 hours to allow complete infiltration into the pores. The vacuum was then released and a mixture of 0.9 mL water and 3.0 mL acetone was injected into the flask. The water hydrolyzed the TIVO and the presence of both water and acetone helped control the shrinkage of the gel and prevented collapse of the pores within the gel. After five minutes, vacuum was slowly applied to remove some of the solvent. When most of the solvent had been removed (10–45 minutes, depending on the sample), the vanadia was aged overnight under static vacuum to allow for further condensation.

The following day, the electrode was removed from the cell and placed in a vial containing fresh acetone. The acetone was replaced each hour for a total of eight times to partition the water out of the system. The washing procedure was then repeated with hexanes in order to remove the acetone from the vanadia, as well as to remove the PlastiDip® from the Ni mesh. The interpenetrating cell was then allowed to dry overnight in the dry room.

2.2.5.3.2. Ruthenia

In an attempt to improve the conductivity of the cathode in the interpenetrating cells, ruthenia (RuO_2) was used either as a cathode or a cathode additive. Multiple ruthenia synthesis methods that would allow for infiltration of ruthenia into the porous electrode were attempted.

Cryo RuO_2 Synthesis. A volume of 20 mL of a saturated, aqueous solution of $NaIO_4$ was combined with 20–40 mg $RuO_2 \cdot xH_2O$ in a small glass jar. This mixture was stirred in an ice bath for two hours, forming a milky, yellow solution of RuO_4. The solution was then poured into a plastic centrifuge tube containing 5–10 mL chilled hexane. The RuO_4

was extracted into the hexane phase, and the hexane/RuO_4 solution was transferred to a small flask containing a PPO coated 3DOM carbon electrode with the Ni mesh coated with Plastidip. After optimization of the ruthenia synthesis method, the electrodes used were PPO coated and lithiated. The flask and electrode were chilled in a large dewar containing an acetone bath maintained at –20 to –25 °C using a Neslab immersion chiller or a dry ice/acetone bath which was allowed to slowly warm to room temperature (over the course of several days). At temperatures above approximately –35 °C, RuO_4 decomposed into RuO_2.[252] The progress of the reaction was followed by monitoring the color of the solution; RuO_4 formed a yellow solution while RuO_2 was a black solid. The reaction was allowed to proceed until the yellow color of RuO_4 was no longer observed in the reaction flask, about 4 days. The electrode was then removed from the solution and allowed to dry.

Molecular Sieve Drying. In order to try to exclude water from the ruthenia synthesis, the RuO_4 precursor solution was dried over molecular sieves. After preparation of the RuO_4/hexane solution as above, it was placed in a jar containing freshly dried molecular sieves. This jar was placed in a dry ice/acetone bath (to prevent decomposition of the RuO_4) for 3–24 h. The solution was then transferred to a flask containing the 3DOM carbon electrode in a chilled acetone bath. The reaction then proceeded as described above.

Room Temperature Synthesis. A room temperature synthesis method for RuO_2 adapted from Zheng *et al.* was also utilized.[249] Approximately 20 mg $RuCl_3{\cdot}H_20$ was dissolved in 1 mL liquid (water or water/alcohol mixture) in a small vial by stirring for

>1 h. In order to infiltrate this solution into a 3DOM C electrode, the Ni mesh current collector was bent, allowing the Ni mesh to rest on the bottom of a vial. The $RuCl_3$ solution was then dripped onto the electrode until enough solution had been added to completely cover the carbon. After allowing the electrode to soak for 1 h, several drops of 33–50 wt.% NaOH (in water or water/alcohol) were added to convert the $RuCl_3$ to RuO_2. After 1 h reaction, the solution was removed and the electrode was washed several times with water or a water/alcohol mixture.

2.2.5.3.3. Mixed Vanadia/Ruthenia Cathode

In order to synthesize electrodes containing both RuO_2 and V_2O_5, the RuO_2 was first deposited into the electrode by the cryo synthesis method, as described above. After the RuO_2-containing electrode had been dried in a dry room (relative humidity <1%) overnight, the vanadia cathode was prepared as described above. The electrode was washed thoroughly with acetone to remove all of the water, followed by washing with hexane to remove the acetone. The electrode was dried overnight in a dry room.

2.2.5.3.4. Rehydration Test

To determine if anhydrous ruthenia will rehydrate after being exposed to the vanadia synthesis conditions, a sample of ruthenia (synthesized by the cryo method) was dried at 150 °C for 2 h. Half of the sample was then placed in a vial with a mixture of water and acetone overnight. During this time, the ruthenia powder had settled to the bottom of the vial, allowing most of the water/acetone mixture to be pipetted out. The ruthenia was then allowed to dry at room temperature. Thermogravimetric analysis was performed on the soaked and unsoaked halves of the sample to determine whether rehydration had occurred.

2.2.5.4. Cell Cycling

To cycle the complete cells, an aluminum foil current collector was used for the cathode current collector. The entire assembly was placed between glass slides and held together using a binder clip. The cell was cycled in a glass jar with a rubber stopper. This allowed an inert, dry atmosphere to be created during cycling, which takes place outside of the dry room. Four tungsten rods with copper or stainless steel clips soldered onto the ends passed through the rubber stopper and served as connections to the cell. The Ni mesh and Al foil (current collectors to the anode and cathode, respectively) were connected to two of the clips, while a piece of Li foil was connected to each of the other two clips to serve as a reference to monitor the potential of the individual electrodes. Electrolyte solution, 1 M $LiClO_4$ in propylene carbonate or 1 M $LiClO_4$ in a 1:1 (v/v%) mixture of ethylene carbonate and dimethyl carbonate, was added to cover the cell and the bottom of the Li foil. The cell was assembled in a dry room and purged with argon overnight prior to cycling. The cell was then connected to an Arbin battery testing system for cycling. The current for cycling was 1 μA.

2.2.6. Characterization

2.2.6.1. Scanning Electron Microscopy

The samples were affixed on an aluminum stub with conductive carbon tabs. Imaging was carried out on a JEOL 6700 field emission gun scanning electron microscope with an accelerating voltage of 5.0 kV.

2.2.6.2. Thermogravimetric Analysis

Thermogravimetric analysis (TGA) was carried out on a Netzsch STA 409 analyzer. The samples were heated from room temperature to 900–1000 °C at a ramp rate of 10 °C·min^{-1} in alumina crucibles under flowing air or nitrogen, depending on the sample.

2.3. Results and Discussion

2.3.1. PPO Coating

The 3DOM carbon electrodes were successfully coated with a thin layer of poly(phenylene oxide) (PPO). Figure 2.1 shows the response of the current to the potential steps applied during the electrodeposition process. The electrodes typically required four electrodeposition cycles, each with four deposition steps, to be fully passivated (the peak current below 0.5 mA). The first and fourth electrodeposition cycles are shown. The residual current is attributed to monomer diffusion through the polymer film and oxidation at the surface.[315,316]

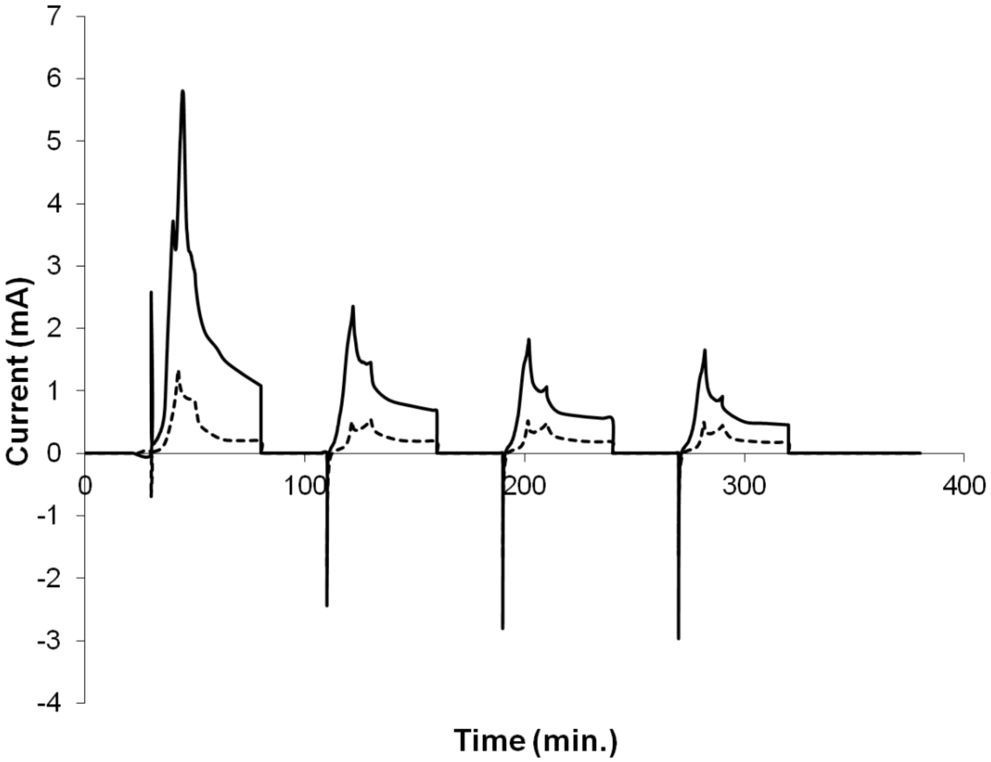

Figure 2.1. Current versus time plot for PPO electrodeposition on a 3DOM carbon electrode. Four electrodeposition cycles were necessary to fully passivate the electrode. The first (solid line) and fourth (dashed line) electrodeposition cycles are shown.

The presence of the PPO layer is also evident when comparing SEM images of carbon from the same batch with and without PPO coating (Figure 2.2). When the polymer coats the surface, the pores and pore windows decrease in size. The size difference in the pores is difficult to determine accurately, but the pore window size is easier to measure. The difference in window sizes before and after polymer deposition gives an estimate of the PPO thickness. In the particular example shown in Figure 2.2, the window size decreased from 62±8 nm before PPO deposition to 51±8 nm after deposition, indicating a film thickness of 5–6 nm. A minimum of 100 pore windows were measured at their longest dimension for each sample using ImageJ Software.

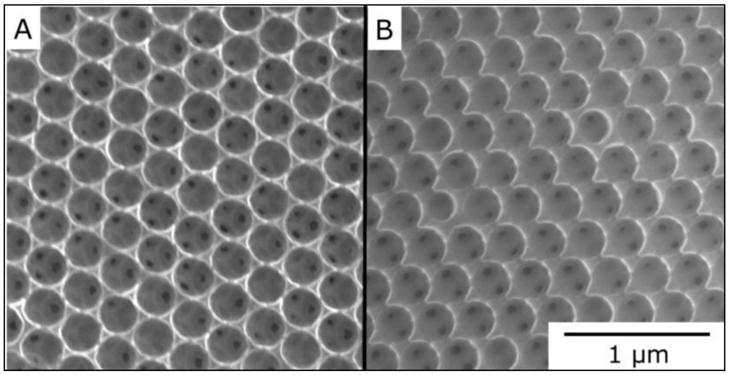

Figure 2.2. SEM image of 3DOM carbon (A) with and (B) without PPO deposition. The difference in window size between the two samples indicates a PPO thickness of 5–6 nm.

2.3.2. Acceleration of PPO Deposition Procedure

For a typical PPO deposition on a 3DOM carbon electrode, four electrodepositions are required, with each electrodeposition requiring one entire day. During this process, PPO was deposited on both the Ni mesh current collector, as well as on the 3DOM carbon anode. In an attempt to decrease the time required for this process, the Ni mesh current collector was insulated prior to the electrodeposition procedure, allowing only the passivation of the 3DOM carbon. The material chosen for insulation must be able to tightly seal to the electrode, preventing contact of the Ni mesh and the electrodeposition solution, and must be stable in a wide variety of chemical environments since it will not be removed before further steps in the battery synthesis are completed. The material must be stable in aqueous and organic solvents that the electrode will encounter in further steps, including water, acetonitrile, hexane, and the battery electrolyte of choice. For this work, unplasticized poly(vinyl chloride) (PVC) was an ideal material.

Electrodes consisting of 3DOM carbon attached to Ni mesh were inserted between two pieces of unplasticized PVC (0.5 mm thickness). The PVC was sealed using tetrahydrofuran (THF) and a commercially available PVC cement. The Ni mesh around the carbon was completely embedded in the Ni mesh, leaving only the carbon exposed. A small amount of Ni mesh at the other end of the electrode was also left exposed to allow for electrical contact to the electrode.

For an electrode that has been encased in PVC, the electrodeposition of PPO only needs to be carried out once before the electrode is fully passivated, with the peak current of the last potential step below 0.5 mA (Figure 2.3).

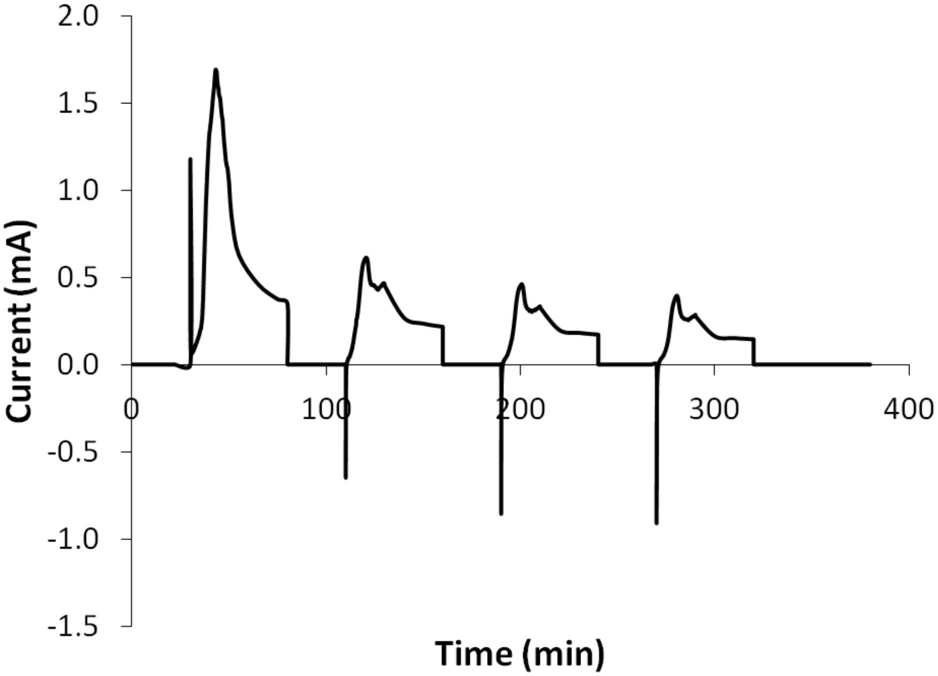

Figure 2.3. Current versus time plot of PPO electrodeposition of PVC encased 3DOM carbon electrode. The electrode is passivated after the first deposition.

If a second electrodeposition is attempted, the observed current is very low, and very little further deposition takes place (Figure 2.4). By insulating the Ni mesh, the time required for the PPO deposition was decreased from approximately four days to one day. In addition, the insulation of the Ni mesh prevents contact between the Ni mesh and the cathode during future battery assembly steps (helping to prevent short circuits in the cell).

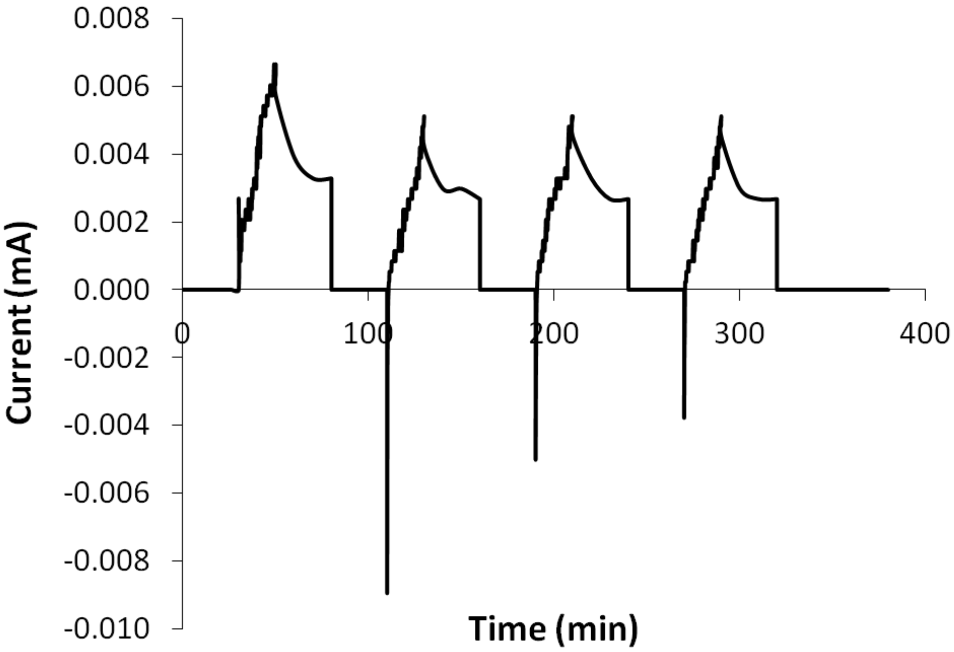

Figure 2.4. The current versus time plot of a second electrodeposition cycle for a PVC encased 3DOM carbon electrode. The current is very low, and very little further electrodeposition of PPO takes place.

2.3.3. Lithiation

PPO-coated 3DOM carbon was lithiated at constant currents of –50, –20, and –10 μA; each step continued until the potential reached 10 mV vs Li/Li$^+$, then stepped down to the next current; the cycle was repeated six total times to get a sufficient amount of lithium into the carbon. This process took about 35 days for a 13.7 mg sample whose data is shown below (Figure 2.5). Part of the reason that the lithiation process was so long is the low ionic conductivity of the PPO coating.[315] The potential vs. Li/Li$^+$ decreased when current was applied, then rebounded slightly during periods of rest. However, the potential increased to 81 mV during the 70-hour rest period at the end of the lithiation, and continued to increase after monitoring was stopped. The potential had increased to 130 mV one week after the conclusion of the lithiation. Ideally, the potential of the carbon would remain stable at the completion of lithiation instead of increasing. The increase in potential was probably due to Li^+ leaching out of the carbon, possibly into the PPO layer.

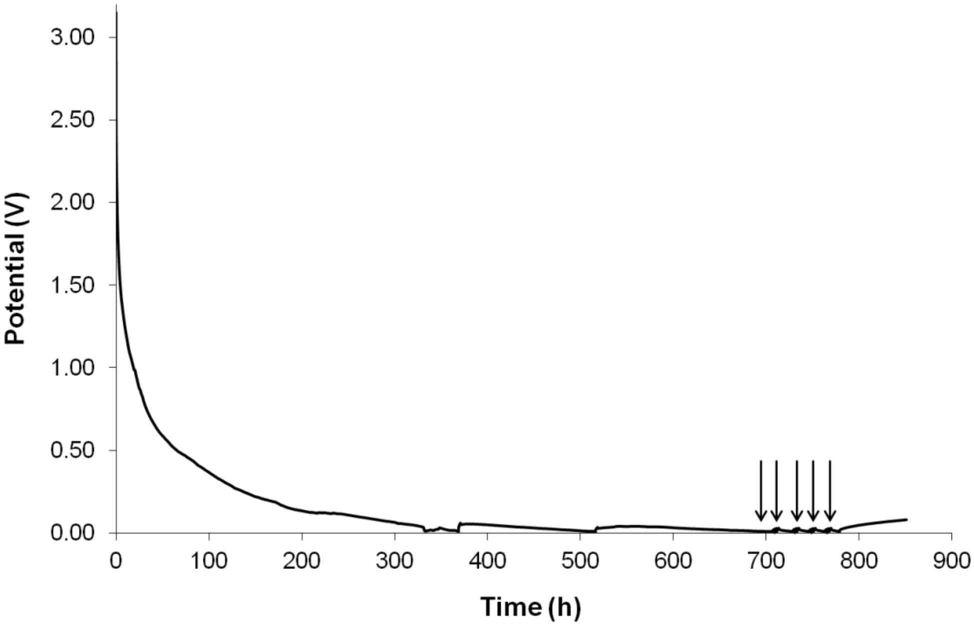

Figure 2.5. Lithiation of 3DOM carbon. Constant currents of –50, –20, and –10 μA were applied to PPO-coated 3DOM carbon until the potential dropped below 10 mV. After a brief rest period, the cycle was repeated in order to increase the amount of Li^+ in the carbon. Potential is measured vs. Li/Li^+. Arrows indicate where cycles 2–6 began. The potential increase at the end was during the final resting step.

2.3.4. Cathode Infiltration

2.3.4.1. Vanadia

Vanadia was successfully infiltrated into a PPO-coated carbon monolith. After washing with acetone and hexanes and drying, the carbon of the electrode appeared green in color, indicating the presence of a layer of vanadia on the surface of the carbon. This surface layer provided a contact area for the Al current collector. As shown in Figure 2.6, vanadia was present in the pores of the carbon monolith as well. The pores appear to be completely filled which allow for Li^+ migration through the cathode.

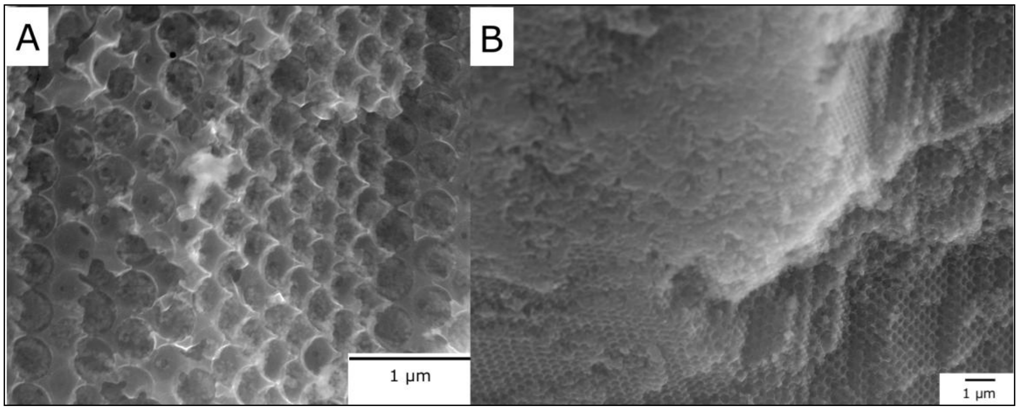

Figure 2.6. SEM images of vanadia infiltrated 3DOM carbon. Image (A) shows pores filled with vanadia, while image (B) shows the surface vanadia layer.

2.3.4.2. Ruthenia

Early experiments used a dry ice/acetone bath in a dewar to chill the flask containing the electrode and the RuO_4 solution. However, the temperature of the bath was difficult to control once it began to warm up. Since the conversion of RuO_4 to RuO_2 begins to occur at –35 °C, as mentioned above, even though the flask may be in the dewar for several days, the actual amount of time during which a reaction was occurring was quite small. The reaction only occurred while the temperature in the dewar increased from –35 °C to room temperature. This temperature increase was difficult to control with a dry ice/acetone bath and tended to occur quite rapidly. This led to most of the RuO_4 decomposing to RuO_2 outside of the 3DOM carbon electrode. A large amount of RuO_2 was found on the surface of the electrode and in the hexane solution in which the electrode was immersed, but only a small amount of RuO_2 was observed inside of the electrode (Figure 2.7).

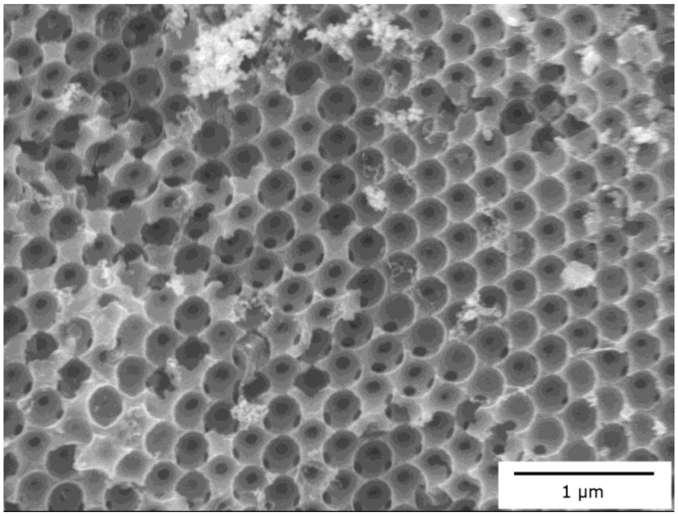

Figure 2.7. SEM image of a cross section of a 3DOM carbon electrode in which RuO_2 was formed by decomposition of RuO_4 during the warming of the solution in a dry ice/acetone bath. Very little RuO_2 was observed in the interior of the monolith.

When a chilled acetone bath was used to control the temperature of the reaction flask, the temperature was maintained between –20 and –25 °C. Even though this was above the temperature at which the decomposition of RuO_4 occurs, the complete decomposition of RuO_4 to RuO_2, monitored by the color of the solution in the flask, took approximately four days. The decomposition of RuO_4 occurred during the entire reaction period instead of just within a short time frame (as was the case when a dry ice/acetone bath was used). This allowed more of the RuO_2 to decompose in the interior of the electrode, instead of just on the surface and in the surrounding solution (Figure 2.8).

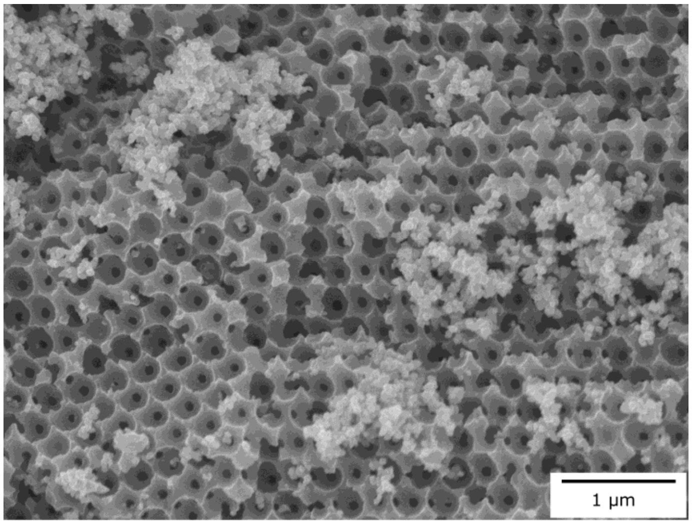

Figure 2.8. SEM image of a cross section of 3DOM carbon electrode in which RuO_2 was formed by decomposition of RuO_4 during the warming of the solution in a chilled acetone bath at –20 to –25 °C. More RuO_2 was observed within the interior of the structure than with the previous method.

Even in areas of the interior of the 3DOM carbon electrode with no obvious RuO_2 growth, energy dispersive X-ray spectroscopy (EDS) showed that RuO_2 was present (Figures 2.9 and 2.10). It is believed that RuO_2 coated the walls in the interior of the electrode in addition to decomposing into wire structures.

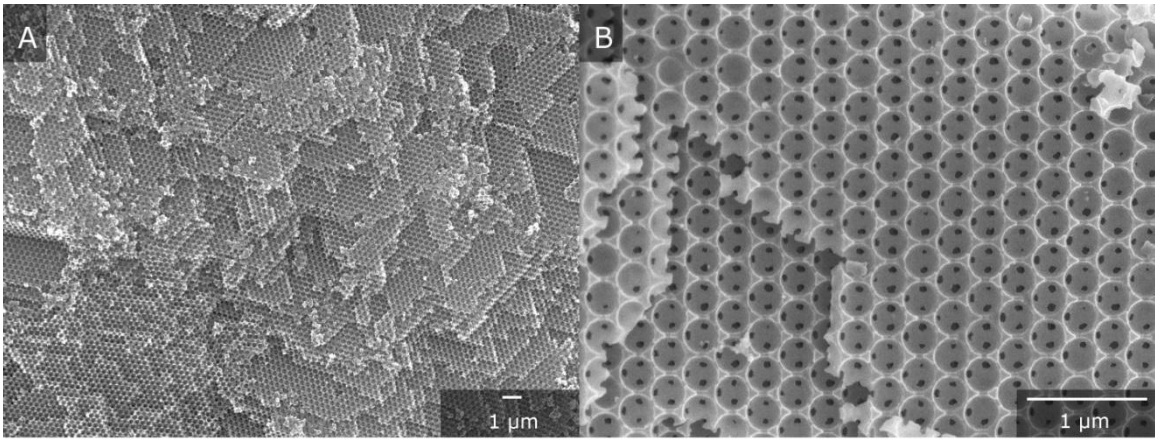

Figure 2.9. Low (A) and high (B) magnification SEM images of the interior of a 3DOM carbon anode in which RuO_2 has been deposited. Very little RuO_2 was visible in the interior of the monolith in this region, but the walls were likely coated with RuO_2. EDS data for the region in (A) is shown in Figure 2.10.

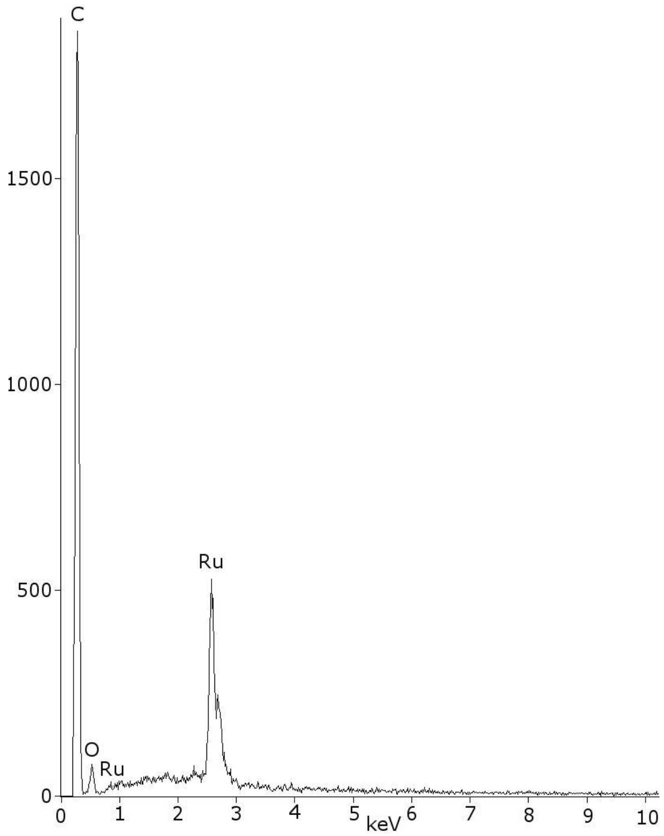

Figure 2.10. Energy dispersive X-ray spectroscopy (EDS) spectrum of the interior of the carbon monolith shown in Figure 2.9A after deposition of RuO_2. The sample contained Ru, O and C.

In addition to having RuO_2 in the interior of the monolith, it is also important to have a layer of RuO_2 on the surface of the monolith. This layer contacts the cathode current collector and prevents direct contact between the current collector and the PPO separator. The surface layer of RuO_2 is shown in Figure 2.11. High and low magnification images of the surface layer are shown.

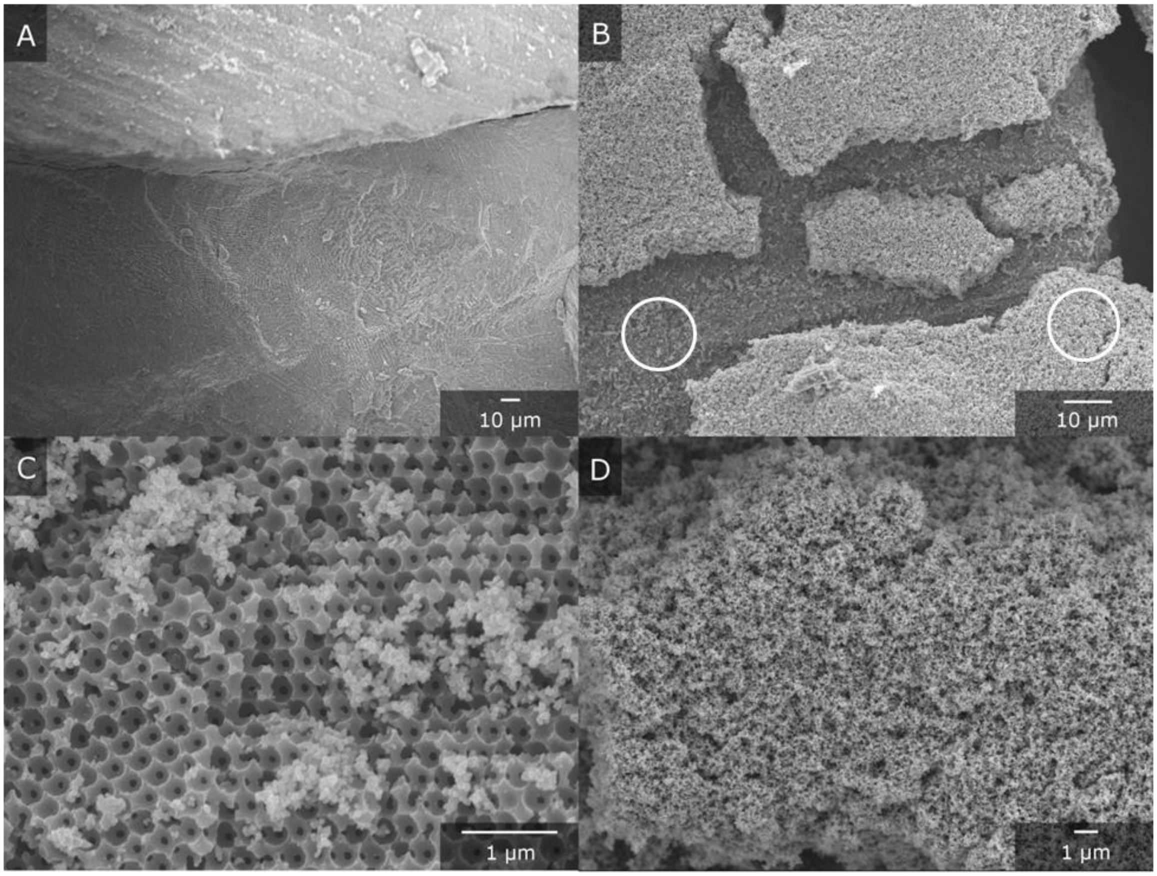

Figure 2.11. SEM images of exterior of monolith after RuO_2 deposition. (A) Low magnification image of a cross section of the monolith showing interior of monolith and surface ruthenia layer. (B) Low magnification image of surface of the monolith. Many large islands of ruthenia are visible. (C) High magnification image of area in left circle in image (B). This region is not in a large ruthenia island, but ruthenia is still visible on the circle. (D) High magnification image of area in right circle in image (B). This region is from one of the large ruthenia islands.

The presence of ruthenia within the interior of the cell was further shown by lithiating the ruthenia. A current of 20 μA was used, and the ruthenia was lithiated until a potential of ~0.5 V versus Li/Li^+ was reached. The potential versus time plot of the lithiation is shown in Figure 2.12.

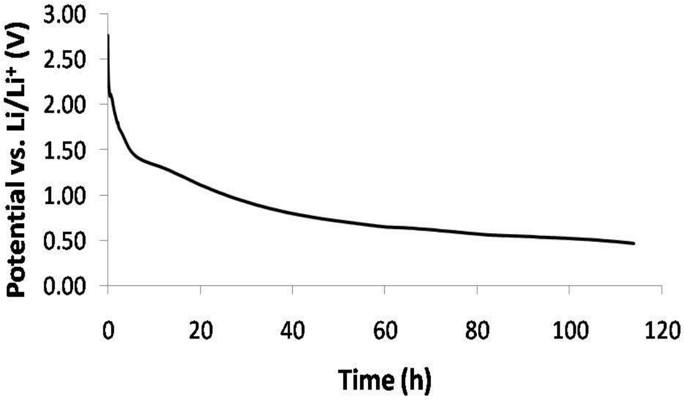

Figure 2.12. Potential versus time plot of lithiation of ruthenia of a cell. A current of –20 μA was applied until the potential was 0.5 V vs. Li/Li^+.

The interior of the cell after lithiation of the ruthenia is shown in Figure 2.13. The ruthenia expanded to fill the pores after lithiation. While a significant portion of the pores are filled, there are areas in the monolith without filled pores. It was hypothesized that there was too little ruthenia inside the monolith to fill the entire structure after lithiation, or the ruthenia was not all connected throughout the structure, preventing lithiation of part of the sample.

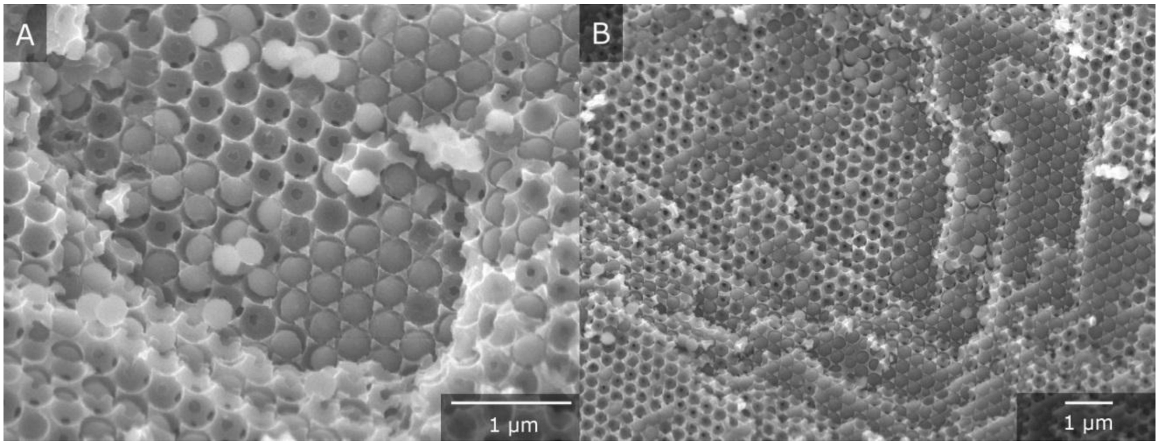

Figure 2.13. SEM images of interior of cell after lithiation of RuO_2. Ruthenia expands to fill the pores.

2.3.5. Cell Cycling

A complete cell containing RuO_2 as the cathode was cycled. The potential versus time plot of the first ~100 cycles is shown in Figure 2.14, and an expanded version is shown in Figure 2.15. The capacity (versus the mass of RuO_2) is shown in Figure 2.16. The capacity of the cell was much lower than expected. The capacity of the cell decreased as it was cycled.

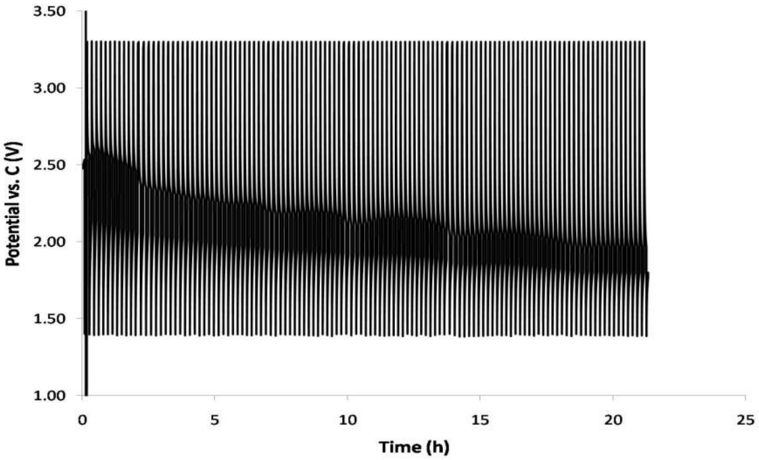

Figure 2.14. Charge/discharge profile of the first ~100 cycles of a RuO_2 cell.

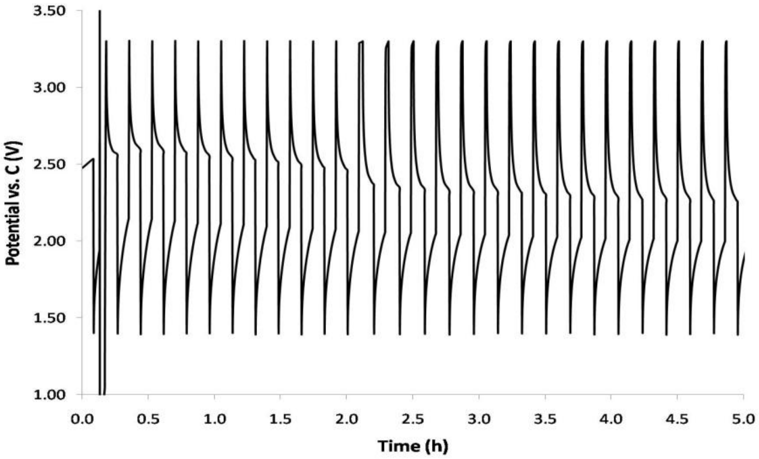

Figure 2.15. Expanded charge/discharge profile for RuO_2 cell.

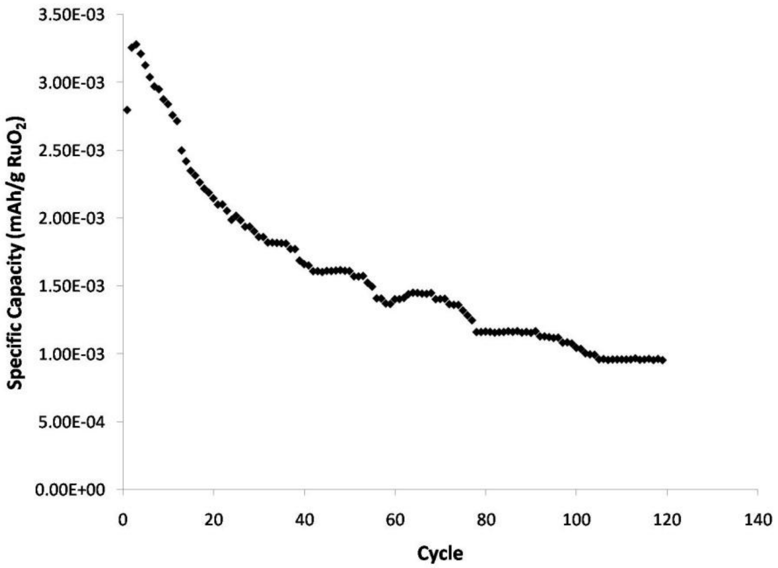

Figure 2.16. Capacity versus cycle number plot of cycling of RuO_2 cell. The specific capacity is based on the mass of ruthenia in the cell.The capacity decreases as the number of cycles increases.

A complete cell containing RuO_2/V_2O_5 as the cathode was also cycled. The potential versus time plot of the first ~100 cycles is shown in Figure 2.17, and an expanded version is shown in Figure 2.18. The capacity (versus the mass of the carbon anode) is shown in Figure 2.19. The capacity of the cell was much lower than expected, but was quite stable over 100 cycles.

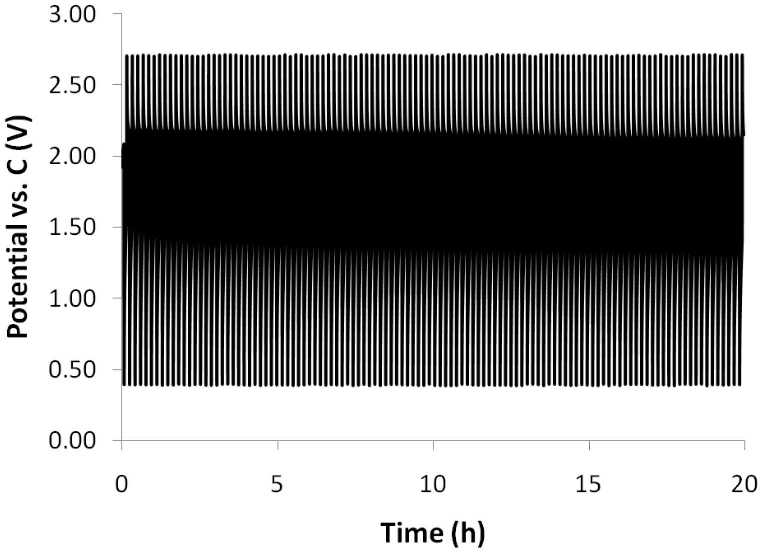

Figure 2.17. Charge/discharge profile of the first ~100 cycles of a RuO_2/V_2O_5 cell.

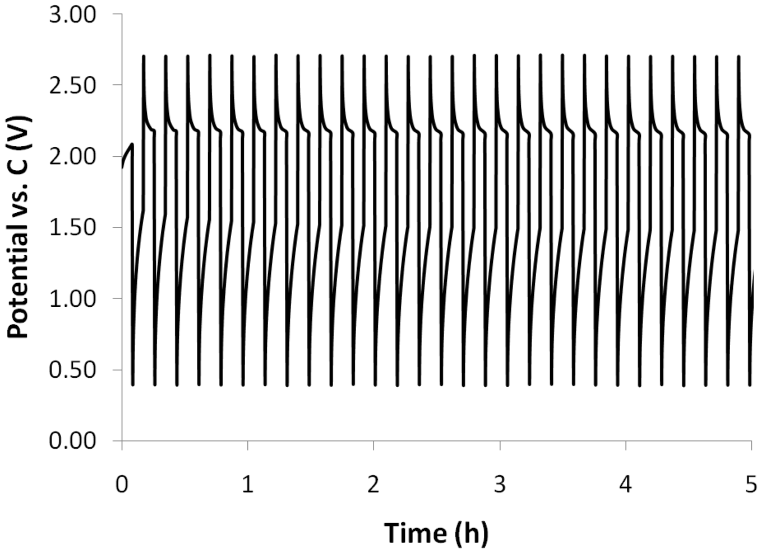

Figure 2.18. Expanded charge/discharge profile for RuO_2/V_2O_5 cell.

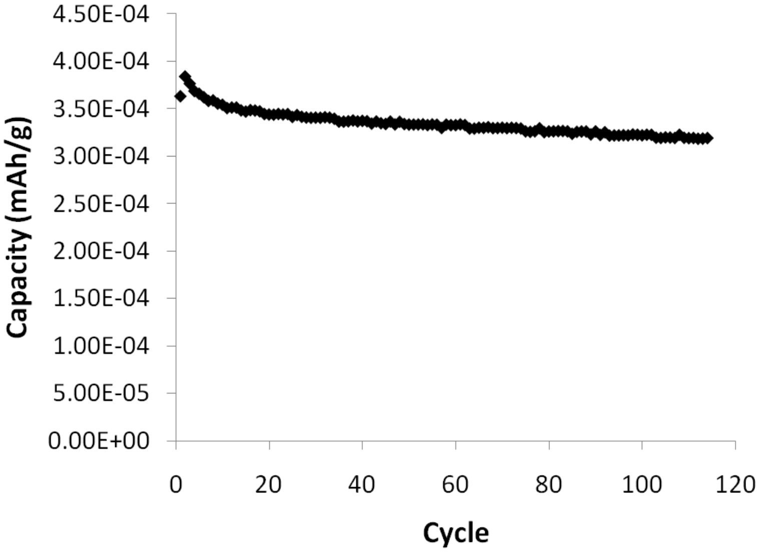

Figure 2.19. Capacity versus cycle number plot of cycling of RuO_2/V_2O_5 cell. The capacity values are based on the mass of the carbon anode. While the capacity values were very low, a relatively constant capacity was obtained.

It was hypothesized that the poor cycling performance of the cells containing ruthenia as the cathode was due to the formation of hydrous ruthenia ($RuO_2{\cdot}xH_2O$) during the cryo synthesis method, not enough ruthenia being deposited inside the electrode to act as the cathode, or due to the low conductivity of the ruthenia as-deposited. Efforts were made to optimize the synthesis and post-synthesis treatment of the ruthenia cathode. The conditions chosen had to be mild enough to not disrupt any of the previous cell synthesis steps, including the PPO deposition and the lithiation.

2.3.6. Optimization of Ruthenia Cathode

2.3.6.1. Amount of Ruthenia Deposited

Two different synthesis methods were compared to determine which would lead to greater ruthenia deposition within a 3DOM carbon electrode. The cryo deposition method (with the cooling bath maintained at –20 to –25 °C) was compared to the room-temperature deposition method. The concentration of the RuO_4 precursor in the cryo method was also increased. In order to determine the best method of ruthenia deposition, TGA was used to determine the amount of ruthenia deposited into 3DOM carbon electrodes by various methods. The results are shown in Table 2.1. Increasing the concentration of the RuO_4 in the hexane solution and reducing the amount of hexane had a dramatic effect on the amount of ruthenia deposited into the electrode. The smaller amount of solution allowed more ruthenia to be deposited into the electrode instead of in the surrounding solution. When using the room temperature synthesis of RuO_2 with $RuCl_3$ as a precursor, solutions containing an alcohol tended to give a higher amount of deposited ruthenia. The alcohol in the aqueous solution allowed for better wetting of the electrode. In addition, using NaOH instead of KOH gave a higher ruthenia deposition.

The best option for a higher ruthenia deposition appears to be using the cryo-deposition method with a higher RuO_4 concentration and a smaller amount of hexane. This system provides the most efficient ruthenia deposition of those tested.

Table 2.1. Fraction of RuO_2 remaining after TGA of 3DOM carbon electrodes. RuO_2 deposited by cryo and room temperature syntheses under a variety of synthesis conditions.

Synthesis	Synthesis conditions	RuO_2 in Sample (%)
Cryo	40 mg $RuO_2 \cdot xH_2O$, 15 mL hexane	10
Cryo	20 mg $RuO_2 \cdot xH_2O$, 5 mL hexane	29
Room temp. ($RuCl_3$)	Aqueous solutions, NaOH	8.6
Room temp. ($RuCl_3$)	Water/ethanol solutions, NaOH	17
Room temp. ($RuCl_3$)	Water/methanol solutions, KOH	6.8
Room temp. ($RuCl_3$)	Water/methanol solutions, NaOH	18

2.3.6.2. Post-Synthesis Treatment

After exposing bulk ruthenia samples to a variety of post-synthesis treatment conditions, thermogravimetric analysis (TGA) was performed to determine if the samples were hydrated. The mass remaining after TGA corresponds to anhydrous ruthenia. The fraction of anhydrous ruthenia in the original sample can be used to determine the molecular formula of the treated sample. The results of the TGA of the ruthenia samples are shown in Table 2.2. Heating cryo-synthesized ruthenia at temperatures up to 100 °C or placing it under vacuum produced samples with a significant amount of water remaining. Heating at 150 or 200 °C eliminated nearly all of the water. Storing the RuO_4/hexane solution over molecular sieves prior to the reaction had only a minor effect.

The room temperature synthesis of RuO_2 from $RuCl_3$ produced a product with slightly less water, but it was still not anhydrous.

Table 2.2. Mass remaining after thermogravimetric analysis and corresponding molecular formula for RuO_2 prepared by cryo and room temperature syntheses with a variety of post-synthesis conditions.

RuO_2 Synthesis	**Post-synthesis conditions**	**Mass remaining after TGA (%)**	**Molecular formula**
Cryo	None	72.9	$RuO_2 \cdot 2.7H_2O$
Cryo	Vacuum, room temp., 24h	74.4	$RuO_2 \cdot 2.5H_2O$
Cryo	Flowing air, 100 °C, 3h	88.8	$RuO_2 \cdot 0.93H_2O$
Cryo	Flowing air, 150 °C, 3h	95.3	$RuO_2 \cdot 0.36H_2O$
Cryo	Static air, 150 °C, 4h	95.1	$RuO_2 \cdot 0.38H_2O$
Cryo	Flowing air, 200 °C, 3h	100.	RuO_2
Cryo (3 h over molecular sieves)	None	75.1	$RuO_2 \cdot 2.5H_2O$
Cryo (24 h over molecular sieves)	None	79.0	$RuO_2 \cdot 2.0H_2O$
Room temp. ($RuCl_3$)	None	84.0	$RuO_2 \cdot 1.4H_2O$

The best option appeared to be heating electrodes containing cryo-deposited RuO_2 at 150 °C in air. This produced a material that was nearly or completely anhydrous, while being mild enough to allow the PPO separator to survive.

To determine if performing the ruthenia deposition and heat treatment before the vanadia synthesis is feasible, half of a ruthenia sample that had been heated to 150 °C in air for 2 h was soaked in a water/acetone mixture overnight. After allowing the sample to dry, both samples were analyzed by TGA. Both samples showed a 100% mass retention, indicating that both are anhydrous ruthenia. The ruthenia does not rehydrate when exposed to the vanadia synthesis conditions.

Cells containing a mixed ruthenia/vanadia cathode following the above conditions were attempted. The depositions were performed on electrodes that had previously been lithiated. While it is possible to achieve a small potential difference (indicating that a short circuit is not present), the carbon had discharged during the cathode infiltration steps. This is due to the exposure of the lithiated cathode to various solvents as well as heat treatment.

The conductivity of the ruthenia also continued to be a problem which prevented cells which survived the synthesis process from cycling well. The ruthenia was hydrous as synthesized, with a very low conductivity. In order to improve the conductivity, the samples would have to be heated above the crystallization temperature (approximately 300 °C, depending on conditions)[249] which is higher than the PPO separator can withstand.

2.4. Conclusion

In this work, optimization of an interpenetrating electrochemical cell with 3DOM carbon as the anode was attempted. A separator material, PPO, was successfully deposited onto 3DOM carbon electrodes. A method for reducing the time required for fully coating an electrode with PPO to one day (from four days), was developed. The PPO-coated electrodes were then lithiated in order to introduce Li^+ ions into the carbon anode.

Several types of cathode materials, including vanadia, ruthenia, and a mixed vanadia/ruthenia cathode were synthesized and infiltrated into the pores of the PPO-coated 3DOM carbon anode. SEM and/or EDS were used to confirm the presence of the cathode materials, especially in the interior of the monoliths. Methods for optimizing the ruthenia synthesis were developed. A mild method for producing anhydrous ruthenia by heating samples of cryo-synthesized ruthenia at 150 °C for 2–3 hours. This produces anhydrous ruthenia under conditions that allow the PPO separator to survive if properly annealed. An efficient set of parameters for increasing ruthenia deposition was developed, which involved using a small volume of a concentrated RuO_4 solution in the cryo synthesis. It was also determined that the vanadia synthesis will not have an effect on the deposited and heat-treated ruthenia. However, the temperatures necessary to produce crystalline RuO_2 (with a high conductivity to increase the overall conductivity of the cathode material) are likely too high for the PPO-coated, lithiated electrodes to withstand. Cells tested after RuO_2 deposition and heat treatment had discharged during the process and could not be recharged.

While a few of the cells constructed were able to be cycled (albeit with very low capacity), many could not be cycled due to a variety of issues, including those mentioned above. The procedure to produce a single cell was long and involved. Even when many cells were produced in parallel, most failed before reaching the stage where they could be cycled. Common problems included carbon detachment from the current collector, breakage of PPO-coated 3DOM carbon monoliths (leading to a short circuit in the cell), and incomplete cathode surface layers (allowing direct contact between the cathode current collector and the polymer separator). The overall process contained too many steps (including the very long lithiation step) to be an efficient process for production of consistently viable electrochemical cells.

Chapter Three

Design and Investigation of Ion-Selective Electrodes with Three-Dimensionally Ordered Macroporous Carbon Solid Contact and Low Detection Limits

Reproduced in part with permission from references 262, 317, and 318. Copyright American Chemical Society 2007, Springer 2009, and American Chemical Society 2010, respectively.

3.1. Motivation

Over the last four decades, ionophore-based ion-selective electrodes (ISEs) have been extensively studied and have become routine tools in chemical analysis.[257,258,294,319-321] They are attractive for applications in clinical diagnostics, process control, and environmental monitoring. With a view to both mass fabrication and measurements in small volumes, the miniaturization of ISEs has attracted considerable interest. Conventional ion-selective microelectrodes[322] are based on an ion-selective membrane separating the sample solution from the inner reference electrode, which is immersed in an inner solution. However, the use of an inner solution impedes further miniaturization since attempts to minimize the volume of the internal electrolyte solution encountered considerable difficulties.[265] In contrast, electrodes without an inner solution are less fragile, do not dry out, and are more robust to external pressure.

While ISEs have been designed for more than 60 analytes and are used for billions of measurements each year, their practical use has been limited to a selected number of application fields, most importantly in clinical chemistry. Their wider use has been impeded by insufficient detection limits. Until a decade ago, most potentiometric sensors could only detect sample concentrations down to the micromolar level, disqualifying them for trace-level measurements. Fortunately, the recently obtained understanding of ion fluxes through ISE membranes allowed the lowering of detection limits drastically.[323,324] The successful minimization of such fluxes was first achieved by an appropriate choice of the internal solution of conventional ISEs, improving detection limits to the nanomolar and even picomolar level.[325-332] However, the optimization of the inner filling solution of a conventional ISE depends on the membrane selectivity, diffusion coefficients and—most importantly—the anticipated sample, which can make the procedure somewhat cumbersome to perform under real-life conditions.[333-335]

As an alternative approach to ISEs without an inner filling solution and to allow for low detection limits, solid-contact ISEs (SC-ISEs) have attracted a lot of attention. The first reported SC-ISEs were commonly referred to as coated-wire electrodes (CWEs).[268] In a CWE, a sensing polymeric membrane is directly coated onto a metallic conductor. Although CWEs are capable of short-term reproducibility of measurements, they show large long-term drifts on the order of several hundred microvolts per hour and higher.[262,336] This limited long term stability has led to CWEs only being used as detectors in certain specific areas, such as capillary electrophoresis[337] and flow injection analysis.[338] The instability of the measured potential can be attributed to the "blocked" interface between the sensing membrane and the metallic conductor, which is characterized by an ill-defined phase boundary potential that often depends on oxygen and other redox-active components of the sample.[270] Many efforts have been made to solve this problem, e.g., by using an inner Ag/AgCl reference electrode and replacing the internal electrolyte solution with a hydrogel-based electrolyte.[339,340] Sensors with a hydrogel layer between the metal contact and sensing membrane were shown to exhibit somewhat smaller drifts than a CWE system (e.g., 250 $\mu V \cdot h^{-1}$ for pH, 90 $\mu V \cdot h^{-1}$ for K^+).[339] However, hydrogel-based ISEs have limitations related to water uptake/release and the corresponding volume changes of the hydrogel layer.[265]

A completely different method to modify the "blocked" interface is to use an intermediate layer with suitable redox and ion-exchange properties that permits charge transfer between the electronic conductor and the sensing membrane. A redox-active self-assembled monolayer (SAM) between the membrane and the inner Au electrode was reported to lead to a stable system because of a well-defined pathway for charge transfer.[267] However, one limitation of monolayers is their inherently low redox capacitance. In order to minimize the polarizability of the solid contact, a sufficiently high redox capacitance of the intermediate layer is required.[283] Conducting polymers that possess this higher redox capacitance have been investigated, such as polypyrrole (PPy),[266,272,273,275,276] poly(aniline) (PANI),[278,281] poly(thiophene) (PT),[279,280] and several of their derivatives. Some of the electrodes using these polymers as an intermediate layer have been reported to be sensitive to CO_2 and pH, such as in the case of PPy, PANI, and poly(3-octylthiophene) (POT).[277,284-289,341] For PANI, partial conversion from its conducting to its nonconducting emeraldine salt form was found during long-term measurements (1–3 months),[281] which results in a decrease of the electrode potential. Moreover, some polymers, such as PT, are organic semiconductors with a suitable band gap for photon absorption, giving SC-ISEs that are photoresponsive.[293] Some of the lowest reported potential drifts that have been achieved based on SC-ISEs are 85 $\mu V \cdot h^{-1}$ for SAM-contacted electrodes,[342] 100 $\mu V \cdot h^{-1}$ for hydrogel-based electrodes, and 30 $\mu V \cdot h^{-1}$ for PPy-contacted electrodes.[273] In view of long-term monitoring under circumstances where frequent recalibration must be avoided, a further reduction of signal drift is highly desirable.

First efforts to use SC-ISEs for measurements with low detection limits were reported by Michalska and coworkers.[343] They incorporated the complexing agent ethylenediaminetetraacetate in electropolymerized poly(3-methylthiophene) intermediate layers. More recently, they presented an impressive nanomolar detection limit for calcium ions by using a polypyrrole solid-contact doped with the Ca^{2+} ligand Tiron (4,5-dihydroxy-*m*-benzenedisulfonate).[344] As could be expected, it has been demonstrated that the detection limit of SC-ISEs is much worse when a water layer is present because ion fluxes between the sample and the water layer arise.[345,346] Indeed, SC-ISEs with electropolymerized polypyrrole that do not show any evidence of a water layer reached a nanomolar detection limit for Pb^{2+}.[276] Even better detection limits, as low as 5.0×10^{-10} M, were achieved with sensing membranes based on the plasticizer-free methyl methacrylate-decyl methacrylate copolymer and poly(3-octylthiophene) intermediate layers that were not doped with the potentially leaching hexacyanoferrate.[347] The improvement in detection limit was probably not only due to the absence of hexacyanoferrate but at least partly due to the use of copolymer, in which diffusion is much slower than in poly(vinyl chloride) (PVC) membranes modified with a high concentration of plasticizer.[348] A nanomolar detection limit for Ag^{+} was reported using this approach.[280] Importantly, whatever type of intermediate layer is being used for SC-ISEs, the conditioning procedure prior to measurements has a crucial effect on the observed detection.[280,349]

Carbon materials were also explored as electrode components in ISEs. Already in the 1970s, early versions of the so-called “selectrodes” were prepared by directly coating the surface of a graphite pellet with an ion-exchanger or ionophore-doped hydrophobic liquid.[350] Long-term drifts of such electrodes were not reported, and they were soon replaced by similar constructs in which Hg_2Cl_2 and Hg were admixed to the graphite pellet, giving an $E°$ shift of 22 mV over 1 week (131 $\mu V \cdot h^{-1}$) for a valinomycin-based selectrode.[351] Carbon materials with a much higher surface area, i.e., carbon nanotubes,[352-355] and fullerenes,[356] have only been used as solid contacts recently. The fullerene-consisting electrode constructs were reported to show much less drift in the initial conditioning process, but long-term drifts were not described. To prepare SC-ISEs with carbon nanotubes as solid contact, a suspension of single-walled carbon nanotubes (SWCNTs) was sprayed onto a mechanical support. After a sufficient amount of SWCNTs had been deposited, an ionophore-doped polymeric membrane was applied. When a current of 1 nA was applied, chronopotentiometry showed a drift of 61.2 $mV \cdot h^{-1}$, which was about 16 times lower than for a CWE system.[353]

In this context, we have tested three-dimensionally ordered macroporous (3DOM) carbon as a new material for SC-ISEs. 3DOM carbon is electrically conductive, and the pores can be infiltrated with the ionophore-doped sensing membrane, making it an ideal solid-contact material. In the present work, 3DOM carbon has been used for the first time as the intermediate layer of SC-ISEs to stabilize the potential difference between the ionophore-doped solvent polymeric sensing membrane and a metallic conductor. An excellent potential stability of this new type of SC-ISEs is reported. Another objective was to determine whether 3DOM carbon-contacted ISEs offer the same advantages of low detection limits as the SC-ISEs with conducting polymers as intermediate electron-and ion-conducting layer. With this goal in view, the effect of membrane composition and the conditioning procedure on the detection limits of these electrodes for K^+ and Ag^+ were determined. The reasons for the remarkable performance of this system in terms of detection limit and potential stability were also investigated. We hypothesized that the high capacitance of the solid contact in 3DOM carbon based electrodes and the large interfacial contact area between 3DOM carbon and the sensing membrane led to the performance advantages of these electrodes and that surface functional groups on the 3DOM carbon surface affected the sensor performance. ISEs with solid contacts prepared from related solid-contact materials (3DOM carbon, oxidized 3DOM carbon, and an untemplated carbon from the same precursor as 3DOM carbon) were studied by cyclic voltammetry, chronopotentiometry, electrochemical impedance spectroscopy, cryo-scanning electron microscopy (cryo-SEM), elemental analysis, titrations to determine the surface chemistry of 3DOM carbon, and potentiometry to measure the initial potential, intermediate-term responses in aqueous layer tests, and long-term drifts.

3.2. Experimental

3.2.1. Materials

High molecular weight poly(vinyl chloride) (PVC), 2-nitrophenyl octyl ether (*o*-NPOE) and *o*-xylylenebis(N,N-diisobutyldithiocarbamate)—despite its Ag^+ selectivity sometimes referred to as copper (II) ionophore (I)—were purchased from Fluka (Buchs, Switzerland), valinomycin, potassium hexafluorophosphate (99.5%), methyl methacrylate (MMA) (99%), 2,2′-azobis-(2-methylpropionamidine) dihydrochloride (AMPD, 97%), resorcinol (99+%), sodium ethoxide solution (21 wt % in ethanol), and bromocresol green/methyl red (mixed indicator solution in methanol) were from Sigma-Aldrich (St. Louis, MO), sodium hydroxide and sodium carbonate solutions were from Alfa Aesar (Ward Hill, MA), sodium bicarbonate solution, hydrochloric acid, sodium carbonate (anhydrous, 99.7%), and the potassium, sodium, and iron salts were obtained from Mallinckrodt Baker (Paris, KY), formaldehyde (37% in H_2O) was from Fisher Scientific (Pittsburgh, PA), unplasticized PVC sheet as substrate was from Goodfellow (Oakdale, PA), potassium tetrakis[3,5-bis-(trifluoromethyl)phenyl]borate (KTFPB) and sodium tetrakis[3,5-bis(trifluoromethyl)phenyl]borate (NaTFPB) were from Dojindo (Kumamoto, Japan), highly oriented pyrolytic graphite (HOPG) (SPI-2) was purchased from SPI Supplies (West Chester, PA). Ni mesh was a gift from Dexmet (Branford, CT). Deionized and charcoal-treated water (18.2 MΩ·cm specific resistance) obtained with a Milli-Q PLUS reagent-grade water system (Millipore, Bedford, MA, USA) was used for all sample solutions. All chemicals were used as received.

3.2.2. 3DOM Carbon Synthesis

3DOM carbon monoliths were prepared as reported by colloidal crystal templating with monodisperse PMMA spheres.[56,63,92,239] PMMA spheres with diameters of 420 nm were synthesized by surfactant-free emulsion polymerization of MMA at 70 °C, initiated by AMPD, as previously described.[54] The sphere suspension was poured into a large crystallization dish, covered, and allowed to undergo gravitational settling. The cover was then removed, and the water was allowed to evaporate, forming opalescent PMMA pieces. 3DOM carbon was prepared by a slight modification of published methods.[56,63] The carbon precursor solution was prepared by stirring resorcinol (3.3 g), formaldehyde (4.5 mL solution), and sodium carbonate (60 mg) in a 60:120:1 molar ratio at room temperature for 20 min. Several PMMA pieces with dimensions of approximately 1 cm × 1 cm × 0.2 cm were placed in a small crystallization dish. The resorcinol-formaldehyde (RF) solution was deposited with a pipet around the PMMA pieces to cover the bottom of the dish but not the PMMA pieces. The dish was covered, and the solution infiltrated the PMMA pieces by capillary action. Once the RF solution reached the top of the PMMA pieces, they were placed in a sealed plastic bottle and kept at 85 °C for 3 days. The PMMA/RF composites were then transferred to a porcelain boat and heated under flowing nitrogen with a heating ramp of 5 $°C·min^{-1}$ to 900 °C. The temperature was kept at 900 °C for 2 h and then reduced back to room temperature with a cooling rate of 10 $°C·min^{-1}$. This process removes the PMMA template and carbonizes the precursor, leaving a porous glassy carbon skeleton with 360 nm diameter pores connected by 90 nm diameter windows.

Untemplated glassy carbon samples were prepared by following the same procedure as for the 3DOM carbon but excluding the template. Oxidized 3DOM carbon was prepared by boiling 3DOM carbon monoliths in concentrated nitric acid at 130 °C for 10–60 min, followed by thorough washing with DI water. Unoxidized and oxidized 3DOM carbon samples had dimensions of approximately 5 × 5 × 0.5 mm^3, whereas untemplated samples had dimensions of approximately 5 × 5 × 1 mm^3.

Before use, the 3DOM carbon monoliths were wet polished with 320 grit sandpaper to remove the untemplated crust and to produce the desired thickness (≈0.25 mm). The carbon monoliths (3DOM carbon, oxidized 3DOM carbon, or untemplated carbon) were then attached to a piece of Ni mesh using resorcinol-formaldehyde carbon precursor (with the same molar ratios as above) that had been heated for approximately 20 min to make it more viscous. A small amount of the RF was used to attach the carbon to the Ni mesh, which was then clamped between two microscope slides, placed in a sealed plastic bottle, and kept at 85 °C overnight for RF curing.

The electrical conductivity of monolithic macroporous carbon was measured to be 0.34 $S \cdot cm^{-1}$ at room temperature with the four-probe van der Pauw method.[357] The probes were attached to the sample using Ag paste as an adhesive (Ted Pella, Redding, CA). For further information regarding the factors affecting the conductivity of 3DOM carbon, see Appendix A.

3.2.3. Sensing Membrane Synthesis

Valinomycin-doped K^+-ISE membranes were prepared according to a standard procedure by pouring a tetrahydrofuran (THF) solution of 200 mg of the membrane components into a glass dish (31 mm i.d.) and letting the THF evaporate slowly at room temperature over 24 h. The membranes were composed of 33–75 wt % polymer (PVC), 0.6 wt % ionic sites (KTFPB or NaTFPB), 1.0 wt % ionophore (valinomycin), and the remainder plasticizer (*o*-NPOE) for all K^+ experiments. Membranes doped with the ionophore *o*-xylylenebis(N,N-diisobutyldithiocarbamate) were prepared in the same way, but the amount of PVC and the ratio of ionophore and ionic sites were varied. The thickness of the resulting membranes was approximately 100 μm.

3.2.4. Electrode Fabrication

The 3DOM carbon/nickel mesh construct was embedded between two PVC sheets, which served as the substrate for the whole setup. A solution of PVC was used to tightly glue the two PVC sheets together and to cover all still exposed Ni mesh and 3DOM carbon, ensuring that there was no direct contact between the ionophore-doped PVC membrane and the Ni mesh, and between the 3DOM carbon and the sample solution. Finally, the 3DOM carbon was covered with a PVC membrane. The 3DOM carbon was covered with the ionophore-doped, plasticized PVC membrane (Figures 3.1 and 3.2). A fairly concentrated THF solution of the same PVC used in the preparation of the membranes could be used for this purpose, but for convenience commercially available PVC cement (a solution of PVC in a mixture of THF, methyl ethyl ketone and cyclohexanone; ACE Hardware Corp., Oak Brook, IL, USA) was used in this study. All electrodes were conditioned in a 100 mM KCl solution for 24 h prior to measurements, unless otherwise noted.

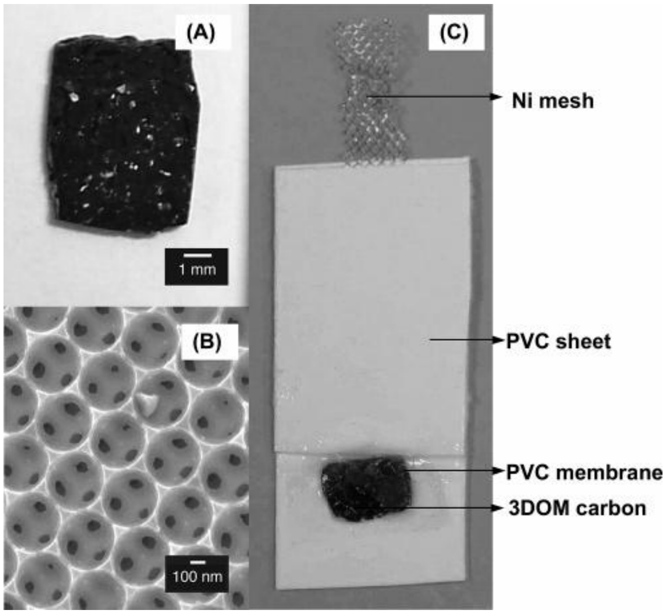

Figure 3.1. (A) Photograph of monolithic 3DOM carbon. (B) SEM image of 3DOM carbon. (C) Photograph of 3DOM carbon-contacted ISE.

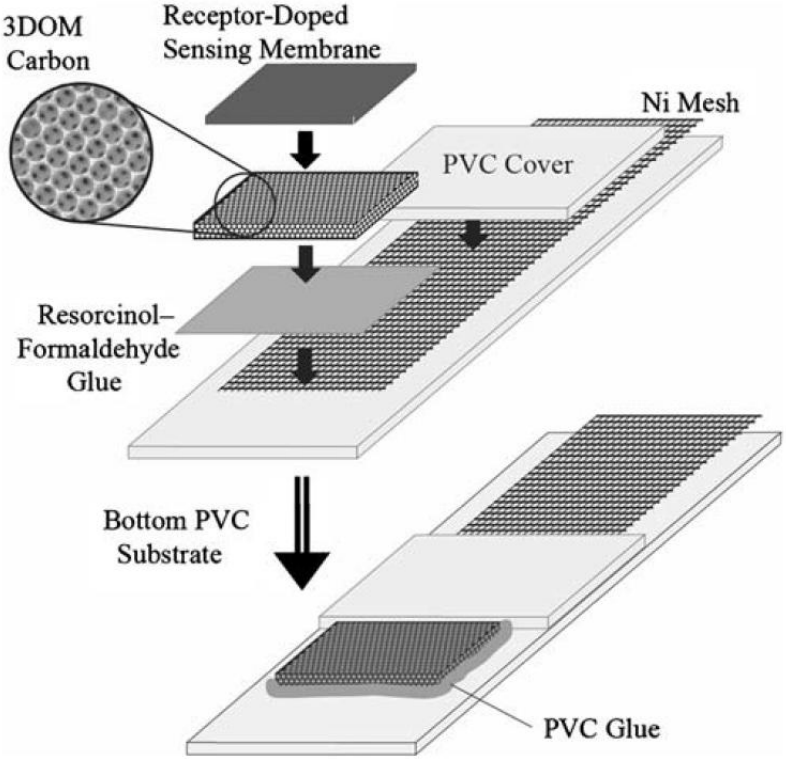

Figure 3.2. Schematic setup of a 3DOM carbon-contacted ion-selective electrode.

3.2.5. Characterization

3.2.5.1. EMF Measurements

Electrode potentials were measured with 2.5 μV resolution with an EMF 16 potentiometer (Lawson Labs, Malvern, PA) controlled with EMF Suite 1.02 software (Fluorous Innovations, Arden Hills, MN) at room temperature (25 °C) in stirred solutions. The external reference electrode consisted of a double-junction Ag/AgCl electrode with a 1 M LiOAc bridge electrolyte and 3 M KCl as reference electrolyte. All measurements of long-term stability were performed with temperature-controlled samples, using a water bath. All EMF values were corrected for liquid-junction potentials according to the Henderson equation.[358] Activity coefficients were calculated with a two-parameter Debye–Hückel approximation.[359]

For detection limit optimization, all K^+ and Ag^+ measurements were performed with polypropylene beakers to minimize ion leaching from the sample container into the sample. In the case of the Ag^+ measurements, the beakers were cleaned overnight in 0.1 M HNO_3 before use.

3.2.5.2. Electrochemical Impedance Spectroscopy

All impedance experiments were performed on a Solartron 1255B frequency response analyzer with an SI 1287 electrochemical interface (Farnborough, Hampshire, U.K.) controlled by ZPlot software (Scribner Associates, Southern Pines, NC). ZView software was used to view and fit the data. The typical frequency range for the measurement was 200 kHz to 0.1 Hz. Measurements were performed at open circuit potential with an AC amplitude of 10 mV.

Measurements were performed under aqueous or nonaqueous conditions, depending on the type of electrode. For aqueous systems, a 0.1 M KCl solution was used as the electrolyte, with a double-junction Ag/AgCl reference electrode (with a 1.0 M LiOAc bridge electrolyte and AgCl-saturated 3.0 M KCl inner reference electrolyte) or a Ag/AgCl Luggin capillary filled with 3.0 M KCl. For nonaqueous systems, a 0.1 M solution of KPF_6 in acetonitrile was used as electrolyte, and a Luggin capillary filled with 3.0 M KCl was used as reference electrode. In all cases, a platinum wire served as the counter electrode.

3.2.5.3. Capacitance Measurements

To ensure complete wetting of the carbon during the capacitance experiments, a nonaqueous electrolyte (0.1 M KPF_6 in acetonitrile) was used. The nonaqueous reference electrode was a Ag wire in 0.1 M $AgPF_6$ in acetonitrile. A three-electrode setup was used for all experiments, with the carbon electrode as the working electrode, a Pt wire as the counter electrode, and the nonaqueous reference electrode. All experiments were carried out in a closed three-neck flask, and the electrolyte solution was purged with argon for at least 15 min prior to each measurement.

For cyclic voltammetry experiments, a potential window of 0.6 V centered around 0.0 V with a scan rate of 0.5 $mV \cdot s^{-1}$ was used. Three cycles were typically used, and the capacitance value was obtained from the third cycle. The capacitance was calculated by averaging the absolute value of the two current values at the center of the positive and negative sweep (typically 0.0 V). This average current was then divided by the scan rate and the mass of the electrode, giving a capacitance value in $F \cdot g^{-1}$.

For chronopotentiometry (which may also be referred to as constant-current charge-discharge) experiments, a constant current was applied to the electrode until an upper potential limit was reached (charge), at which time an equal but opposite current was applied until a lower potential limit was reached (discharge). The upper and lower potential limits were typically 0.2 and 0.0 V, respectively, for unoxidized carbon and 0.7 and 0.0 V, respectively, for oxidized carbon. The capacitance in F/g was determined by dividing the applied current by the mass of the electrode and by the slope of the discharge line in a potential versus time graph.

All cyclic voltammetry experiments were performed on an electrochemical analyzer (CH Instruments, Inc., Austin, TX). All charge/discharge experiments were performed on a Solartron 1255B frequency response analyzer with an SI 1287 electrochemical interface.

3.2.5.4. Scanning Electron Microscopy

For carbon not infiltrated with a PVC membrane, the samples were affixed on an aluminum stub with conductive carbon tabs. Imaging was carried out on a JEOL 6700 field emission gun scanning electron microscope with an accelerating voltage of 5.0 kV.

3.2.5.5. Cryo-Scanning Electron Microscopy

Due to the volatility of *o*-NPOE in high vacuum, electrodes were imaged using cryo-SEM on a Hitachi S-4700 cold field emission gun scanning electron microscope with an accelerating voltage of 3.0 kV. To prepare the electrodes for imaging, the membrane-covered pieces of 3DOM carbon were removed from the PVC substrate and Ni mesh metal contact. The membrane-covered carbon was mounted in the sample holder, which was then submerged in liquid nitrogen for quick freezing. From this point forward, the sample holder remained at liquid nitrogen temperature during the entire imaging process. After several minutes, the sample holder was transferred to a vacuum chamber and evacuated. The electrode was fractured to reveal a fresh cross section. A thin layer of Pt was then sputtered onto the membrane-coated carbon to improve its conductivity for imaging. The sample holder was transferred under vacuum to the microscope for imaging.

3.2.5.6. Elemental Analysis

C, H, N, O, and Cl elemental analyses were performed by Atlantic Microlab (Norcross, GA). For electrodes containing PVC membranes, the outer PVC membrane layer was removed prior to analysis and three electrodes were combined to supply sufficient material for each elemental analysis set.

3.2.5.7. Acid/Base Titrations to Determine Surface Functionality

The quantity of oxygen-containing surface functional groups was determined by a modified version of a published acid/base titration procedure.[56,135] Unoxidized 3DOM carbon and 3DOM carbon that had been oxidized for 10, 30, and 60 min were ground to powders to allow better mixing with the base solutions. The carbon samples were dried at 100 °C overnight, mixed with base, and then the excess of base was back-titrated with 0.025 M HCl using a mixed methyl red/bromocresol green end point indicator. Four types of base solutions were used to determine different types of surface functional groups: aqueous solutions of NaOH, Na_2CO_3, and $NaHCO_3$, as well as an ethanol solution of sodium ethoxide (all 0.05 M). In order to enhance the infiltration of the base solutions into the carbon, they were mixed under static vacuum. For each of the four carbon types (unoxidized and 10, 30, and 60 min oxidations), four 60 mg samples were placed in small plastic bottles and sealed with rubber septa. The bottles were then evacuated for 15 min, refilled with nitrogen, and evacuated for 15 more minutes. Then, 25 mL of a base solution was injected into each bottle using a syringe. The carbon was soaked in the base solutions for 2 days, swirling occasionally. After soaking, the base solutions were recovered by filtering the solutions through a 0.2 μm syringe filter and back-titrated.

3.2.5.8. Nitrogen Sorption

Nitrogen sorption measurements were carried out at 77 K. The unoxidized sample was evaluated after degassing overnight at 150 °C to 40 Pa using a Micromeritics ASAP 2000 system; the oxidized samples were tested on a Quantachrome Instruments Autosorb-1 system after degassing overnight at 150 °C to 13 Pa. The Brunauer-Emmett-Teller (BET) method was applied to calculate specific surface areas, and the pore sizes and volumes were estimated from the pore size distribution curves obtained from the adsorption branches of the isotherms.

3.3. Results and Discussion

3.3.1. Investigation of K^+ Sensor System with 3DOM Carbon Solid Contact

To characterize the novel solid-contact ISE with 3DOM carbon (Ni/3DOM carbon/PVC) as contact layer between a nickel metal lead and ionophore-doped PVC membranes, their ionic response, long-term drift characteristics, and the stability to redox and light interferences were determined. They are compared in the following to the responses of several other electrode setups. SC-ISEs with a layer of HOPG replacing the

3DOM carbon were prepared analogous to the 3DOM carbon-contacted ISEs and are referred to in the following as Ni/HOPG/PVC electrodes. SC-ISEs made of a Ni mesh covered directly with an ionophore-doped plasticized PVC membrane but without an intermediate layer (Ni/PVC) and a Ni mesh coated with 3DOM carbon but lacking the PVC membrane (Ni/3DOM carbon) were also investigated for comparison.

3.3.1.1. Ionic Response

The ionic responses of SC-ISEs with the different electrode assemblies were measured in KCl solutions. Calibration curves (Figure 3.3) were obtained by repeated dilution of the sample with pure water, starting from a 100 mM KCl solution. As predicted by theory for an electrode based on a solvent polymeric membrane doped with K^+-selective valinomycin as ionophore, the Ni/3DOM carbon/PVC electrode exhibited a Nernstian response to K^+. The observed detection limit of $10^{-6.2}$ M is similar to detection limits of SC-ISEs as observed in the past but could probably be lowered by preventing direct exposure of the electrode to solutions of high K^+ activity.[276]

While the Ni/HOPG/PVC and Ni/PVC electrodes lack the ion- and electron-conducting intermediate layer between the electron conductor (Ni) and ion conductor (PVC membrane) and would not be expected to give stable long-term responses, they did provide Nernstian responses to K^+ with slopes of 58.1 mV·decade^{-1} for the Ni/HOPG/PVC electrode in the range from $10^{-1.1}$ M to $10^{-5.2}$ M and 56.4 mV·decade^{-1} for the Ni/PVC electrode in the range from $10^{-1.1}$ M to $10^{-5.5}$ M. This can be explained by the short time span required for the measurement of a calibration curve and is consistent with previous observations for comparable CWEs (see above). More surprising was the response of the Ni/3DOM carbon electrode, which exhibited a slope of 48.6 mV·decade^{-1} in the range from $10^{-1.1}$ M to $10^{-4.3}$ M. This response may be related to K^+ intercalation into 3DOM carbon or very low concentrations of oxygen-containing functional groups on the surface of 3DOM carbon.[56]

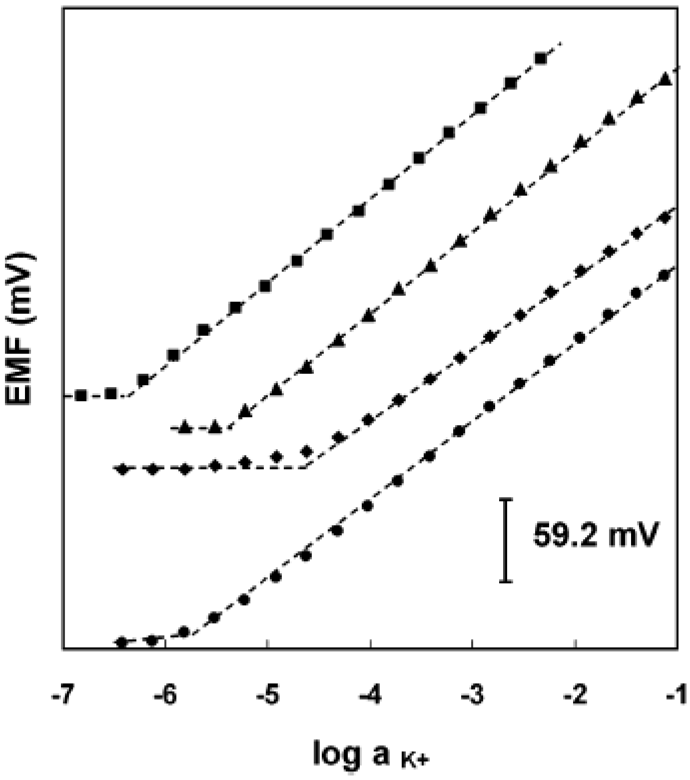

Figure 3.3. Potentiometric K^+ response curves of SC-ISEs with different electrode assemblies in KCl solutions: (■) Ni/3DOM carbon/PVC, (▲) Ni/HOPG/PVC, (♦) Ni/3DOM carbon, (●) Ni/PVC. For clarity, response curves have been shifted vertically relative to one another.

3.3.1.2. Redox Response

For each electrode assembly, the redox interference was investigated by measuring the cell potential in solutions of the redox couple Fe(III) and Fe(II) in various ratios with a constant ionic strength (100 mM KCl). The sum of the concentrations of Fe(II) and Fe(III) was kept constant (1 mM), and the Fe(II)/Fe(III) ratio was changed from 4:1 to 1:4. The results are shown in Table 3.1. A Nernstian response to the Fe(II)/Fe(III) redox couple was observed at the 3DOM carbon-coated Ni electrode because 3DOM carbon is an electron conductor and can be considered as an extension of the Ni electrode. Evidently, this redox response would be considered an interference for an SC-ISE. In contrast, all electrodes coated with PVC membranes showed no redox interference, which is consistent with the lack of electron transport through the valinomycin- doped plasticized PVC membranes.

Table 3.1. Redox response of different electrode assemblies as given by the slope of the EMF versus log([Fe(III)]/[Fe(II)]).

Substrate	**Slope (mV·decade^{-1})**
Ni/3DOM carbon	57.2 ± 0.2
Ni/3DOM carbon/PVC	1.43 ± 0.40
Ni/HOPG/PVC	0.70
Ni/PVC	4.16

3.3.1.3. Potential Stability

The potential stability of all SC-ISEs was studied by comparing the potential drift for different electrode assemblies in 100 mM KCl solution at a constant temperature (25 °C) controlled with a thermostat. To assess the contribution of the reference electrode to the measured potentials, the potential of one reference electrode was measured relative to a second identical reference electrode. This measurement showed a residual drift of 7.5 $\mu V \cdot h^{-1}$ over 80 h. While this value is not the drift associated with one individual reference electrode, it suggests that the residual drift associated with one reference electrode is at least on the order of 7.5 $\mu V \cdot h^{-1}$. In comparison, the potentials of 3DOM carbon-contacted ISEs relative to the same reference electrode were very stable (see Table 3.2). Their potential drifts over 70 h were only 11.7 ± 1.0 $\mu V \cdot h^{-1}$ or 0.28 ± 0.02 $mV \cdot day^{-1}$ (average for three electrodes). The potential stabilities were rechecked after the electrodes were kept in 100 mM KCl solution for 1 month. The potential drift of the 3DOM carbon-contacted ISE was still very small (10.8 $\mu V \cdot h^{-1}$ over 185 h), while the potential drift of the Ni/HOPG/PVC electrode worsened further (from 77.0 $\mu V \cdot h^{-1}$ over 96 h to 114.6 $\mu V \cdot h^{-1}$ over 144 h).

Table 3.2. Potential stability of different freshly prepared electrode assemblies in 100 mM KCl solution.

Substrate	**Drift ($\mu V \cdot h^{-1}$)**
Ni/3DOM carbon	210 (over 96 h)
Ni/3DOM carbon/PVC	11.7 (over 70 h)
Ni/HOPG/PVC	77.0 (over 96 h)
Ni/PVC	280 (over 144 h)

Other solid contacts that have been reported to be used in SC-ISEs exhibited significantly larger potential drift, e.g., the potential drifts were 30 $\mu V \cdot h^{-1}$ (over 72 h) and 100 $\mu V \cdot h^{-1}$ (over 72 h) for PPy- and hydrogel-contacted ISEs, respectively.[273] In contrast, the potential drift of the electrode with HOPG as the intermediate is much larger (77.0 $\mu V \cdot h^{-1}$), indicating the presence of a "blocked" interface due to the absence of an ion/electron conductor. With 280.0 $\mu V \cdot h^{-1}$, the potential drift of the Ni/PVC electrode between the polymeric membrane and the Ni electrode was even worse.

The high stability of the 3DOM carbon-contacted SC-ISEs reported here is related to the bicontinuous electron- and ion-conducting structure of the interlayer. On one hand, the well-interconnected wall structure of the 3DOM carbon provides a continuous pathway for electron conduction. On the other hand, ionic conductivity is provided by a continuous network of interconnected pores that are filled with the ionophore-doped solvent polymeric phase containing the cationic valinomycin complexes and the tetrakis-[3,5-bis(trifluoromethyl)phenyl]borate as ionic species.[56,239] The 3DOM carbon/polymer composite interlayer shares the mixed ion- and electron-conducting property with semiconducting polymers but lacks the photon sensitivity and surface hydrophilicity that many of the latter exhibit. Moreover, the bicontinuity of the two phases appears to be an excellent means to prevent delamination of the electron and the ion conductor.

3.3.1.4. Effect of Oxygen and Carbon Dioxide on the Potential Stability

Interferences from O_2 and CO_2 have been reported for several SC-ISEs. Both gases can easily permeate through the polymeric membrane. While CO_2 can affect the local pH at the surface of the metal contact (or more generally, the electron conductor), it has been reported that the formation of an oxygen half-cell can affect the phase boundary potential at that surface.[336] The PPy-contacted ISEs show different levels of interference from O_2 depending on the type of doping ion and the PPy film thickness.[266,282]

In this study, a possible interference of O_2 on the K^+ response was tested by immersion of the electrodes into 100 mM KCl solution and alternating saturation of the solution with O_2 and Ar by bubbling the respective gas into the solution while recording the electrode potentials. As shown in Figure 3.4, a small potential increase of 0.82 ± 0.02 mV was observed upon O_2 exposure of 3DOM carbon-contacted electrodes. Figure 3.4 also shows a -2.6 ± 0.1 mV drift over 30 min for a HOPG-contacted electrode, which is more than 3 times larger than for the 3DOM-contacted electrode but still better than expected in the presence of an ill-defined interfacial potential. Indeed, even for a PPy-coated glassy carbon electrode coated with a valinomycin-doped solvent polymeric membrane, a drift of 25 $mV \cdot h^{-1}$ was reported in the literature.[282]

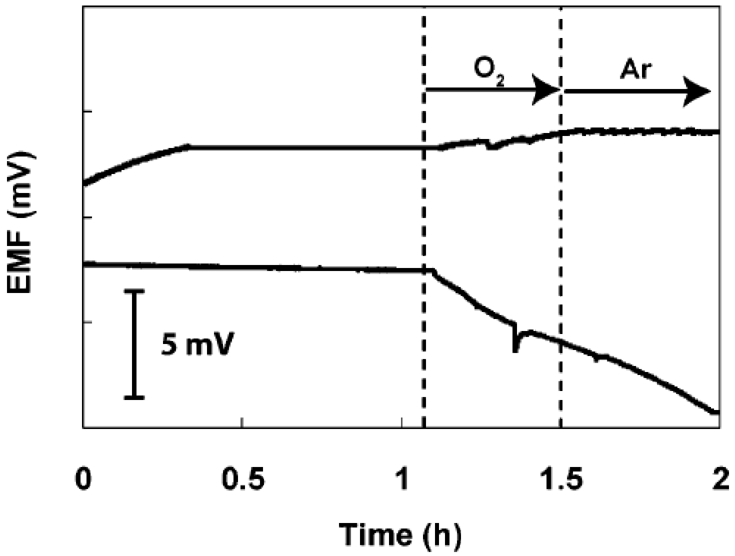

Figure 3.4. Effect of oxygen on the potential stability of SC-ISEs with different electrode assemblies in 100 mM KCl solution: (top) Ni/3DOM carbon/PVC, (bottom) Ni/HOPG/PVC.

CO_2 has been shown to interfere with SC-ISEs by altering the local pH at the solid contact.[284-289,341] For this study, the effect of CO_2 on the K^+ response was determined by bubbling CO_2 emitted from dry ice into a 100 mM KCl solution (see Figure 3.5). Both the 3DOM carbon- and the HOPG-contacted ISE show a larger potential drift (11.8 ± 1.5 mV·h^{-1} and 12.8 ± 1.6 mV·h^{-1}, respectively) than in the case of O_2. The sensitivity to CO_2 of the 3DOM carbon-contacted ISE is of the same magnitude as for poly(3,4-ethylenedioxythiophene)-contacted SC-ISEs (8 to ~10 mV·h^{-1}) and less than for PPy-contacted electrodes (25 to ~30 mV·h^{-1}).[282]

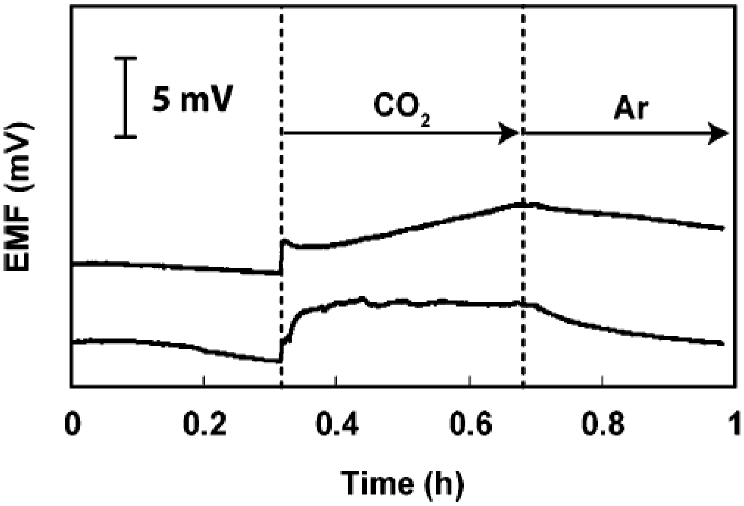

Figure 3.5. Effect of carbon dioxide on the potential stability of SC-ISEs with different electrode assemblies: (top) Ni/3DOM carbon/PVC, (bottom) Ni/HOPG/PVC.

3.3.1.5. Test for an Aqueous Layer at the 3DOM Surface

The formation of an aqueous layer between the polymeric sensing membrane and the underlying contact, as for example reported for highly plasticized PVC membranes with PPy contacts, not only causes mechanical failure but also leads to chemical hysteresis caused by the distribution of ions or carbon dioxide into this aqueous layer. Fibbioli *et al.* suggested that such a thin aqueous layer was the main source of potential instability of SC-ISEs and proposed a method to test for the presence of such an aqueous layer.[360] Potential drifts upon replacing the primary ions in the measuring solution with discriminated interfering ions, or the reverse, are indicative of the presence of an aqueous layer between the solid contact and the membrane. The presence of an aqueous layer is indicated by a positive potential drift when changing from primary ions to interfering ions and a negative potential drift when changing from interfering ions to primary ions.

This can be explained by transport of the relevant ions from the sample through the ionophore-doped membrane into the aqueous layer and vice versa.

Corresponding experiments were carried out for SC-ISEs with 3DOM carbon as the solid contact (Figure 3.6). Upon conditioning of electrodes in 100 mM KCl solution for 24 h, the solution was changed to 100 mM NaCl. As soon as the solution was changed, an instantaneous EMF shift of –220 mV was observed (curve A). This is caused by the change in the phase boundary potential at the PVC/outer sample solution interface and reflects the membrane selectivity. Over the next several hours, a positive drift was observed (curve A). However, no negative potential drift was observed when the sample solution was changed back to 100 mM KCl. On the basis of the theory of Fibbioli *et al.*, the existence of an aqueous layer would be indicated by a positive potential drift when changing from K^+ to Na^+ and a negative potential drift when changing back from Na+ to K^+ (see, e.g., Figure 3 in Fibbioli, *et al.*[360]). Evidently, our results differ from what is expected as there is no drift on the return to K^+. To understand the reason for the positive potential drifts, the potential was recorded while the electrode was kept in 100 mM KCl solution for 24 h, and the solution was then changed to 100 mM NaCl solution, followed by repeated replacement of the solution with fresh 100 mM NaCl every 60 min (Figure 3.6, curve B). Each time the NaCl solution was replaced, a drop of potential was observed, indicating a contamination of the NaCl solution with K^+ continuously leaching from the PVC membrane. This is the main reason for the potential drifts upon changing to NaCl solution. The only evidence that might indicate an aqueous layer is that the potential upon return to 100 mM KCl is 4 mV higher than for the initial KCl solution and that there is some carbon dioxide interference (see above). The comparatively small size of both effects suggests that the hydrophobic surface of 3DOM carbon as prepared in this study suppresses the formation of an aqueous layer.

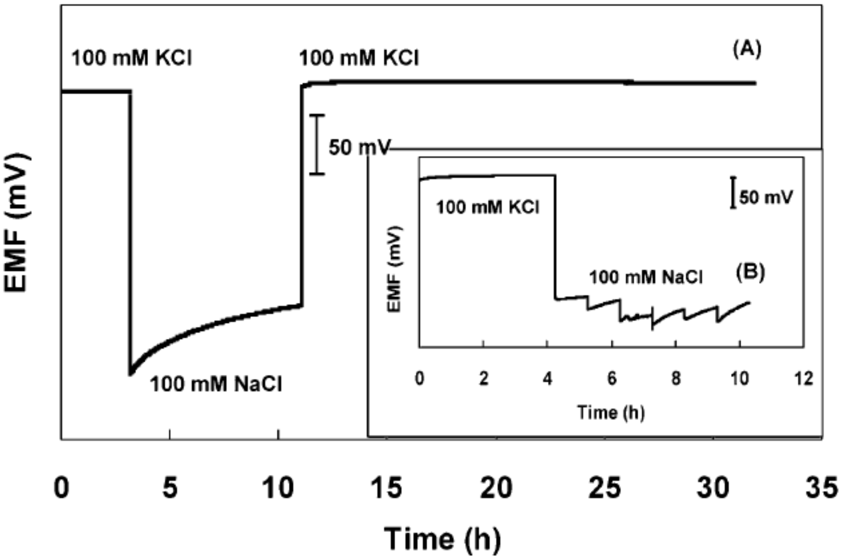

Figure 3.6. Response of a 3DOM carbon-contacted K^+-selective electrode: (A) At *t* = 3.2 h, the conditioning solution (100 mM KCl) was exchanged for 100 mM NaCl; at *t* = 11.0 h, the sample was replaced by the conditioning solution. (B) At *t* = 4.3 h, the conditioning solution (100 mM KCl) was exchanged for 100 mM NaCl, which was then replaced five times by fresh 100 mM NaCl solution in intervals of 60 min.

3.3.1.6. Effect of Ambient Light on the Potential Stability

SC-ISEs can be photoresponsive if the intermediate layer between the polymeric membrane and the underlying metal electrode is an organic semiconductor with a suitable band gap. To investigate the light sensitivity, electrodes prepared in this study were immersed into a 100 mM KCl solution. Continuously recorded potentials are presented in Figure 3.7. During the experiment, the whole electrochemical cell was kept in the dark until the electrodes were exposed either to a flashlight for 6 min or to ambient room light for 20 min, followed each time by a return to the dark. In both experiments, no significant drift was observed, indicating that the 3DOM carbon-based layer is insensitive to light.

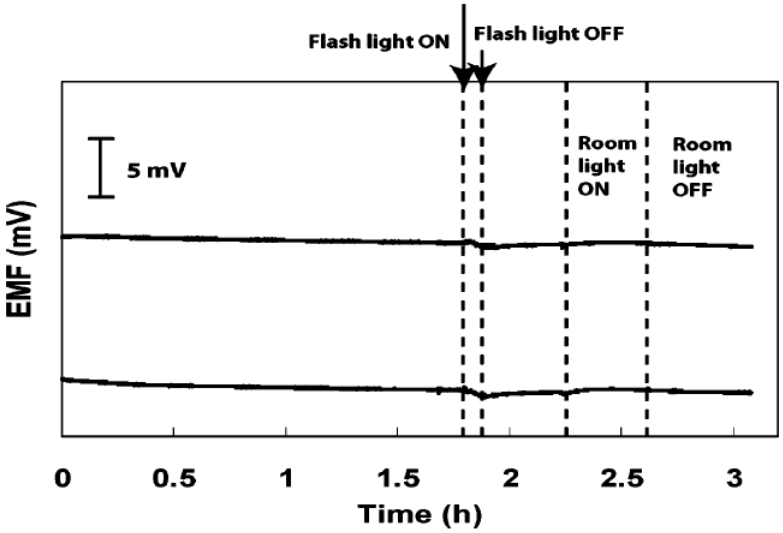

Figure 3.7. Effect of light on the potential stability of SC-ISEs with different electrode assemblies in 100 mM KCl solution: (top) Ni/3DOM carbon/PVC, (bottom) Ni/HOPG/PVC.

3.3.2. Optimization of Sensor System for Improved Detection Limit

3.3.2.1. K^+-Selective Electrodes

As shown above, K^+ selective 3DOM carbon-contacted ISEs exhibited excellent long-term stability with potential drifts of only 11.7 $\mu V \cdot h^{-1}$ and a very good resistance to the interference from oxygen and light.[262] Moreover, the hydrophobic surface of 3DOM carbon suppressed the formation of an aqueous layer. While a detection limit of 6.3×10^{-7} M for K^+ was reported, it was suspected that the detection limit could be improved by more carefully preventing direct exposure of the electrode membrane to solutions of high K^+ concentration.[262] This is indeed the case, as shown in the following.

When freshly prepared electrodes were first conditioned in 1 μM KCl solution for 1 day and then transferred to 1 mM KCl solutions for the measurement of calibration curves by successive sample dilution, a detection limit for K^+ of 1.0×10^{-6} M was observed. Similarly, conditioning in 1 nM KCl solution for 2 days and calibration curve measurements by dilution of 1 mM KCl gave the nearly identical detection limit of 1.2×10^{-6} M. This suggests that any effect from the low concentration of the conditioning solution is overpowered by the 1 mM KCl concentration that the electrode is first exposed to when the calibration curve is measured by successive dilution. Therefore, calibration curves were determined with the successive sample dilution method, starting from different KCl concentrations (see Figure 3.8 and Table 3.3). Clearly, lower detection limits were obtained for lower concentrations of the conditioning and sample solutions. The best detection limit, 1.6×10^{-7} M, was obtained with a 1 μM conditioning solution and a calibration curve obtained by successive dilution of a 1 μM K^+ starting solution. The use of high concentrations of the analyte ion in the conditioning solution is apparently followed by a release of analyte ions from the membrane phase back into the sample when the membrane is exposed to more dilute solutions.

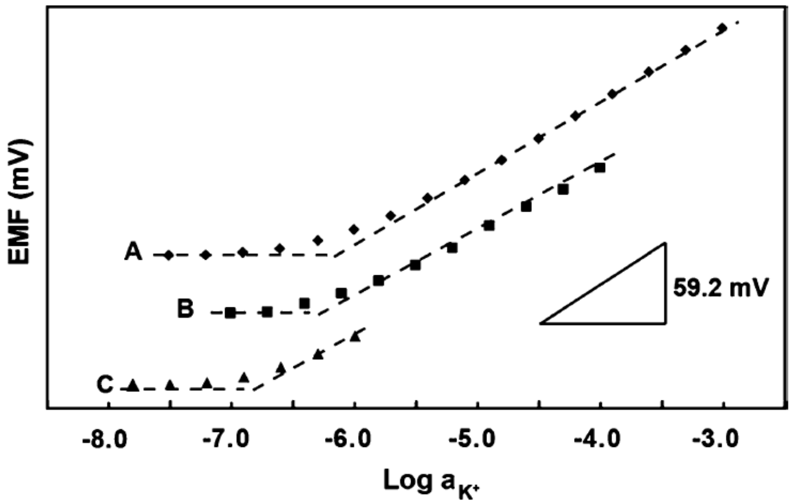

Figure 3.8. Potassium ion calibration curves for K^+-selective ISEs recorded: Conditioning in (A) 1 mM KCl for 1 day, (B) 0.1 mM KCl for 1 day, and (C) 1 μM KCl for 1 day. For clarity, response curves have been shifted vertically relative to one another.

Table 3.3. Detection limits achieved for K^+ with different concentrations of conditioning and starting solutions.

Conditioning solution (M)	Starting solution (M)	Detection limit (M)
10^{-6}	10^{-3}	1.0×10^{-6}
10^{-9}	10^{-3}	1.2×10^{-6}
10^{-3}	10^{-4}	6.3×10^{-7}
10^{-4}	10^{-4}	4.0×10^{-7}
10^{-6}	10^{-6}	1.6×10^{-7}

The K^+ SC-ISEs presented here compare well to previously reported ones. For example, solid-contact K^+ ISEs with polypyrrole intermediate layers, electropolymerized in the presence of the water-soluble hexacyanoferrate, exhibited a 1.2×10^{-7} M detection limit.[346] Chumbimuni-Torres and coworkers reported a detection limit for K^+ at 1×10^{-7} M for electrodes with a plasticizer-free copolymer as the membrane matrix and poly(3-octylthiophene) as the intermediate layer.[280] In comparison, the lowest detection limit reported thus far for any ISE was $\sim 5.0 \times 10^{-9}$ M for a K^+ ISE with an inner filling solution in equilibrium with an ion-exchange resin buffering the activity of the primary ion.[330] It appears that, independent of the approach, very similar detection limits are observed for all SC-ISEs. This may be the result of sample contamination with K^+ from ambient sources. Only clean room conditions are likely to exclude the possibility of ambient K^+ contamination.

3.3.2.2. Optimization of Ag^+-Selective Electrode System

In order to eliminate the effects of ambient K^+ contamination, further tests of the low detection limits of 3DOM carbon-contacted ISEs were performed with Ag^+ ISEs. Silver is not only a ubiquitous contaminant, but its determination is also of practical interest. Due to their antibacterial properties, silver salts are used in the disinfection of drinking water, as well as in implanted prostheses. The amount of silver entering the aquatic system and the atmosphere each year is estimated to be as high as 450,000 kg. Although very small portions of the total silver is biologically available in water, a concentration higher than 0.17 $\mu g \cdot L^{-1}$ is toxic to fish and microorganisms, making it crucial to monitor the concentration of silver in the environment.[361]

SC-ISEs for Ag^+ have been used previously,[362,363] however, it was not until 2006 that Bakker and co-workers reported on the first SC-ISE for Ag^+ with a detection limit in the nanomolar range. In a report on trace level measurements of five different ions, they described detection limits for Ag^+ of 2.0×10^{-9} M for a SC-ISE with *o*-xylylenebis(N, N-diisobutyldithiocarbamate) as ionophore.[280] In the work with 3DOM carbon-contacted ISEs reported here, the same ionophore has been used, and different factors that affect the detection limit were studied. These include the polymer content, the molar ratio of ionophore and ionic sites, the concentration of the conditioning solution, and the concentration range of the calibration curves.

3.3.2.2.1. Polymer Content

The choice of the polymer content of a PVC-based membrane is a trade-off. On one hand, a higher polymer content decreases the diffusion of ions through the membrane, which is helpful for lowering ion fluxes and, thereby, detection limits. The diffusion coefficients in the membrane can be strongly varied by changing the concentration ratio of polymer to plasticizer.[364,365] An increase of the polymer content of the membrane from the usual value of 30% to 50% (w/w) has been reported to improve the detection limit for calcium from the micromolar down to the nanomolar range.[366] On the other hand, increasing the polymer content of the sensing membrane increases its electrical resistance, and eventually makes it impossible to carry out potentiometric experiments. In this study, the polymer content of *o*-NPOE/PVC membranes was varied from 33% to 75%. All electrodes were conditioned in 1 nM $AgNO_3$ for 2 days, and calibration curves were measured by dilution of 0.1 mM $AgNO_3$ solutions. The thus obtained detection limits are listed in Table 3.4. Clearly, membranes with a higher polymer content provided lower detection limits. With 75% PVC, the electrodes responded to Ag^+ down to the nanomolar level, which was two orders of magnitude lower than for the membranes with 33% PVC. This is consistent with the observation that the resistance of a 33% PVC membrane (5.1×10^5 Ω) was approximately two orders of magnitude lower than the resistance of a 75% PVC membranes (1.7×10^8 Ω).

Table 3.4. Detection limits for Ag^+ upon optimization of the sensing membranes and the experimental protocol.

Polymer content (wt %)[a]	33	43	66	70	75
Detection limit (M)	1.0×10^{-7}	3.1×10^{-8}	1.8×10^{-8}	7.2×10^{-9}	3.7×10^{-9}
Molar ratio of ionophore and ionic sites[b]	3.2 : 1.0	2.1 : 1.0			
Detection limit (M)	1.6×10^{-8}	3.7×10^{-8}			
Conditioning solution (M)[c]	1 mM $AgNO_3$ (1 d)	1 nM $AgNO_3$ (1 d)	1 nM $AgNO_3$ (2 d)		
Detection limit (M)	1.1×10^{-7}	4.3×10^{-8}	4.0×10^{-8}		
Starting concentration of $AgNO_3$ (M)[d]	1.0×10^{-4}	1.0×10^{-6}	1.0×10^{-8}		
Detection limit (M)	4.0×10^{-8}	8.0×10^{-9}	7.9×10^{-11}		

[a] Molar ratio of ionophore and ionic sites 2.1 : 1.0. Electrodes conditioned in 1 nM $AgNO_3$ solution for 2 days. Calibration curves measured by dilution of 0.1 mM $AgNO_3$.

[b] Polymer content 43%. Conditioning and calibration curve procedure as described in footnote a.

[c] Polymer content 43%. Molar ratio of ionophore and ionic sites 3.2 : 1.0. After conditioning in different solutions, calibration curves measured by dilution of 0.1 mM $AgNO_3$ solutions.

[d] Membrane components as for c. All electrodes conditioned in 1 nM $AgNO_3$ solution for 1 day.

3.3.2.2.2. Molar Ratio of Ionophore and Ionic Sites

The molar ratio of ionophore and ionic sites is well known to affect the selectivities[367,368] and, thereby, the detection limits of ISEs. For a given concentration of interfering ions, electrodes with better selectivities can detect the primary ion at lower concentrations. Moreover, the ionophore and ionic sites are buffering the primary ion activity in the sensing membrane, stronger binding of the primary ion to the ionophore resulting in a lower primary ion activity in the membrane. Under circumstances where the detection limit is not determined by interfering ions but by the release of primary ions from the membrane into the sample, a lower primary ion activity in the membrane is also expected to result in a lower detection limit. Therefore, if the concentration of ionic sites is kept constant while the ionophore concentration in the sensing membrane is increased and, thereby the concentration of free analyte ions in the sensing membrane decreases, the detection limit is expected to improve. Experimentally, the molar ratio of the Ag^+ ionophore *o*-xylylenebis(N,N-diisobutyldithiocarbamate) and the ionic sites in the sensing membrane was varied, while the weight percentages of PVC, *o*-NPOE and NaTFPB were kept constant at 43%, 56% and 1%, respectively. Two molar ratios of ionophore and ionic sites, i.e., 3.2 : 1.0 and 2.1 : 1.0, were tested. All electrodes were conditioned in 1 nM $AgNO_3$ for 2 days, and calibration curves were obtained by successive dilution of 0.1 mM $AgNO_3$. With the ratio of ionophore to ionic site ratio of 3.2 : 1.0, the detection limit was 1.6×10^{-8} M, which was approximately two times better than for electrodes with the ionophore: ionic site ratio of 2.1 : 1.0 (Table 3.4). This seems to be consistent with the fact that the activity of Ag^+ in the membranes with the 3.2 : 1.0

ionophore to site ratio is calculated from the known 1 : 1 binding constants to be two times lower than in the membranes with the 2.1 : 1.0 ratio.[369]

3.3.2.2.3. Conditioning Solutions and Starting Solutions

As the above mentioned results for K^+ show, different conditioning solutions and starting solutions strongly affect the detection limits. To investigate these effects, membranes containing 43% PVC and a 3.2 : 1.0 molar ratio of ionophore and ionic sites were used, and calibration curves were measured by successive dilution, starting with 0.1 mM $AgNO_3$ solutions. Conditioning for 1 day in 1 nM solutions gave a detection limit of 4.0×10^{-8} M, which was approximately four times lower than when conditioning was performed with a 1 mM $AgNO_3$ solution. Conditioning in 1 nM $AgNO_3$ for one additional day did not further improve the detection limit. For this lower concentration of the conditioning solution of 1 nM, different concentrations of starting solutions were subsequently investigated, i.e., 0.1 mM, 1 μM, and 10 nM. As expected, the lower the concentration of the starting solution, the lower the detection limit that could be achieved. With a starting solution containing 10 nM $AgNO_3$, the detection limit was 7.9×10^{-11} M, which is about three and two orders of magnitude lower than the results for the 0.1 mM and 1 μM starting solutions, respectively (see Table 3.4).

3.3.2.2.4. Combination of Best Conditions for Low Detection Limit

The best conditions for low detection limit detection of Ag^+ were selected based on a combination of the relevant experimental parameters. In this experiment, the sensing membrane was composed of 75% PVC, and the molar ratio of ionophore and ionic sites was 3.2 : 1.0. The electrode was conditioned in 1 L of 1 μM $AgNO_3$ for 1 day to ensure complete Na^+/Ag^+ exchange between the sample and the sensing membrane. Subsequently, the membrane was conditioned in 1 nM $AgNO_3$ for 2 days. Then the electrode was immersed into 500 mL of a 10 nM $AgNO_3$ solution for the measurement of a calibration curve by successive dilution (see Figure 3.9). The thus obtained detection limit was 4.0×10^{-11} M, or 4.3 ppt for Ag^+, which is more than two orders of magnitude lower than for the previously reported SC-ISEs based on a plasticizer-free methyl methacrylate–decyl methacrylate copolymer matrix.[280] As shown by others previously, this two-step conditioning procedure starting with a relatively high concentration of analyte in the first step ensures that even a limited volume of conditioning solution contains enough analyte ions to fill the sensing membrane by ion-exchange with primary ions, while the second step with the solution of much lower primary ion activity removes excess primary ion from the sensing membrane that may have entered in there due to co-extraction. Once the ion exchange is performed this way, the electrodes can be stored in the conditioning solution of lower primary ion activity and used without further preparatory steps.

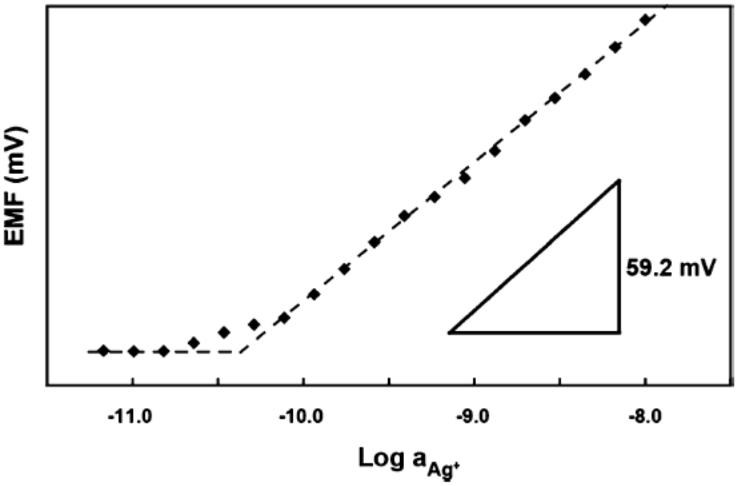

Figure 3.9. Silver ion calibration curve for Ag^+-selective electrode, with the lowest detection limit achieved in this work, recorded after conditioning in 1 μM $AgNO_3$ for 1 day and 1 nM $AgNO_3$ for 2 days.

3.3.3. Effects of Architecture and Surface Chemistry of 3DOM Carbon Solid Contacts on Performance of ISEs

The ISEs with 3DOM carbon solid contacts described above exhibit excellent detection limits and long-term stabilities. The reasons for this remarkable performance were studied by investigating the effects of changing the carbon architecture and surface area of K^+-selective electrodes. The electrodes were prepared by affixing a valinomycin-containing plasticized PVC sensing membrane over carbon solid contacts attached to a Ni mesh as metal contact. As in the work described above, 3DOM carbon, with walls of glassy carbon surrounding an array of interconnected macropores, was the primary solid contact used. For comparison, oxidized 3DOM carbon and an untemplated carbon prepared from the same precursor as the 3DOM carbon were also used as solid contacts for polymeric sensing membranes. The properties of the ISEs with 3DOM carbon solid contacts were investigated by examining their structure, capacitance, and the surface chemistry of the unoxidized and oxidized 3DOM carbon and by performing electrochemical impedance spectroscopy on several types of electrode constructs.

3.3.3.1. Electrode Structure

Cryo-SEM analysis of 3DOM carbon/ PVC electrodes was performed to ensure that the plasticized PVC membranes wetted the carbon monoliths and to qualitatively evaluate the degree of infiltration of the membranes into the pores of the carbon. SEM images of pristine 3DOM carbon and an electrode with a sensing membrane containing 33 wt % PVC are shown in Figure 3.10. SEM images of electrodes with sensing membranes containing 43 and 66 wt % PVC are provided in Figure 3.11. The sensing membranes coat the pore walls of each monolith and in some cases completely fill part of the pore structure, creating a bicontinuous carbon/ membrane structure. For all electrodes, the plasticized polymer is distributed throughout the entire thickness of the monolith, facilitating charge transport through the entire construct. Importantly, the penetration of the polymeric phase deep into the porous 3DOM carbon provides a large interfacial area between the polymeric sensing membrane and the carbon.

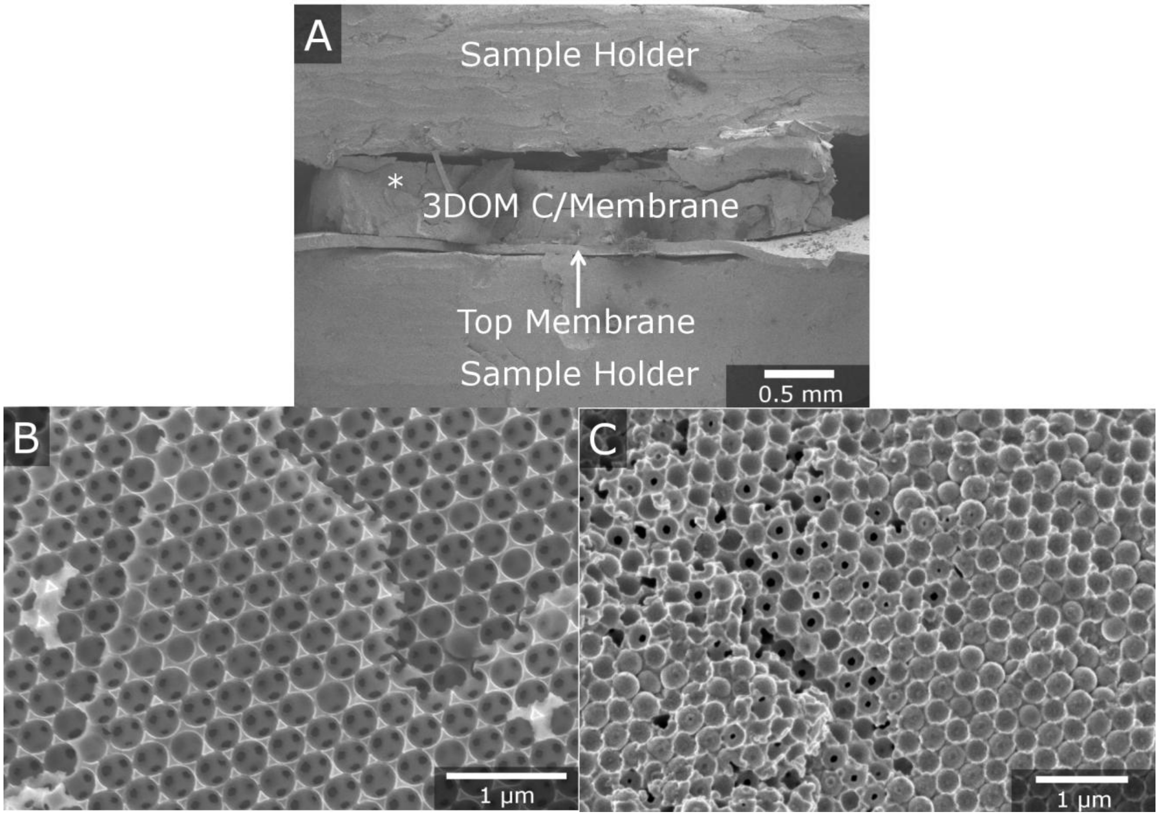

Figure 3.10. SEM images of (A) a membrane-infiltrated 3DOM carbon electrode mounted in a sample holder and cross sections of 3DOM carbon without (B) and with (C) the infiltrated sensing membrane material. The labels in image A indicate the locations of the membrane-infiltrated 3DOM carbon electrode and the top membrane sandwiched in the sample holder. The * indicates the location from which image C was obtained. The PVC content in the as-prepared sensing membrane in image C was 33 wt %.

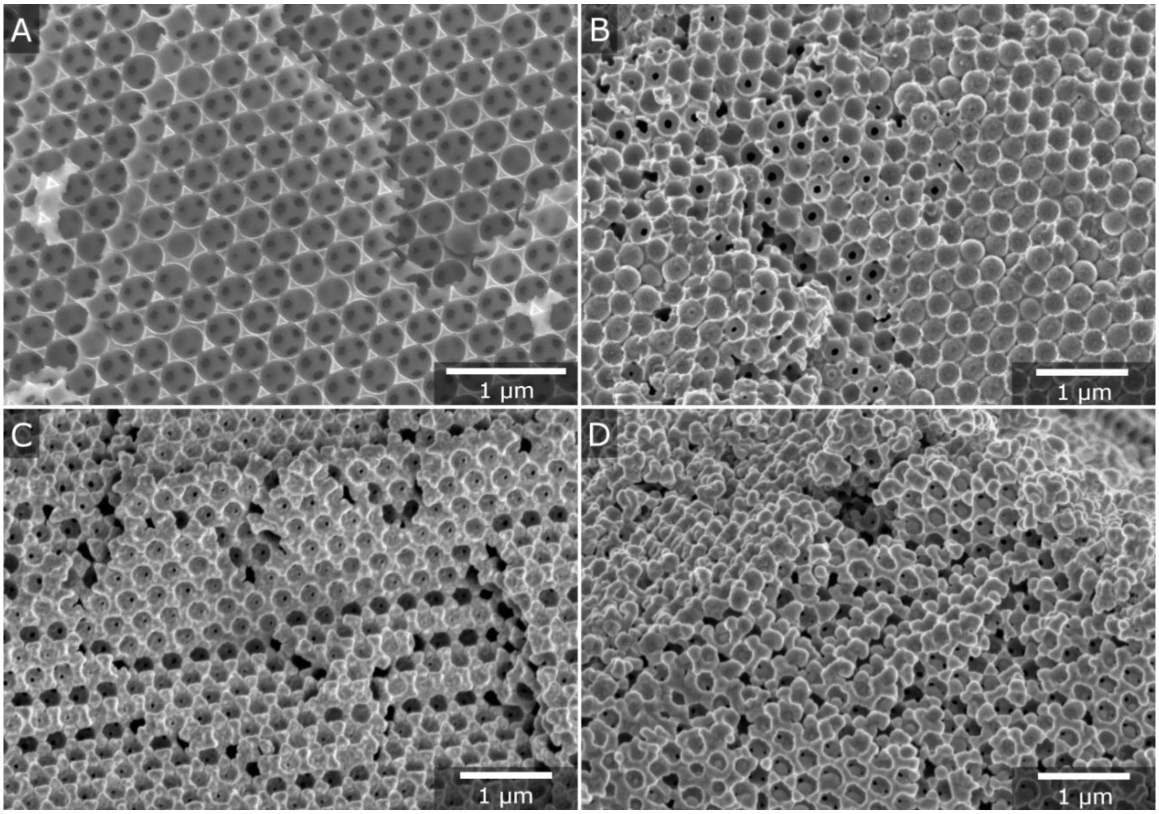

Figure 3.11. SEM images of 3DOM carbon without (A) and with (B–D) a PVC membrane. The PVC content of the membranes was (B) 33%, (C) 43% and (D) 66%. The membranes also contain 0.6 wt % ionic sites (NaTFPB), 1 wt % ionophore (valinomycin), and the remainder plasticizer (*o*-NPOE).

However, by examination of the cryo-SEM images alone, it is not possible to determine whether the infiltrated membrane has the same composition as the prepared membrane, or whether the membranes demix and one component (PVC or plasticizer) preferentially enters the 3DOM carbon monoliths. Therefore, elemental analysis was performed on electrodes whose outer membrane layer had been removed in order to determine the composition of the membrane that had infiltrated into the 3DOM carbon monoliths. For this purpose, electrodes fabricated with sensing membranes containing 33, 43, 66, and 74 wt % polymer were analyzed. Elemental analysis data of bare 3DOM carbon (without PVC membrane) are provided in Table 3.5 for comparison. The chlorine and nitrogen contents were used to determine the compositions of the infiltrated membranes since chlorine and nitrogen are present only in the PVC and the plasticizer *o*-NPOE, respectively. Whereas the PVC content of the as-prepared membranes ranged from 33–74 wt %, the PVC content of the infiltrated membranes ranged from 11–54 wt % (see Table 3.5). The actual PVC contents of the infiltrated membrane material are lower for each system than for the as-prepared membranes, with the largest difference in the electrode with 33 wt % PVC in the as-prepared membrane. This shows that during the preparation of the electrodes, the membranes demix, with the lower viscosity component *o*-NPOE preferentially entering the pores of the carbon. Indeed, separation of plasticizer and PVC in ISE sensing membranes has previously been observed at the surface of similar types of membranes.[370,371] However, in the case of the 3DOM carbon electrodes, the limited extent of demixing ensures that PVC enters the pores of the solid contact, thereby inhibiting delamination of the sensing membrane overlayer.

Table 3.5. Elemental analysis data for 3DOM carbon constructs upon infiltration with polymeric sensing membranes of varying PVC contents (three samples for each PVC content) and for 3DOM carbon without a PVC membrane as a comparison.

PVC content in as-prepared membrane (wt %)	**C (wt %)[a]**	**H (wt %)**	**N (wt %)**	**O (wt %)**	**Cl (wt %)**	**PVC content in infiltrated membrane (wt %)[b]**
(3DOM C only)	92.95	0.27	0.00	2.13		
33	81.02	2.40	1.28	12.48	1.67	11
43	85.20	1.55	0.51	6.25	2.53	32
55	83.68	1.69	0.36	8.75	3.11	45
74	80.33	1.83	0.29	8.86	3.54	54

[a] All elemental analysis values are ±0.3% according to Atlantic Microlab.

[b] The PVC contents of the infiltrated membranes are calculated from the nitrogen and chlorine contents of the electrodes.

The elemental analysis data was also used to estimate the extent of infiltration of the sensing membrane material into the 3DOM carbon monoliths. The filling fraction of the sensing membrane material in the pores of the 3DOM carbon monolith was obtained for each of the different membrane compositions. Volume fractions of 26% carbon and 74% macropore volume were assumed for the 3DOM carbon solid contact (the theoretical values for a face-centered cubic array of spheres). The densities of 3DOM carbon, PVC, and *o*-NPOE as well as the PVC content of the infiltrated membranes (as calculated above and shown in Table 3.5) were used to estimate the filling fraction of the membrane in the void space of the 3DOM carbon skeleton. The filling fraction decreased as the PVC content of the membrane increased, ranging from 25% for the as-prepared membrane containing 33 wt % PVC to approximately 9% for the as-prepared membranes containing 43, 66, and 74 wt % PVC. Importantly, as shown by the cryo-SEM data discussed above, this membrane material in the voids is coating the surface of the 3DOM carbon pores. Even though one may conceive of methods of filling the pores to a greater extent, here we chose to use the same methods as described above to help our understanding of the excellent performance of this system.

3.3.3.2. Surface Chemistry of 3DOM Carbon

In order to investigate if there is a relationship between the initial potential ($E°$) of the electrodes and the surface chemistry of the 3DOM carbon, $E°$ of SC-ISEs with 3DOM carbon contacts containing different amounts of surface functional groups was measured. For this purpose, a series of 3DOM carbon samples oxidized for varying amounts of time (0, 10, 30, and 60 min) was prepared. Oxidation of the 3DOM carbon increases the overall surface area and pore volume, largely through the generation of new micropores (Table 3.6). Acid/base titrations with four different bases were used to determine the quantity of different oxygen-containing surface functional groups for each sample by mixing each base with the 3DOM carbon and allowing them to react with the surface functional groups. After filtering the carbon out, the bases were back-titrated to determine the change in concentration. As Table 3.7 shows, the number of surface functional groups increases with the time of 3DOM carbon oxidation. The largest increase is observed in the number of carboxylic acid groups, which can provide the surface with negative charges.

Four sets of electrodes with 3DOM carbon solid contacts with different levels of oxidation (0, 10, 30, and 60 min) were fabricated with sensing membranes containing 33 wt % PVC (three or four electrodes for each oxidation level). Each set of electrodes was prepared using the same master membrane, and each of the four master membranes was prepared in an identical manner from the same THF solution of the membrane components. The average *E*° value for each set of electrodes (after conditioning) is shown in Table 3.7. The initial potential for electrodes prepared with oxidized carbon is higher than that of the electrodes prepared with unoxidized carbon. While the ranges of the *E*° values for electrodes with the same level of 3DOM carbon oxidation are rather small in comparison to the difference in *E*° for the different levels of oxidation, no direct relationship between oxidation time and initial potential is apparent.

Table 3.6. BET surface area, mesopore surface area, micropore surface area, mesopore volume, micropore volume, and average pore diameter of unoxidized and oxidized 3DOM carbon.

Oxidation time (min)	**BET surface area ($m^2 \cdot g^{-1}$)**	**Mesopore surface area ($m^2 \cdot g^{-1}$)[a]**	**Micropore surface area ($m^2 \cdot g^{-1}$)**	**Mesopore volume ($cm^3 \cdot g^{-1}$)**	**Micropore volume ($cm^3 \cdot g^{-1}$)**	**Average pore diameter (nm)**
0	247	25	192	0.031	0.088	1.8
15	372	50	284	0.084	0.160	3.2
60	467	65	354	0.087	0.198	3.1

[a] Mesopore surface area and mesopore volume are calculated for pore size ranges of 1.9–49, 2.1–60, and 2.1–56 nm for 0, 15, and 60 min of oxidation, respectively. The difference in the total area/volume and the sum of the mesopore and micropore area/volume is due to pores larger than the upper limit of the mesopore range.

Table 3.7. Concentrations of the functional groups on the surface of unoxidized and oxidized 3DOM carbon as determined by acid/base titration.[a]

Oxidation time (min)	**Ketone ($\mathrm{mmol \cdot g^{-1}}$)**	**Phenol ($\mathrm{mmol \cdot g^{-1}}$)**	**Lactone and lactol ($\mathrm{mmol \cdot g^{-1}}$)**	**Carboxylic acid ($\mathrm{mmol \cdot g^{-1}}$)[b]**	**E° (mV)[c]**
0	0.34	0.27	0.0	0.0	285 ± 27
10	0.51	0.35	0.35	0.79	531 ± 30
30	0.75	0.50	0.44	1.60	421 ± 19
60	1.05	0.65	0.91	2.72	642 ± 17

[a] The *E*° values of electrodes prepared with oxidized and unoxidized 3DOM carbon solid contacts and polymeric sensing membranes are also shown.

[b] The titration method cannot distinguish between carboxylic acid and anhydride groups, which may also be present.

[c] The *E*° values are an average of three (60 min of oxidation) or four (0, 10, and 30 min of oxidation) electrodes prepared in an identical manner.

3.3.3.3. Aqueous Layer Test and Long-Term Drift

The formation of an aqueous layer between the ion-selective sensing membrane and solid contact is directly related to the surface chemistry of the solid contact. If such a layer is formed, it can significantly affect the response and detection limit of an SC-ISE, and in the case of conventional SC-ISEs it can lead to complete delamination of the sensing membrane from the solid contact.[360,372] As described above, we tested for the formation of an aqueous layer in electrodes with unoxidized 3DOM carbon as the solid contact. Here, oxidized 3DOM carbon and untemplated carbon-contacted electrodes were examined using the same procedure (Figure 3.12). A very large negative drift was observed for the untemplated carbon-contacted electrode. This is clear evidence for the formation of an aqueous layer between untemplated carbon and the PVC membrane, and it is likely also related to the very poor long-term stability of this system with a potential drift of 1530 μV·h^{-1} over 70 h.

Evidence for the existence of an aqueous layer was also found for the oxidized 3DOM carbon-contacted electrode, even though the overshoot in potential was smaller than for the untemplated carbon. After going through a maximum, the EMF gradually decreased by 11.9 mV until it stabilized at a value 9.4 mV lower than before exposure to the Na$^+$ solution.

The worse performance of the oxidized 3DOM carbon as compared to the unoxidized 3DOM carbon is consistent with the different potential stabilities of the two systems. The average drift for three SC-ISEs with an unoxidized 3DOM carbon solid contact after initial conditioning in K$^+$ solution for 24 h was found to be 11.7 ± 1.0 μV·h^{-1} over 70 h. For three SC-ISEs with an oxidized 3DOM carbon solid contact, drifts of 29 ± 33 μV·h^{-1} were determined. Although the drifts for the oxidized 3DOM carbon constructs are small, they are larger than for the unoxidized 3DOM carbon. The large increase in surface area resulting from the introduction of macropores allows for a much larger interfacial surface area between the solid contact and sensing membrane, leading to a much lower drift compared to the untemplated carbon. However, increasing the surface area further by oxidation of the carbon does not lead to a further increase in stability. The corresponding surface area increase is mostly due to micropores (<2 nm), which are not readily accessible to all membrane components. Also, the oxidation causes a significant increase in the concentration of oxygen-containing functional groups (as shown above), creating a more hydrophilic surface. This allows for the formation of a water layer, decreasing the stability of the electrodes.

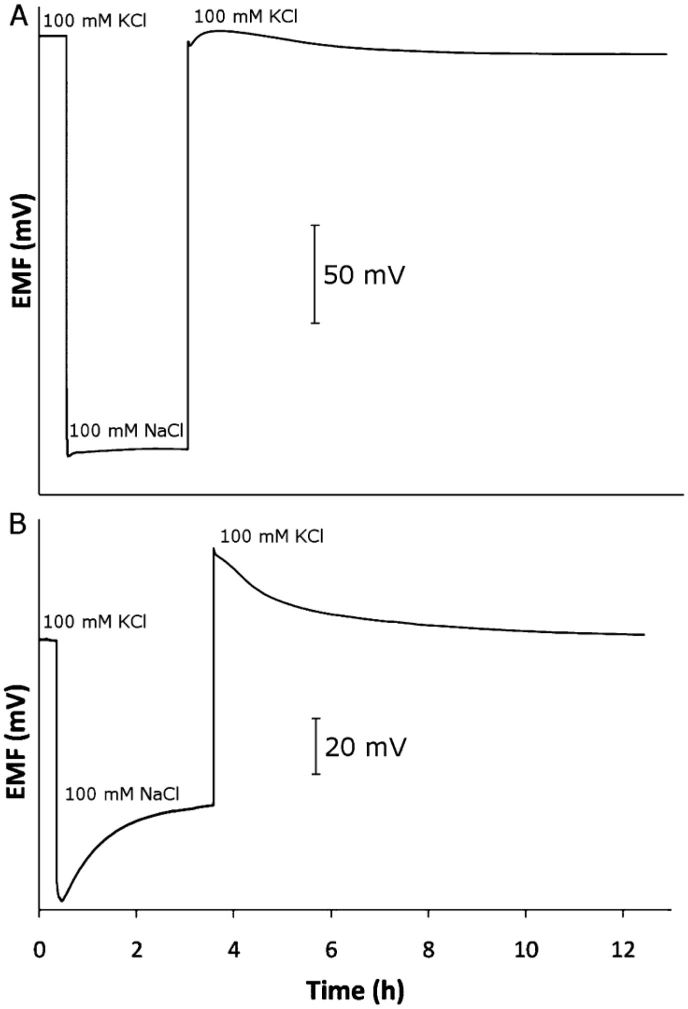

Figure 3.12. Aqueous layer test for (A) oxidized 3DOM carbon and (B) untemplated carbon. At *t* = 0.35 h (for A) or 0.55 h (for B), the 100 mM KCl conditioning solution was replaced by 100 mM NaCl. At *t* = 3.6 h (for A) or 3.0 h (for B), the 100 mM NaCl was replaced by100 mM KCl.

3.3.3.4. Electrochemical Investigation of 3DOM Carbon Solid Contacts

Several electrochemical techniques were used to examine unoxidized 3DOM carbon and oxidized 3DOM carbon solid contacts in order to better understand their effect on potentiometric measurements. First, cyclic voltammetry (CV) was performed on unoxidized 3DOM carbon and 3DOM carbon that had been oxidized for 15 min (Figure 3.13). The measurements were performed without polymeric sensing membranes and using acetonitrile as the solvent (0.1 M KPF_6), which effectively wets both types of carbon. A scan rate of 0.5 $mV{\cdot}s^{-1}$ was used, and the capacitance was calculated from the current values at 0.0 V of the last cycle (see section 3.2.5.3.). The measured capacitance of unoxidized 3DOM carbon was 3.9 $F{\cdot}g^{-1}$, whereas the value for oxidized 3DOM carbon was 62 $F{\cdot}g^{-1}$. The large increase in capacitance after oxidation cannot be explained only by the increase in surface area associated with the oxidation (Table 3.6). Oxidation for 15 min increased the surface area of the 3DOM carbon by about 50%, whereas the apparent capacitance as determined by CV increased by a factor of 16.

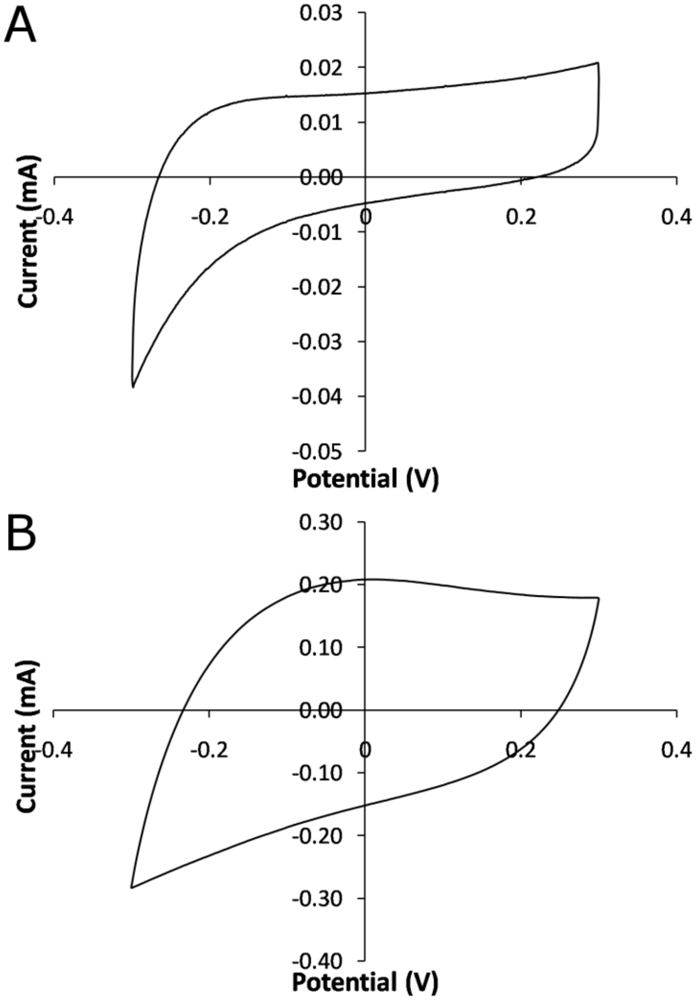

Figure 3.13. Cyclic voltammograms of (A) unoxidized 3DOM carbon and (B) oxidized 3DOM carbon scanned at 0.5 mV·s^{-1}. Each experiment was performed in a non-aqueous electrolyte, and the third cycle is shown for each.

The same trend was also observed when capacitances were determined using chronopotentiometry with unoxidized and oxidized 3DOM carbon (15 min oxidation) in acetonitrile solution at three different currents (1, 0.5, and 0.1 mA, see Table 3.8 and Figure 3.14). For unoxidized carbon, the capacitance increased from 1.92 to 2.25 F·g^{-1} as the current decreased from 1 to 0.1 mA. For oxidized carbon, this effect was even more pronounced. The apparent capacitance increased from 11.0 to 68.4 $F\cdot g^{-1}$ when the current was decreased from 1 to 0.1 mA. As for the cyclic voltammetry, the time scale of the experiment appears to have a large effect on the capacitance, especially for oxidized 3DOM carbon. This suggests that a technique with time resolution, such as electrochemical impedance spectroscopy (EIS),[373,374] is better suited to characterize the capacitance of 3DOM carbon electrodes.

Table 3.8. Apparent capacitance values obtained for unoxidized and oxidized 3DOM carbon (15 min of oxidation) by chronopotentiometry at three different currents.

	Capacitance at		
Sample	**1 mA ($F\cdot g^{-1}$)**	**0.5 mA ($F\cdot g^{-1}$)**	**0.1 mA ($F\cdot g^{-1}$)**
3DOM C	1.92	2.10	2.25
Oxidized 3DOM C	11.0	46.8	68.4

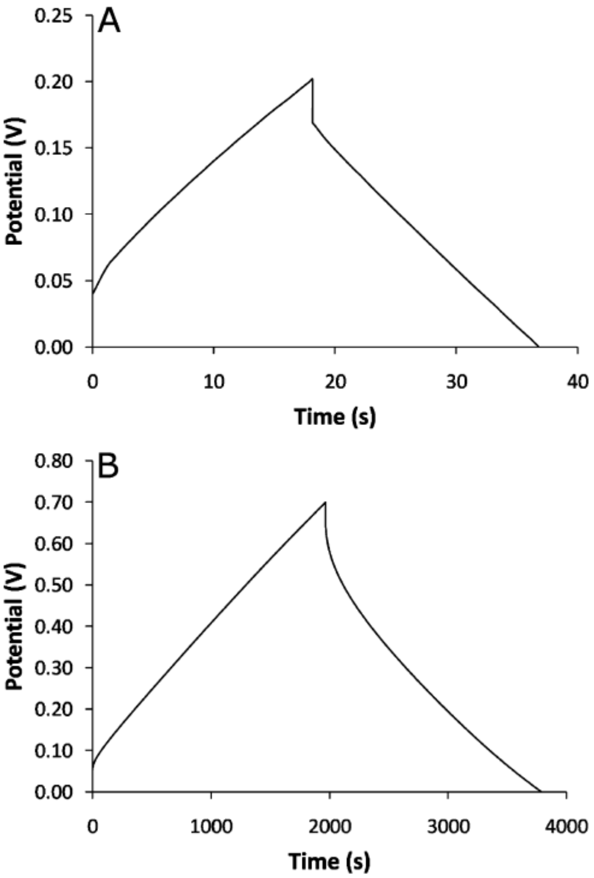

Figure 3.14. Chronopotentiometry data for (A) unoxidized and (B) oxidized 3DOM carbon. A charge and discharge current, *i*, of 0.1 mA was used. The instantaneous drops in potential at the peak maxima coincide with the current reversal. They are a result of the cell resistance, *R*, which adds a contribution of *iR* to the observed potential; the sign of this contribution depends on the direction of the current.

Therefore, EIS was performed on unoxidized 3DOM carbon (again in acetonitrile solution). The complex plane plot and fitted equivalent circuit are shown in Figure 3.15A, while the values of the fit are shown in Table 3.9. In the fit for this construct, the series resistance R1 arises from the acetonitrile solution and the Luggin capillary reference electrode. The observation of a parallel combination of a capacitor and resistor (C1/R2) is expected for an electrode surface exhibiting interfacial capacitance (C1) and interfacial charge transfer resistance (R2) and is associated in this case with the surface of the 3DOM carbon. Since the series combination of R1 and C1/R2 did not provide a good fit, an additional parallel combination of a resistor (R4) and a constant phase element (CPE1) was used for fitting. CPEs with a phase value of 1.0 behave as capacitors, whereas CPEs with a phase value of 0.5 behave as Warburg impedances.[374] In this case, the fitted phase value of 0.37 suggests that the CPE1/R4 element appears to be associated with Warburg diffusion and that R4 represents the resistance of the electrolyte phase trapped within the 3DOM carbon. Note that data for $\omega > 1500$ Hz were not used for this fit since they are part of a semicircle centered on the negative side of the *x*-axis and can be readily recognized as affected by a high-frequency instrumental artifact.[375]

If the mass of the 3DOM carbon monolith used for the EIS shown in Figure 3.15A is taken into account, a specific capacitance of 1.77 $F \cdot g^{-1}$ is obtained from the fitted value of C1. This value is reasonably close to the one obtained for unoxidized 3DOM C using CV (3.9 $F \cdot g^{-1}$) and chronopotentiometry at 1 mA (1.92 $F \cdot g^{-1}$). However, since EIS takes advantage of the frequency dependence to distinguish between the C1/R2 and CPE1/R4 elements, the value of 1.77 $F \cdot g^{-1}$ for nonoxidized 3DOM carbon appears to be most trustworthy.

The larger values for the apparent capacity obtained from CV or chronopotentiometry, in particular when investigated in long experiments (i.e., for slow scan rates in CV and for low currents in chronopotentiometry), and the much larger apparent capacitances for oxidized 3DOM carbon can be explained by the occurrence of redox reactions. In the case of CV, they increase the total current beyond the double layer charging current. In the case of chronopotentiometry, they reduce the fraction of the total current available to charge the double layer. While the chronopotentiometry data look symmetrical with respect to charging and discharging, the CVs clearly lack symmetry with respect to the direction of the scan (see Figure 3.13). This indicates that the redox reactions in question are irreversible on the CV time scale. The much higher apparent capacitance in the case of the oxidized 3DOM carbon despite the only marginally increased surface area suggests that the rate of these redox reactions is directly affected by the surface functional groups. This may be explained by redox reactions that involve these functional groups themselves. Alternatively, these functional groups may play a catalytic role. Indeed, a strong dependency of the rate constants of redox reactions on the surface chemistry of carbon electrodes is well-known.[376]

3.3.3.5. EIS Investigation of PVC Membrane-Coated Electrode Constructs

Four membrane-coated electrode constructs were also investigated using EIS: a piece of Ni mesh covered with a PVC sensing membrane in order to characterize electrodes without a carbon solid contact and three PVC sensing membrane-covered electrodes with different carbon solid contacts (3DOM carbon, 3DOM carbon oxidized for 15 min, and untemplated carbon) in order to examine the effects of different solid contacts. For all PVC membrane-coated constructs, an aqueous electrolyte containing K^+ was used. The complex plane impedance plot for each system (Figure 3.15B–E) was fitted to an equivalent circuit (insets of Figure 3.15, fit values in Table 3.9).

All four constructs are more similar to each other than they are to the system without a PVC membrane, as it was described above. In each case, a negative R1 value is observed. Similarly as for the membrane-free constructs, this is an instrumental high-frequency artifact. For all four electrodes, the fits provide an R2 value of a few hundred kilo-ohms, which is a value very typical for bulk resistances of plasticized PVC membranes. Consequently, the C1 element represents the geometrical capacity of the sensing membranes. Similar semicircles arising from a parallel combination of C1/R2 have been observed in numerous impedance studies of ISEs.[370,373] For all four PVC membrane-coated electrode constructs, the CPE1/R4 element (or alternatively the CPE1 element, which is equivalent with a CPE/*R* element with a very large resistance *R*) corresponds to the CPE1/R4 element in the 3DOM carbon case. Here, this term is associated with diffusion through the bulk of the PVC membrane that is the top layer of the four electrode constructs instead of diffusion through the organic electrolyte, as for the 3DOM carbon constructs without polymeric sensing membrane. Therefore, R4 has a much larger value than in the case of the 3DOM carbon in acetonitrile electrolyte solution (i.e., without polymeric membrane coating). Whereas for the Ni/ PVC electrode and the construct with the untemplated carbon the phase values for the CPE differ more significantly from 0.5, the more important cases of the constructs with nonoxidized and oxidized 3DOM carbon are characterized by phase values very close to 0.5, as expected for a pure Warburg impedance.

In the cases where the solid contacts are 3DOM carbon (oxidized or not; Figure 3.15, parts D and C, respectively), an additional element (C2/R3) is present. The fitted value of the C2 is very similar to the fitted values of C1 for the geometrical capacitance of the polymeric sensing membrane located on top of the 3DOM carbon constructs, and indeed many orders of magnitude smaller than the double layer capacitance of the 3DOM carbon surface, as observed in Figure 3.15A. We conclude that C2, and therefore R3, are both associated with the plasticized polymeric membrane material within the pores of the 3DOM carbon. The lower resistance R3 for the oxidized 3DOM carbon as compared to the unoxidized 3DOM carbon is consistent with its larger available pore volume (see Table 3.6). The overlap of the two semicircles for C1/R2 and C2/R3 due to the similar values of C1 and C2 as well as R2 and R3 explain the semi-ellipse feature in the impedance plots in Figure 3.15, parts C and D. This particular shape is distinctly different from the nearly ideal semicircles observed for Figure 3.15, parts B and E, and appears to be characteristic for the electrodes with 3DOM carbon (whether unoxidized or oxidized) solid contacts. Its observation is a further confirmation for the penetration of the polymeric sensing membrane material into the porous 3DOM carbon.

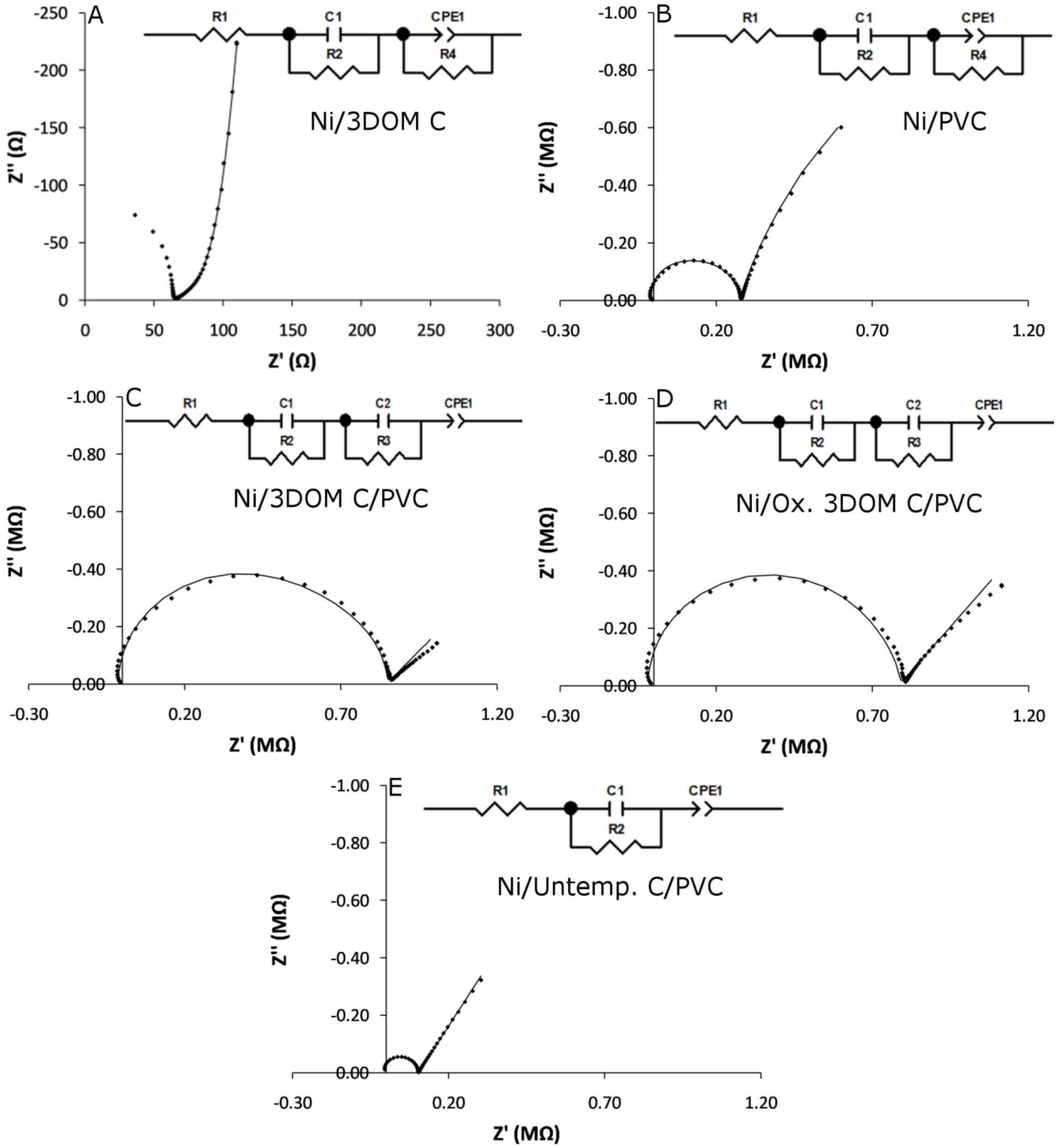

Figure 3.15. Complex plane impedance plots and fits of (A) Ni mesh/3DOM carbon in a nonaqueous electrolyte, (B) Ni mesh/PVC membrane, (C) Ni mesh/3DOM C/PVC membrane, (D) Ni mesh/oxidized 3DOM C/PVC membrane (15 min of oxidation time), and(E) Ni mesh/untemplated carbon/PVC membrane. Data for panels B–E were collected with aqueous electrolyte (0.1 M KCl). Proposed equivalent circuits are shown as insets in each panel. Actual data are shown as ♦, whereas solid lines represent data fits. The fitted values for the elements of the equivalent circuits are listed in Table 3.9. Note the Ω scale of panel A and the MΩ scale of panels B–E.

Table 3.9. Fitting values for the impedance data shown in Figure 3.15.[a]

Circuit element	**(A) Ni/3DOM C**	**(B) Ni/PVC**	**(C) Ni/3DOM C/ PVC**	**(D) Ni/ox 3DOM C/ PVC**[b]	**(E) Ni/untempl C/ PVC**[c]
R1 (Ω)	64	-1.1×10^{4}	-1.3×10^{4}	-1.8×10^{4}	-7.5×10^{3}
C1 (F)[d]	7.6×10^{-3}	7.7×10^{-11}	5.7×10^{-11}	3.9×10^{-11}	4.8×10^{-11}
R2 (Ω)	1.5×10^{4}	2.8×10^{5}	6.7×10^{5}	7.6×10^{5}	1.1×10^{5}
C2 (F)[d]			8.1×10^{-11}	3.6×10^{-9}	
R3 (Ω)			1.8×10^{5}	4.6×10^{4}	
CPE1-T	1.6×10^{-2}	2.0×10^{-6}	6.1×10^{-6}	2.7×10^{-6}	3.5×10^{-6}
CPE1-P	0.37	0.81	0.53	0.57	0.66
R4 (Ω)	1.1×10^{2}	3.3×10^{6}			

[a] Labels A–E correspond to Figure 3.15.

[b] 3DOM carbon oxidized for 15 min.

[c] Untemplated carbon.

[d] C1 and C2 were also fit as CPEs. The CPE phase values indicated the presence of nearly perfect capacitors, so capacitors were used instead.

3.4. Conclusion

This work presents a new approach to fabricate SC-ISEs by using 3DOM carbon. Our results show that the 3DOM carbon layer containing the ionophore-doped polymeric phase is capable of both ionic and electronic charge transfer. The 3DOM carbon-contacted electrode provided a good Nernstian response to potassium, with a detection limit of $10^{-6.2}$ M towards K^{+} before optimization, which is similar as for typical SC-ISEs with conducting polymer contacts. Importantly, the 3DOM carbon-contacted electrode was found to exhibit a greatly improved long-term potential stability, and it had good resistance to the interferences from O_2 and light. Interestingly, there was no clear evidence for the formation of an aqueous layer, which is probably the result of the rather hydrophobic character of the surface of 3DOM carbon.

An improved detection limit of 3DOM carbon-contacted ISEs for K^+ was obtained with conditioning at low K^+ concentration. The resulting detection limit is comparable to that of other K^+ selective SC-ISEs operated under optimized conditions. This work also presents the first application of 3DOM carbon-contacted ISEs for the trace-level detection of Ag^+. With optimizations of the polymer content, the molar ratio of ionophore and ionic sites, and the concentrations of the conditioning and starting solutions, the detection limit for Ag^+ could be lowered into the subnanomolar concentration range. The successful detection of Ag^+ at these low concentrations and the excellent stability and resistance to interferences reported previously make 3DOM carbon-contacted ISEs interesting for trace-level measurements in real life samples.

The structural and electrochemical properties of K^+ ISEs with 3DOM carbon, oxidized 3DOM carbon, and untemplated carbon as solid contacts were examined to explain the excellent performance of these SC-ISEs and, in particular, the very low long-term drift of the potentiometric responses. Cryo-SEM, elemental analysis, and EIS confirmed that the components of the sensing membrane enter the macropores of the 3DOM carbon, creating a large contact area between the carbon and the membrane. This large interfacial area, along with the high capacitance of the 3DOM carbon solid contacts as determined by CV, chronopotentiometry, and EIS is essential for the excellent long-term stability. The untemplated carbon, which differs from the unoxidized 3DOM carbon only by its lack of pores, has a much lower surface area and smaller capacitance than either unoxidized or oxidized 3DOM carbon. Electrodes prepared with untemplated carbon show poor initial potential reproducibility and long-term stability. Clearly, the pore structure plays an essential role in determining the properties of the system. However, the surface chemistry of the 3DOM carbon cannot be neglected. The oxidized 3DOM carbon was determined to have a much higher concentration of surface functional groups than the unoxidized 3DOM carbon. Although electrodes with oxidized 3DOM carbon as the solid contact had still high long-term stabilities—albeit not as good as SC-ISEs with unoxidized 3DOM carbon contacts—they fared less favorably in the aqueous layer test.

This work also permits a comparison of methods for the characterization of SC-ISEs. There is still little consensus on how to do this best,[377] which can be partially explained by the diversity of their applications. Whereas a quick response and reproducibility of $E°$ are important for single-use devices, low drift is essential for long-term monitoring. In view of the latter, constant-current charge-discharge experiments offer an attractive approach to quantify the stability of SC-ISEs because they are fast and are hardly affected by temperature changes and drifts in liquid junction potentials at the reference electrode. However, this work demonstrates that such experiments can be biased by irreversible redox reactions, which may not be representative of the electrode behavior in long-term potentiometric measurements but are an artifact of the large applied currents. Consequently, charge-discharge experiments need to be interpreted with care.

Chapter Four

Receptor-Based Detection of 2,4-Dinitrotoluene Using Modified Three-Dimensionally Ordered Macroporous Carbon Electrodes

Reproduced in part with permission from reference 378. Copyright American Chemical Society 2012.

4.1. Motivation

The detection of explosives, including 2,4,6-trinitrotoluene (TNT), is an important analytical problem of relevance for the prevention of terrorism and for the detection of military explosives (including leftover landmines) and environmental hazards from improperly disposed explosives.[379] Rather than attempting to detect TNT directly, researchers often focus on detecting 2,4-dinitrotoluene (DNT).[380-382] DNT, which is a common impurity in TNT-based explosives,[383] exhibits a higher volatility than TNT, allowing for considerably more sensitive detection. In fact, DNT is the component of TNT-based explosives that canines are able to detect with very good sensitivity.[383,384]

Many methods of DNT detection have been reported, including photoluminescence and fluorescence quenching,[385,386] detection of reduction or degradation products,[387-389] vapor adsorption on a modified microcantilever,[390] electronic noses and sniffers,[381,391] electrochemical impedance detection,[392] and detection by combining capillary electrophoresis and electrochemical detection with a porous-carbon-modified electrode.[393] For the purpose of miniaturization, electrochemical detectors are attractive for sensing explosives.[392,394-397] Electrode miniaturization offers many benefits, including reduced cost, which enhances the feasibility of creating sensor networks, and greater portability. Moreover, the adaptation of an electrochemical sensor to detect explosive compounds is rather straightforward, as their structures make them inherently redox active. A common theme in most published electrochemical sensors for DNT, however, is that their selectivity is determined largely by the redox potential of the analyte. The addition of a supramolecular receptor that specifically binds the analyte has the potential for greatly improving both the selectivity and sensitivity of detection.[299] In fact, molecular recognition schemes have previously been developed for the electrochemical detection of the related compound TNT.[312,398]

In this work, a receptor-modified, three-dimensionally ordered macroporous (3DOM) carbon electrode was used to detect DNT electrochemically. The use of porous electrodes, including carbon electrodes, for electroanalytical applications has recently been reviewed.[223,399] 3DOM carbon, a conductive material composed of glassy carbon walls that surround an ordered array of interconnected pores (Figure 4.1), is a particularly attractive electrode material due to its highly accessible and relatively large surface.[244,400] For sensing applications, 3DOM carbon has previously been used as an electrode for solid-state ion-selective and reference electrodes, and extremely low detection limits and very small EMF drifts were achieved.[262,317,318,401] As prepared, the walls of 3DOM carbon do not contain many functional groups,[318] and further functionalization is required to attach receptor molecules. The functionalization scheme used to modify the walls of the pores in 3DOM carbon is shown in Figure 4.1. After functionalization with nitrophenyl groups by diazonium reduction, the nitro groups are reduced to amino groups, which provide an aminophenyl functionalized surface that can be chemically modified by many different methods.[402] Here, 1,6-diisocyanatohexane was reacted with the aminophenyl groups, followed by reaction with 1,6-hexanediamine to give a receptor with two urea groups and a terminal aliphatic amine to interact with DNT.

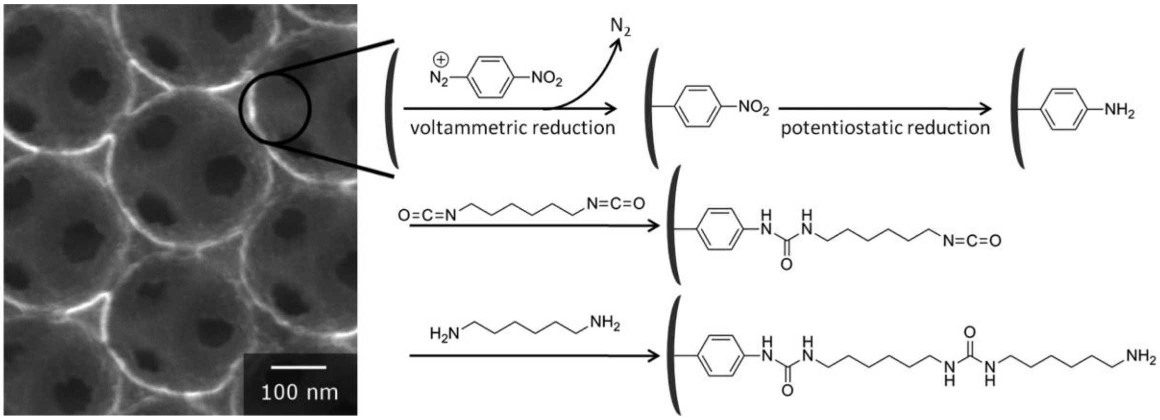

Figure 4.1. Scheme for functionalization of 3DOM carbon (left) to produce receptor-modified electrodes through electrochemical and chemical modification steps.

This receptor molecule was chosen on the basis of previous work, which conclusively showed that in DMSO solutions, the methyl group of DNT is deprotonated by bases such as amines.[403] In the case of the receptor that we designed herein, we expected that DNT would be deprotonated by the terminal amino group of the receptor. The resulting deprotonated DNT would exhibit partial anionic character at each nitro group due to resonance. Because urea moieties are well-known to be good hydrogen bond donors,[402] they are expected to interact rather strongly with the electron-rich nitro groups. By stabilizing the anionic nature of the nitro groups of deprotonated DNT, binding of DNT with the developed receptor would likely lower the pK_a of DNT and therefore further stabilize the DNT:receptor complex. The anticipated geometry of the DNT:receptor interaction is shown in Figure 4.2.

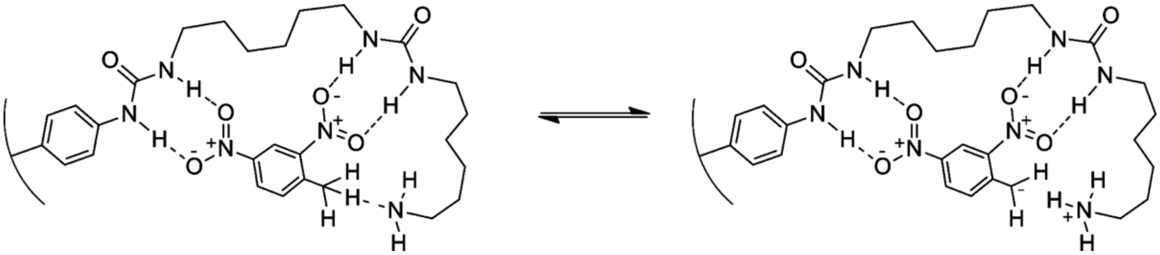

Figure 4.2. Anticipated interaction between DNT and the receptor on the surface of the 3DOM carbon.

In this work, we describe the synthesis and characterization of the receptor-modified 3DOM carbon electrodes and evaluate their performance as DNT sensors in cyclic voltammetry (CV) and square wave voltammetry (SWV) experiments. By SWV, a detection limit of 10 μM was established.

4.2. Experimental

4.2.1. Materials

All reagents were of the highest commercially available purity. Resorcinol, 4-nitrobenzenediazonium tetrafluoroborate, 1,6- diisocyanatohexane, 1,6-hexanediamine, boron trichloride (1.0 M in heptane), t-butyl lithium (1.7 M in pentane), 2,4-dinitrotoluene, and benzotrifluoride (α,α,α-trifluorotoluene) were from Sigma-Aldrich (St. Louis, MO), tetrabutylammonium chloride and tetrabutylammonium tetrafluoroborate were from Fluka (Milwaukee, WI), formaldehyde (37% in H_2O) was from Fisher Scientific (Pittsburgh, PA), 1-bromo- 3,5-bis(trifluoromethyl)benzene was from SynQuest Laboratories (Alachua, FL), unplasticized PVC sheets were from

Goodfellow (Oakdale, PA), and Ni mesh was a gift from Dexmet (Branford, CT). All chemicals were used as received.

4.2.2. Nitrophenyl Functionalization of 3DOM Carbon Electrodes

3DOM carbon was synthesized and attached to nickel mesh (as a current collector) as described in Chapter 3. Nitrophenyl functional groups on the walls of the pores in 3DOM carbon were produced electrochemically by an adapted version of a previously published method.[187,188] Functionalization of the porous electrode requires a high concentration of the diazonium salt because diffusion through the pores is not fast enough to allow for replenishment of the solution in the pores from the bulk solution. A nonaqueous reference electrode and a platinum wire counter electrode were placed in a 25 mL round-bottom flask. Approximately 2 mL of the functionalization solution (an acetonitrile solution containing 0.1 M tetrabutylammonium tetrafluoroborate electrolyte and saturated with 4-nitrobenzenediazonium tetrafluoroborate) was added. After purging the solution with argon for 10 min, the 3DOM carbon electrode was submerged in the solution. Bubbles immediately emerged from the carbon electrode, indicating wetting of the porous carbon by the electrolyte solution. The functionalization was carried out using cyclic voltammetry, with a window of +0.8 to −1.7 V vs Ag/10 mM $AgNO_3$ (CH_3CN) and a sweep rate of 10 $mV\cdot s^{-1}$ for 2−4 cycles (until consecutive cycles overlapped well). After functionalization, the electrode was thoroughly cleaned by soaking in fresh acetonitrile several times.

4.2.3. Aminophenyl Functionalization of 3DOM Carbon Electrodes

The nitrophenyl functional groups on the walls of the 3DOM carbon were electrochemically reduced to aminophenyl functional groups. The modified electrode was placed in an aqueous 0.1 M phosphate buffer ($NaH_2PO_4 \cdot H_2O/Na_2HPO_4 \cdot 7H_2O$) solution (10 v/v % ethanol was added to facilitate wetting, pH 7.1) with a double-junction Ag/AgCl reference electrode and a platinum wire counter electrode. A constant potential of −1.4 V versus the reference electrode was applied for 2 h. The electrodes were then cleaned by soaking in fresh water/ethanol solution several times.

4.2.4. Reaction with 1,6-Diisocyanatohexane

The aminophenyl-modified electrodes were reacted with 1,6-diisocyanatohexane, forming a urea group between an isocyanate functionality and the $-NH_2$ of the aminophenyl on the surface of the carbon electrode. This process leaves a free isocyanate group on the end of the receptor. An aminophenyl functionalized electrode was placed in a small flask. Approximately 4 mL neat 1,6-diisocyanatohexane was added to the flask, completely covering the carbon component of the electrode. The flask was attached to a water-cooled condenser and heated in an oil bath at 120 °C for 24 h. The electrode was then removed from the flask and cleaned by soaking in fresh toluene several times.

4.2.5. Reaction with 1,6-Hexanediamine

A second urea group and a terminal amino group were formed by reacting the isocyanate-functionalized electrodes with 1,6-hexanediamine, forming the complete receptor. An isocyanate-functionalized electrode was placed in a small flask. Approximately 4 mL of a 10 w/w% solution of 1,6- hexanediamine in toluene was added. The flask was attached to a water-cooled condenser and heated in an oil bath at 120 °C for 24 h. The electrode was then removed from the flask and cleaned by soaking in fresh toluene several times.

4.2.6. Electrode Encasement

Before use, fully modified electrodes were encased in unplasticized poly(vinyl chloride) (PVC) to provide mechanical stability and electrical insulation. PVC sheets sealed with commercial PVC adhesive were used to encase the entire electrode, except for the functionalized 3DOM carbon and a small portion of the Ni mesh on the opposite end of the electrode construct (to allow for electrical contact).

4.2.7. Synthesis of NBu_4BArF_{24}

After optimization, a solvent/electrolyte combination of benzotrifluoride with tetrabutylammonium tetrakis[3,5-bis(trifluoromethyl)phenyl]borate (NBu_4BArF_{24}) was selected (Figure 4.3). Benzotrifluoride was chosen because it does not interact with the receptor on the carbon surface, which would prevent detection of DNT. It also does not dissolve or soften the electrode encasement material. NBu_4BArF_{24} is soluble to 100 mM in benzotrifluoride and sufficiently lowers the resistance to allow electrochemical experiments to be carried out.

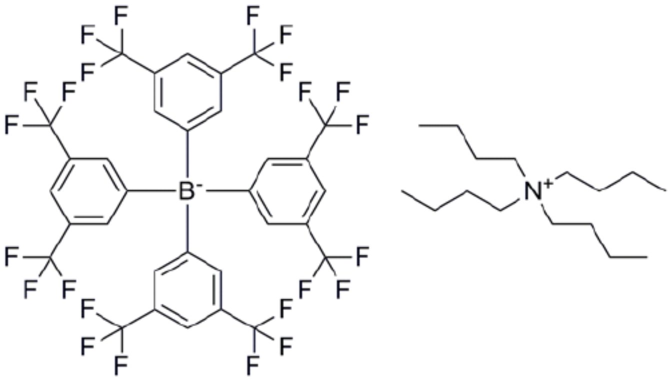

Figure 4.3. Structure of the electrolyte tetrabutylammonium tetrakis[3,5-bis(trifluoromethyl)phenyl]borate (NBu_4BArF_{24}).

Sodium tetrakis[3,5-bis(trifluoromethyl)phenyl]borate was prepared as follows by adaptation of a previously described procedure for the synthesis of sodium tetrakis[3,5-bis(perfluorohexyl)phenyl]borate.[404] All synthetic steps were carried out in an argon atmosphere, unless otherwise noted. A 1.7 M solution of *t*-butyl lithium (76 mL, 130 mmol, 9.2 equiv) was added over 30 min by addition funnel to a stirred solution of 1-bromo-3,5-bis(trifluoromethyl)benzene (10 mL, 56 mmol, 4.7 equiv) chilled to −76 °C. After the solution was allowed to stir for 30 min, a 1.0 M BCl_3 solution (12 mL, 12 mmol, 1 equiv) was added dropwise by syringe over 10 min. Upon complete addition of the BCl_3 solution, the reaction mixture was warmed slowly to room temperature and stirred vigorously for an additional 2 h. The crude mixture was then slowly poured into 100 mL of NaCl-saturated water (the remaining steps are not air-sensitive) and vigorously mixed. This mixture was then extracted with diethyl ether (3 × 100 mL). The organic layers were combined, dried with anhydrous $MgSO_4$, and rotary evaporated to yield a pale yellow oil. This oil was dried at 100 °C under vacuum to produce a tan-yellow solid. The product was recrystallized 3 times from benzotrifluoride by addition of hexane to produce high purity $NaBArF_{24}$ as a fine white powder (40% yield). ^1H NMR (300 MHz, acetone-d_6, δ): 7.69 (s, *p*-ArH, 4H), 7.81 (s, *o*-ArH, 8H). These NMR shifts are in good agreement with previously published results for this compound.[405-407]

NBu_4BArF_{24} was synthesized by metathesis from tetrabutylammonium chloride and sodium tetrakis[3,5-bis(trifluoromethyl)phenyl]borate: 8.0 g of sodium tetrakis[3,5-bis(trifluoromethyl)phenyl]borate and 1.0 g of tetrabutylammonium chloride were added to a separatory funnel containing 300 mL water and 300 mL benzotrifluoride. The mixture was shaken until all of the salt dissolved. The organic layer was collected, washed three times with 300 mL water, dried with $MgSO_4$, and filtered. The solvent was removed by rotary evaporation and further drying under vacuum at 75 °C for 48 h, yielding NBu_4BArF_{24} as a pale yellow, wax-like material in quantitative yield. ^1H NMR (300 MHz, acetone-d_6, δ): 1.00 (t, J_{HH} = 7.2 Hz, $-CH_3$, 12H), 1.46 (m,$-CH_2CH_3$, 8H), 1.86 (m, NCH_2CH_2-, 8H), 3.48 (m, NCH_2-, 8H), 7.69 (s, *p*-ArH, 4H), 7.80 (s, *o*-ArH, 8H).

4.2.8. Characterization

The nitrophenyl and aminophenyl functionalized 3DOM carbon samples were characterized by X-ray photoelectron spectroscopy (XPS). After removal from the Ni mesh, the carbon samples were mounted on the sample stage using conductive carbon sticky tape. XPS measurements were carried out on a Surface Science SSX-100 instrument with an Al anode (Kα X-rays at 1486.66 eV) operated at 10 kV and 20 mA. Measurements were performed at room temperature, with a pressure below 1×10^{-8} Torr in the analysis chamber. FTIR spectra for all functionalized 3DOM carbon samples were obtained using KBr pellets in a Nicolet Magna-IR 760 spectrometer.

4.2.9. Electrochemical Measurements

All cyclic voltammetry measurements were performed at room temperature with a CHI600C Potentiostat (CH Instruments, Austin, TX) while square wave voltammetry experiments were performed with a Cypress Systems 1090 Potentiostat (Cypress Systems, Lawrence, KS). All electrochemical experiments utilized a three-electrode setup with a 3DOM carbon electrode as the working electrode, a Ag/10 mM $AgNO_3$ acetonitrile reference electrode (CH Instruments) and a 0.25 mm Pt wire coil (99.998%, Alfa Aesar, Ward Hill, MA) as the auxiliary electrode. Each sample solution contained 100 mM NBu_4BArF_{24} in benzotrifluoride; DNT was introduced to the electrolyte solution by addition of stock solutions. Each sample was thoroughly purged of oxygen by bubbling high-purity argon for 20 min prior to each measurement. An argon atmosphere was maintained over the solution during measurements. Scan rates and window sizes for each experiment are indicated below. For CV experiments, multiple cycles were performed, but only cycle 2 is shown for clarity. Electrodes were evacuated using a vacuum pump for at least one hour between uses to allow for better wetting with the solution for the next experiment. SWV experiments were performed as usual, i.e., the electrode was kept at an initial potential followed by a decrease of the applied potential by the SW amplitude (often referred to as the forward pulse), and then to the original potential minus the SW amplitude (often referred to as the reverse pulse). The applied potential for the forward and reverse pulse was then decreased by 5 mV for each subsequent cycle until the desired end potential was reached. Each potential was kept constant for half of the time period, referred to below as pulse length. The SW voltammogram was obtained by plotting the differences between the currents at the end of each forward pulse and the following reverse pulse.

4.3. Results and Discussion

4.3.1. 3DOM Carbon Electrode Functionalization

3DOM carbon electrodes were first electrochemically functionalized with nitrophenyl groups by voltammetric reduction of 4-nitrobenzenediazonium (Figure 4.4). In the first cycle, a large, irreversible peak at −0.5 V was observed, and is attributed to the reduction of 4-nitrobenzenediazonium to its aromatic radical,[187,188] which then bonds with the surface of the carbon pore walls. In the subsequent voltammetric cycles, the peak decreased until it was no longer present in cycle 4, indicating maximum coverage of the 3DOM carbon surface with nitrophenyl groups. The number of cycles required to complete the reaction depended on the surface area of the 3DOM carbon monolith.

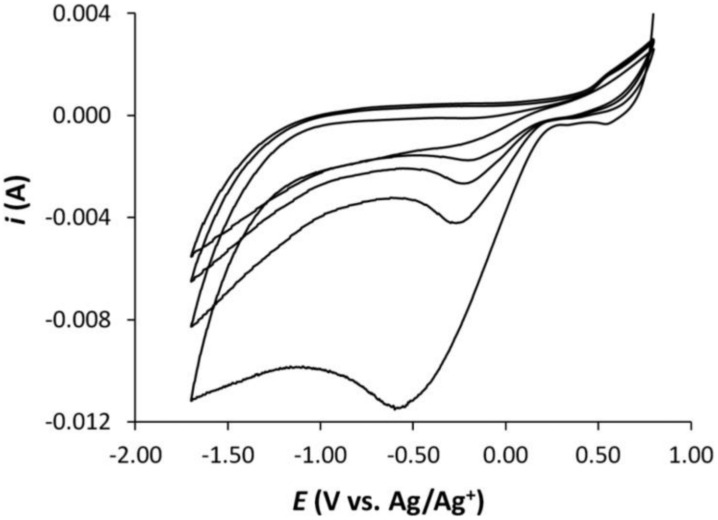

Figure 4.4. Voltammetric functionalization of a 3DOM carbon electrode with a saturated acetonitrile solution of 4-nitrobenzenediazonium tetrafluoroborate (with 0.1 M tetrabutylammonium tetrafluoroborate as the electrolyte), producing nitrophenyl functionalization on the pore walls of the carbon. A scan window of +0.8 to −1.7 V and a scan rate of 10 $mV·s^{-1}$ were used.

The nitro groups on the nitrophenyl modified electrodes were then potentiostatically reduced at −1.4 V in an aqueous phosphate buffer solution. XPS was carried out on reduced and nonreduced samples to verify the reduction of nitro groups to amino groups (Figure 4.5). The bonding environment of nitrogen atoms can be determined by examining the N_{1s} region. Nitrogen atoms in nitro groups produce a peak at 406 eV whereas nitrogen atoms in amino groups produce a peak at 400 eV.[188] The XPS spectrum of nitrophenyl functionalized carbon exhibited peaks at both of these positions (Figure 4.5A). The peak at 406 eV indicates that the walls of the 3DOM carbon were successfully modified with nitrophenyl groups. The additional peak at 400 eV after grafting of nitrophenyl groups has been observed previously.[189,191,212,408-410] Although it suggests the presence of reduced nitrophenyl groups on the surface of the carbon, the peak likely indicates that azo groups were present on the functionalized surface,[408,409] possibly as part of a multilayer film.[410,411]

After potentiostatic reduction of the nitrophenyl modified electrode in an aqueous buffer, only one peak at 400 eV was observed in the XPS spectrum (Figure 4.5B), consistent with the presence of aminophenyl functional groups.[189,408,412]

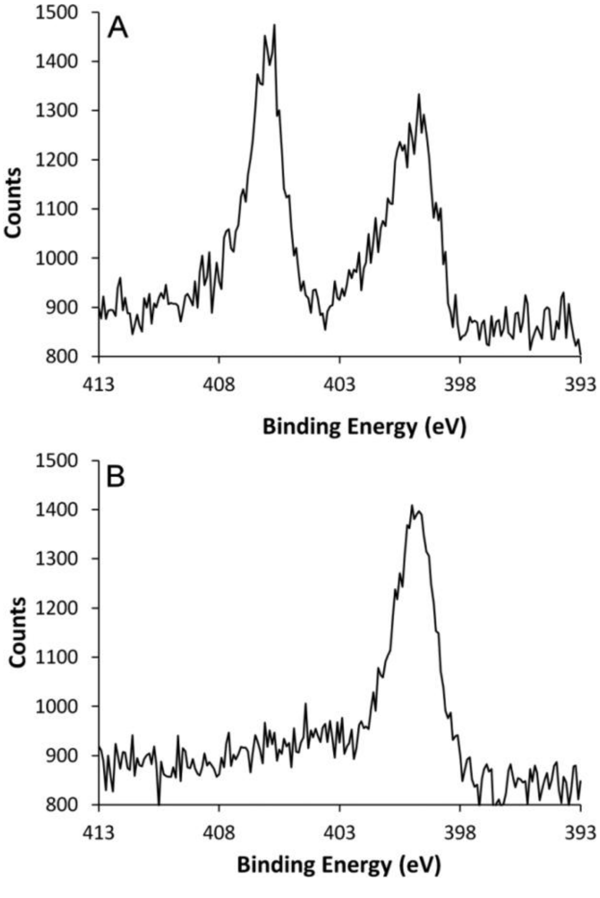

Figure 4.5. XPS spectra of the N_{1s} region of (A) nitrophenyl and (B) aminophenyl functionalized carbon.

After additional chemical functionalization to complete the synthesis of the receptor, FTIR spectroscopy was performed to confirm the presence of the desired functional groups (Figure 4.6). A low concentration of sample in the KBr pellets was required, as carbon absorbs strongly in the infrared.[413] However, the concentration was sufficient to achieve spectra with peaks characteristic of the functional groups attached to the surface of the 3DOM carbon walls. A sample of unfunctionalized 3DOM carbon was also characterized for comparison. The large peak at ~3400 cm^{-1} in each spectrum is due to water adsorbed on the surface of the carbon. In the unfunctionalized sample (Figure 4.6A), the peak at 1575 cm^{-1} is assigned to the skeletal structure of the 3DOM carbon.[414,415] The peaks at 1200 cm^{-1} and 1135 cm^{-1} result from C−O stretching in the oxygen-containing functional groups that exist on the as-made carbon.[318,416,417]

After voltammetric functionalization with nitrophenyl groups and potentiostatic reduction to aminophenyl groups, new peaks appear in the FTIR spectrum (Figure 4.6B). The peak at 1514 cm^{-1} is due to the aromatic C−C stretch of the aminophenyl group.[418] The expected amine N−H stretch at ~3400 cm^{-1} overlaps with the water peak. However, the NH_2 deformation peak at 1597 cm^{-1} is present.[418,419]

Reaction of the aminophenyl functionalized carbon with 1,6-diisocyanatohexane forms a urea group between the amine and an isocyanate group. The attached functionality also contains an aliphatic chain and a terminal isocyanate group. As with the aminophenyl functionalized sample, the FTIR spectrum of diisocyanate functionalized 3DOM carbon (Figure 4.6C) exhibits an aromatic C−C stretch at 1514 cm^{-1}. The aliphatic portion of the functionality is confirmed by the C−H stretching peaks at 2920 and 2850 cm^{-1}. The C=O stretch of the urea group appears at 1668 cm^{-1}, and the NH_2 deformation peak of the urea group is at 1615 cm^{-1}.[418] It is conceivable that some 1,6-diisocyanatohexane molecules do not react to give an attached molecule with the linear structure shown in Panel C of Figure 4.6 but instead form a bridge between two aminophenyl groups.

The further reaction of the diisocyanate functionalized 3DOM carbon with 1,6-hexanediamine forms another urea group with the remaining isocyanate group, adding another aliphatic chain, and leaving a free primary amine. As expected, the FTIR spectrum for the diamine functionalized sample (Figure 4.6D) contains the aromatic C−C stretch at 1514 cm^{-1}, C−H stretches from the aliphatic chains at 2920 and 2850 cm^{-1}, the C=O stretch of the urea group at 1668 cm^{-1}, and the NH deformation peak of the urea group at 1615 cm^{-1}.[418] No peaks for the free primary amine are visible. The peak at ~3400 cm^{-1} is overlapped by the adsorbed water peak.

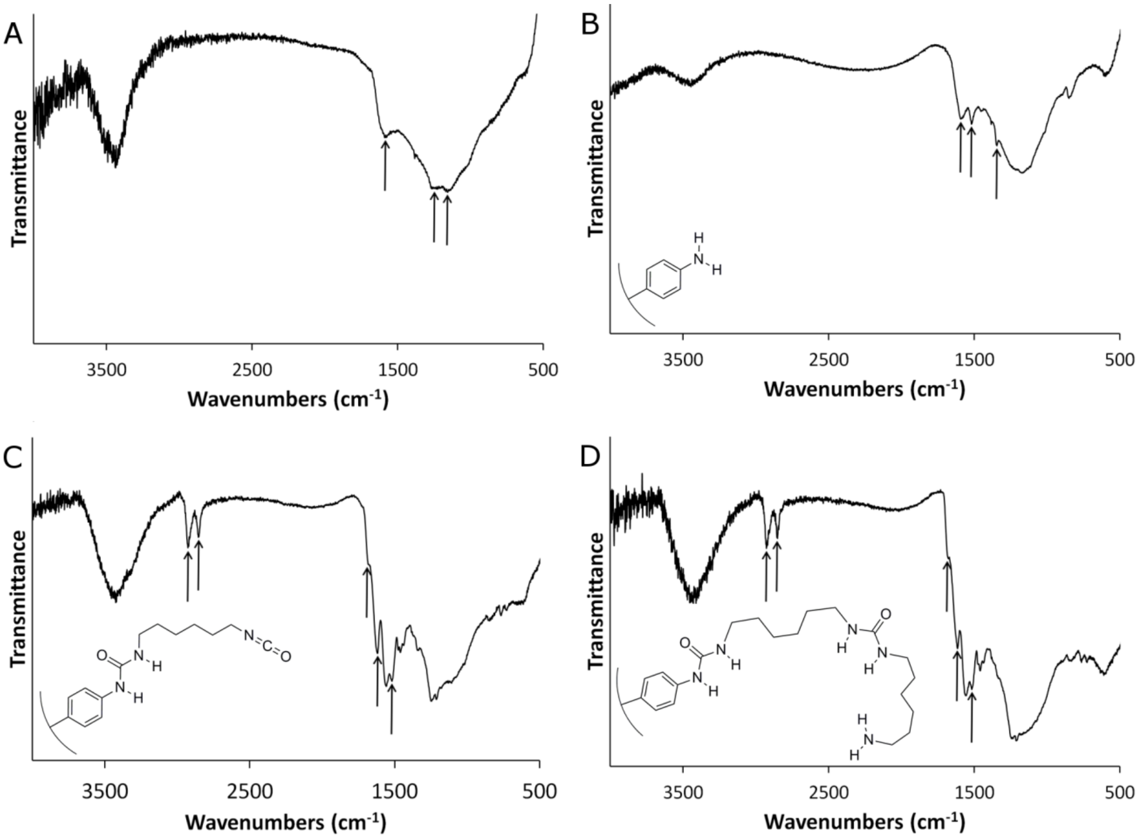

Figure 4.6. FTIR spectra of (A) unfunctionalized 3DOM carbon, and (B) aminophenyl-, (C) isocyanate-, and (D) diamine-functionalized 3DOM carbon. Insets show schematically the carbon surface and the surface functionalities. The arrows point to the peaks described in the text.

4.3.2. Voltammetric Response to DNT

Initial characterization of the functionalized electrodes was performed with cyclic voltammetry to allow direct comparison to previously published CV methods for the detection of nitroaromatic molecules.[396,420] In one such study, a detection limit of 5 ppb for 2,4-DNT was achieved using cyclic voltammetry with a glassy carbon electrode modified with multiwalled carbon nanotubes. Several other nitroaromatic compounds could also be detected at higher detection limits.[421] A similar method was used to detect TNT and DNT with glassy carbon electrodes modified with ordered mesoporous carbon using adsorptive stripping voltammetry to achieve a detection limit of 1 ppb for 2,4-DNT.[422] Mesoporous silica (MCM-41) modified electrodes have also been used to detect 2,4-DNT and other nitroaromatic compounds.[423]

Before testing the fully functionalized 3DOM carbon electrodes for their response to DNT, a gold electrode was used to investigate the reduction behavior of DNT in electrolyte solution (NBu_4BArF_{24} in benzotrifluoride) (Figure 4.7). After addition of 0.3 mM DNT to the electrolyte solution, two reduction waves appeared at −1.2 and −1.5 V vs Ag/Ag^+. As expected, the magnitude of the peaks increased as the concentration of DNT in the solution increased to 0.6 mM. The presence of two reduction waves for DNT is consistent with previous work for nitrobenzene and 1,4-dinitrobenzene in acetonitrile.[424] In this previous work, a single reduction wave at −1.505 V vs Ag/Ag^+ was observed for nitrobenzene while two reduction waves at −1.078 and −1.278 V vs Ag/Ag^+ were observed for 1,4-dinitrobenzene. On the basis of the behavior of the gold microelectrode, reduction peak(s) for DNT were expected at approximately −1.5 V for the modified 3DOM carbon electrode.

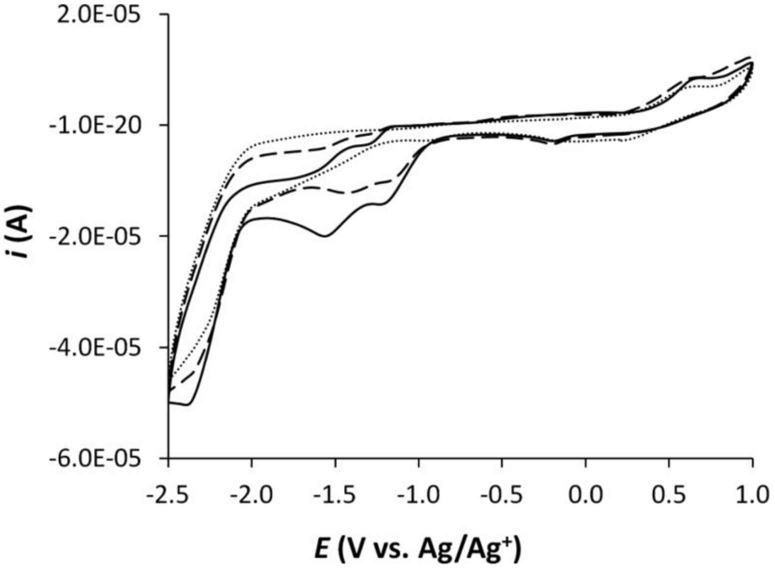

Figure 4.7. CV characterization of a gold electrode in benzotrifluoride/100 mM NBu_4BArF_{24} with varied DNT concentrations (····· 0 mM, — – – 0.3 mM, and — 0.6 mM). A scan window of −2.5 to +1 V starting at +0.2 V was used, with a scan rate of 100 $mV \cdot s^{-1}$. Only cycle 2 is shown.

When obtaining voltammograms of the fully modified 3DOM carbon electrodes, a wide scan window (+2 to −5 V) was used to ensure that all possible peaks were observed. A slower scan rate (10 $mV \cdot s^{-1}$) was also required to obtain a well-shaped voltammogram. DNT concentrations of 0, 0.4, and 0.8 mM DNT were tested (Figure 4.8A). After addition of 0.4 mM DNT, the current increased beginning at −1.0 V as compared to the background scan with 0 mM DNT. After addition of an additional 0.4 mM DNT (for a total of 0.8 mM DNT), a well-defined peak at about −1.7 V was observed. The magnitude of the peak continued to increase as the concentration of DNT in the solution was increased (data not shown).

4.3.3. Response of Unfunctionalized 3DOM Carbon

The response of unfunctionalized 3DOM carbon electrodes to DNT was tested in an identical manner to the functionalized electrodes (Figure 4.8B). The first noticeable difference between the voltammograms of unfunctionalized and functionalized carbon is the total current, which is much larger for the unfunctionalized carbon. The electrochemical functionalization process blocks some micropores in the functionalized electrodes, lowering the surface area compared to the unfunctionalized electrodes. A baseline voltammogram (0 mM DNT) overlaps very well with voltammograms in solutions containing 0.2 and 0.6 mM DNT, indicating a lack of response of unfunctionalized 3DOM carbon electrodes to DNT. Detection of DNT occurred only after modification of the electrode, giving selective detection of DNT with this method.

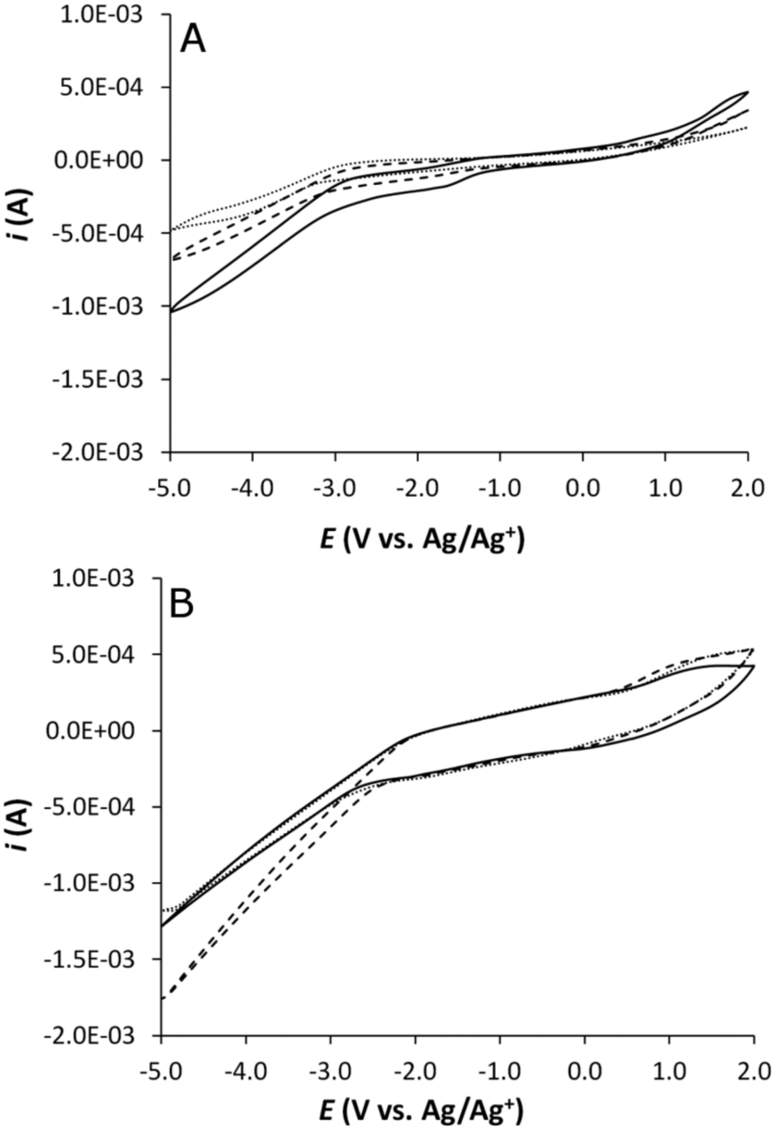

Figure 4.8. (A) CV characterization of a fully functionalized 3DOM carbon electrode in benzotrifluoride/100 mM NBu_4BArF_{24} with varied DNT concentrations (····· 0 mM, − − − − 0.4 mM, and — 0.8 mM). (B) CV characterization of an unfunctionalized 3DOM carbon electrode in benzotrifluoride/100 mM NBu_4BArF_{24} with varied DNT concentrations (····· 0 mM, − − − − 0.2 mM, and — 0.6 mM). A scan window of −5 to 2 V starting at −0.4 V was used, with a scan rate of 10 $mV{\cdot}s^{-1}$; for each experiment, only the 2nd cycle is shown.

4.3.4. Detection of DNT in the Presence of Potential Interferents

Functionalized 3DOM carbon electrodes were tested for response to DNT in the presence of two potential interferents, nitrobenzene and phenol (Figure 4.9). After a baseline voltammogram (0 mM DNT) was measured, the response to nitrobenzene was tested. In the presence of 1.0 mM nitrobenzene, no response was observed, and the total current decreased slightly due to nitrobenzene blocking the surface. The electrode was responsive to DNT (0.6 mM) even in the presence of nitrobenzene (1.0 mM), producing a peak at –2.5 V.

When a functionalized electrode was tested in the presence of phenol (1.0 mM), the total current decreased, as was observed in the nitrobenzene case, indicating no response to phenol. When DNT (0.6 mM) was added to the system, no response to DNT was observed. It was hypothesized that the phenol was blocking the receptor sites. In order to test this hypothesis, the electrode was placed under vacuum overnight in order to remove the phenol, which has a high vapor pressure, from the electrode. After removal of the phenol, the receptor once again responded to DNT.

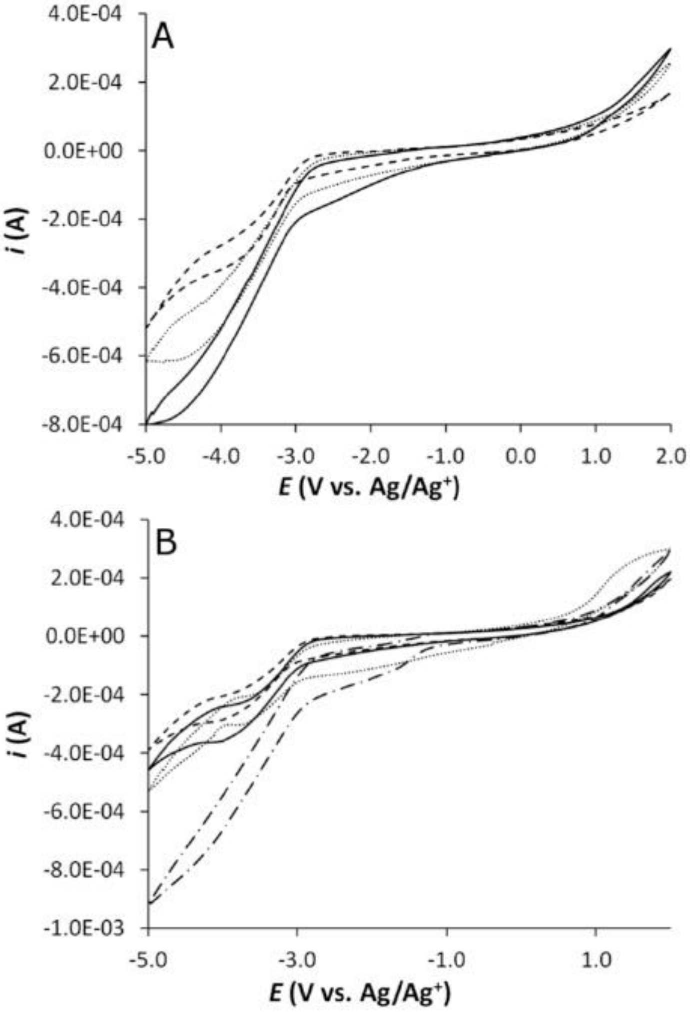

Figure 4.9. CV characterization of fully functionalized 3DOM carbon electrodes in the presence of interferents in benzotrifluoride/100 mM NBu_4BArF_{24}. A scan window of –5 to 2 V starting at –0.4 V was used, with a scan rate of 10 $mV{\cdot}s^{-1}$. Only cycle 2 is shown. The interferents used were (A) nitrobenzene (····· 0 mM nitrobenzene, 0 mM DNT), (– – – – 1.0 mM nitrobenzene, 0 mM DNT), (—— 1.0 mM nitrobenzene, 0.6 mM DNT) and (B) phenol (····· 0 mM phenol, 0 mM DNT), (– – – – 1.0 mM phenol, 0 mM DNT), (—— 1.0 mM phenol, 0.6 mM DNT), (— · — 0 mM phenol, 1 mM DNT after vacuum removal of phenol).

4.3.5. Square Wave Voltammetry

Although cyclic voltammetry demonstrates a response of the fully functionalized 3DOM carbon electrodes to DNT, the peak sizes are quite small. The rather poor limit of detection is not due to poor sensitivity of the technique, but rather an inability to distinguish between Faradaic and capacitive currents.[425] Because of the large capacitance of 3DOM carbon in an electrolyte solution,[318] the electrodes developed here are especially vulnerable to this limitation of cyclic voltammetry. Various techniques have been developed that allow for elimination of capacitive currents.[426] Of these, square wave voltammetry (SWV) is an extremely attractive technique for determination of analytes with electrodes that have rather large capacitance.[425,426] SWV has been well-characterized in the literature.[427-430] In addition, it has been used in recent attempts to detect explosive compounds,[431,432] including a study utilizing carbon fiber electrodes.[396] Square wave voltammetry was used here to investigate the response of the electrodes to DNT while eliminating the signal from the capacitance of the electrode, with the goal of obtaining a lower detection limit.

4.3.5.1. Optimization of SWV Parameters

When using square wave voltammetry, the optimal square wave (SW) pulse length must first be determined. To this extent, a solution of 1 mM DNT was interrogated with varying pulse lengths. As shown in Figure 4.10, the peak current observed for the reduction of DNT increased with increasing pulse length up to 500 ms, where the current began decreasing with subsequent increases in pulse length. This observation may be explained as follows: at rather short pulse lengths, the current observed is largely capacitive,[433] whereas at rather long lengths, the DNT contained in the pores of the 3DOM carbon is largely consumed and the current observed results solely from diffusion to the surface of the electrode. Consequently, a 500 ms pulse length was used for all subsequent experiments.

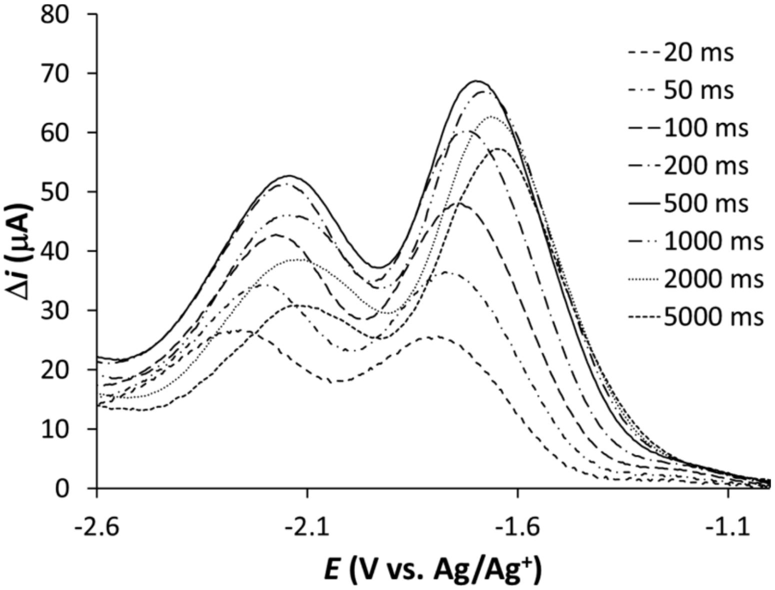

Figure 4.10. Square wave voltammograms of 1 mM DNT at a functionalized 3DOM carbon electrode in benzotrifluoride/100 mM NBu_4BArF_{24} with varied square wave pulse lengths (20−5000 ms). T = 20 °C, SW amplitude = 101 mV, potential step = 5 mV.

When using SWV, it is also necessary to determine the optimal SW amplitude. Shown in Figure 4.11 is the dependence of the peak current upon the SW amplitude.

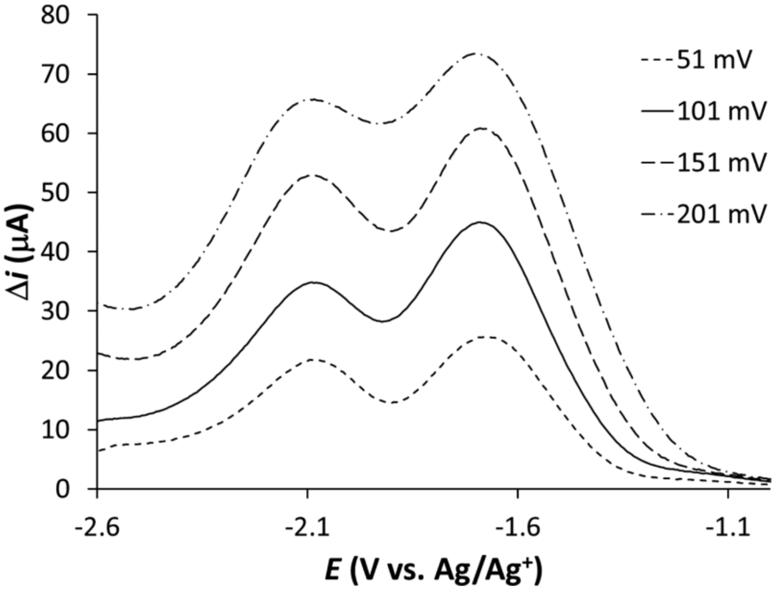

Figure 4.11. Square wave voltammograms of 1 mM DNT at a functionalized 3DOM carbon electrode in benzotrifluoride/100 mM NBu_4BArF_{24} with varied square wave amplitude (51−201 mV). T = 20°C, SW pulse length = 500 ms, potential step = 5 mV.

As observed in Figure 4.11, the peak current for the reduction of DNT increased with increasing SW amplitude. Also, as the SW amplitude increased, there was a marked decrease in the resolution between the two reductions observed for DNT. These effects are consistent with the theory of SWV response.[425] While it may seem advantageous to choose an extremely large SW amplitude, the corresponding loss in resolution is undesirable for analytical applications. Therefore, an amplitude of 101 mV was chosen as a compromise between current sensitivity and resolution for all subsequent experiments.

4.3.5.2. Determination of Limit of Detection

The limit of detection for SWV with the fully functionalized electrodes was determined by addition of DNT. The relationship between the maximum current observed at −1750 mV and the concentration of DNT in solution is shown in Figure 4.12.

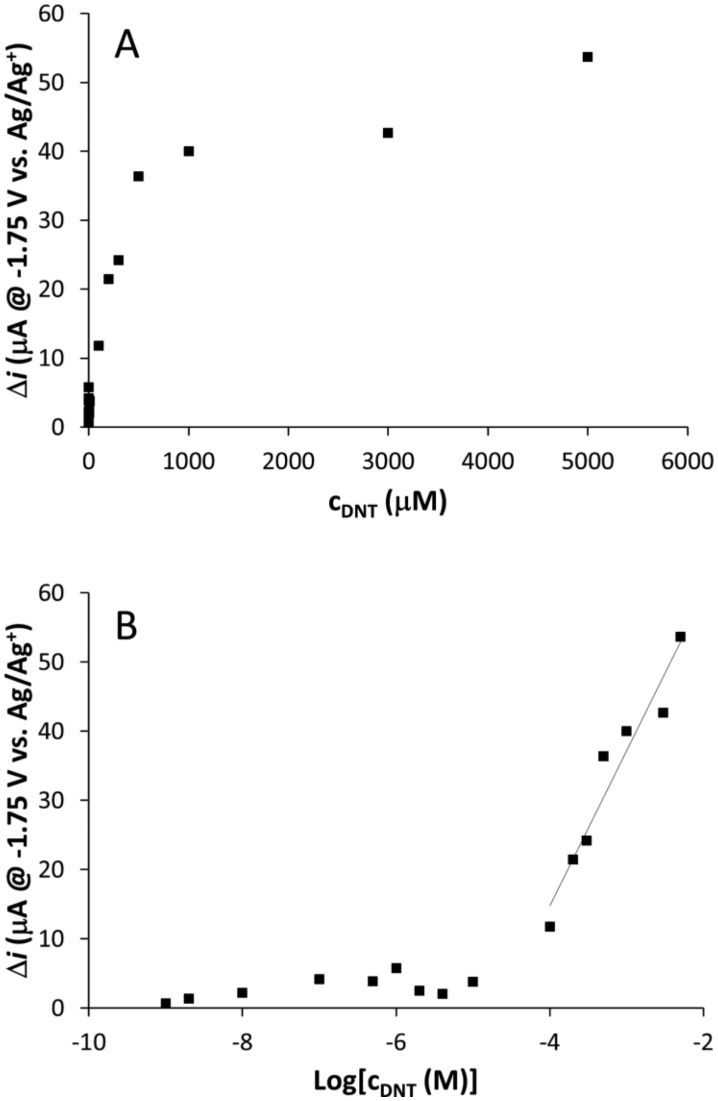

Figure 4.12. Dependence of the current observed by SWV at −1750 mV on (A) DNT concentration and (B) logarithm of DNT concentration at a functionalized 3DOM carbon electrode in benzotrifluoride/100 mM NBu_4BArF_{24}. T = 20 °C, SW pulse length = 500 ms, SW amplitude = 101 mV, potential step = 5 mV.

Inspection of the relationship between peak current and concentration observed in Figure 4.12 reveals that DNT may be adsorbed onto the surface of 3DOM carbon prior to detection. As shown in Figure 4.12B, there is a linear relationship between the peak current and the logarithm of the DNT concentration above 1 × 10^{-4} M. This strongly suggests that adsorbed DNT is indeed being detected by SWV, as expected. A detection limit of 10 μM was obtained, which is comparable to a previously published detection limit of 5 μM for TNT in acetonitrile by SWV with a glassy carbon electrode.[394] Moreover, with an unfunctionalized 3DOM carbon electrode no signal was observed for DNT by SWV at concentrations below 200 μM (see Figure 4.13). The poor limit of detection for the unmodified electrode indicates a rather large preconcentration of DNT at the surface of the modified electrodes, resulting from the interaction of DNT with the receptors that have been linked to the electrode surface.

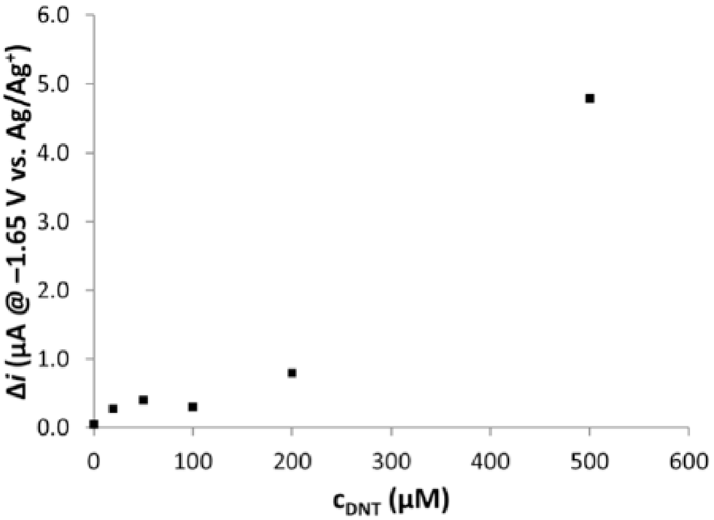

Figure 4.13. Dependence of the current observed by SWV (at –1650 mV) on DNT concentration when using an unfunctionalized 3DOM carbon electrode in benzotrifluoride/100 mM NBu_4BArF_{24}. T = 20 °C, SW pulse length = 500 ms, SW amplitude = 101 mV, potential step = 5 mV.

Lastly, SWV was performed with 1 mM solutions of the electroactive interferent nitrobenzene to determine the limit of detection for DNT in the presence of an electroactive molecule. Because nitrobenzene is electroactive and present in a rather large concentration, the electrode shows a response at −2.0 V for this molecule. However, as shown in Figure 4.14, the presence of nitrobenzene in the solution does not affect the limit of detection observed for DNT. As before, the shape of the current−concentration relationship in the presence of nitrobenzene strongly suggests that adsorbed DNT is being detected. This indicates that the binding coefficient of the receptor toward DNT is substantially stronger than that for nitrobenzene.

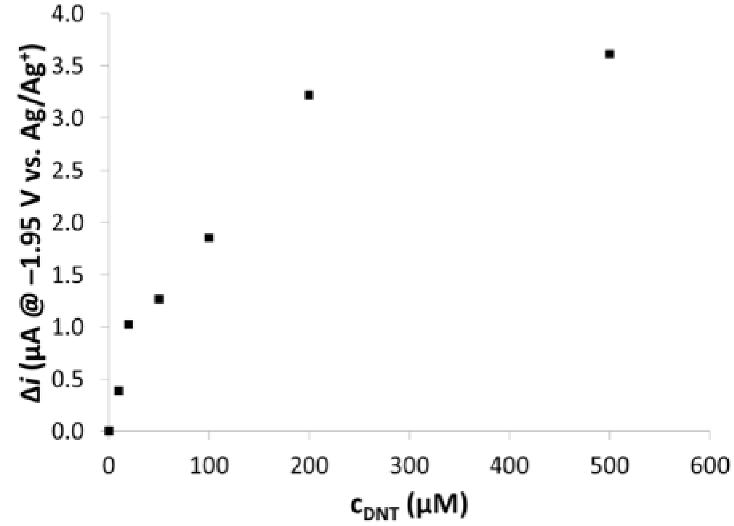

Figure 4.14. Dependence of the corrected current observed by SWV (at –1950 mV) on DNT concentration using a functionalized 3DOM carbon electrode in benzotrifluoride/100 mM NBu_4BArF_{24}, with 1.0 mM nitrobenzene added. Data is corrected by subtraction of the current observed at –1.95 V for a solution of 1 mM nitrobenzene in the absence of DNT. T = 20 °C, SW pulse length = 500 ms, SW amplitude = 101 mV, potential step = 5 mV.

4.4. Conclusion

In this work, the pore walls of 3DOM carbon electrodes were successfully modified with DNT receptors. DNT was detected by cyclic voltammetry, but this requires a high concentration to give even a small peak due to the high surface area, and consequently large interfacial capacitance, of the 3DOM carbon electrode. To overcome this problem, square wave voltammetry was used, resulting in a detection limit of 10 μM for DNT. The concentration dependence of the observed current indicates that receptor-bound DNT is being detected at all but the highest DNT concentrations, where DNT diffusion to the electrode starts to dominate. Moreover, the addition of receptor molecules to the surface of the 3DOM carbon electrodes provides selectivity for DNT over interferents such as nitrobenzene. These receptors were designed to take advantage of the slightly acidic nature of DNT while at the same time including hydrogen-bond-donating sites to further stabilize the deprotonated DNT and thus increase the binding affinity for DNT. The application of these receptor-based sensors to real life samples will be able to take advantage of further preconcentration when DNT (which has a relatively high preference for organic phases and a low vapor pressure) partitions between aqueous or gaseous samples and the organic electrolyte solutions used in this work. It remains to be seen to what extent this will lower detection limits of analysis methods based on these receptor-modified electrodes.

Chapter Five

Summary and Outlook

5.1. Interpenetrating Electrochemical Cell with 3DOM Carbon as the Anode, and Ruthenia/Vanadia as the Cathode

Early investigations into a three-dimensional interpenetrating electrochemical cell with a 3DOM carbon anode, a polymer separator layer, and a vanadia cathode seemed promising for devices requiring a large amount of energy within a small areal footprint.[239,244] The performance of the system was limited by the poor conductivity of the vanadia cathode. The viability of the entire system as a commercial solution for energy needs was hindered by the long synthesis time of an entire cell. In this work, an attempt was made to improve the conductivity of the cathode material by doping with a conductive material (ruthenia), and to increase the efficiency of the synthesis process.

The time required for the deposition of the polymer separator layer was decreased from four days to one day by encasing the anode current collector in PVC. The PVC offers the additional advantage of preventing direct contact between the current collector and the cathode material(s), thereby reducing the possibility of short circuits within the completed cells. A method for controlling the deposition of the ruthenia cathode in the pores of the 3DOM carbon anode was optimized. The amount of ruthenia deposited was also controlled by changing the concentration of the ruthenia precursor (RuO_4) in the solution. After the cryogenic deposition, the as-prepared ruthenia was in a hydrated state ($RuO_2{\cdot}xH_2O$), which would negatively affect the cycling of the cell. A mild procedure for producing anhydrous ruthenia was developed that would not damage the polymer separator layer on the 3DOM carbon anode. Unfortunately, this method did not produce highly conductive RuO_2 as desired, which would require higher temperatures (and thereby destroy the separator layer).

While the need for power, especially in small devices, is likely going to continue to increase, it does not seem like an interpenetrating cell based on 3DOM carbon as the anode is the long-term solution. While the concept seems promising and the chemistry necessary at each step seems compatible with the other steps (except the production of ruthenia that is crystalline and anhydrous while preserving the integrity of the separator layer), the overall process is too complicated. There are too many steps, too many time consuming steps, and many opportunities for damage to occur to the cells. The problems encountered (besides the chemistry/engineering problems we were attempting to overcome) seemed random, which made them difficult to anticipate and/or surmount. While it may be possible to use this process (with a different cathode dopant) to produce an occasional working cell, the concept is not an effective or efficient way to consistently produce cycleable cells.

The two consistent issues that hindered progress when constructing interpenetrating electrochemical cells were the lithiation process and the presence of the polymeric separator layer. Choosing an anode or cathode material that contains lithium ions would eliminate the need for the lithiation step, as well as prevent self-discharge of the cell during the synthesis process. The polymeric separator layer prevented the use of a lot of common electrode materials because only low temperature synthetic steps could be performed. The use of an inorganic solid-state separator layer would allow for the use of a wider range of available materials.

5.2. Ion-Selective Electrodes with 3DOM Carbon as the Solid Contact

An ion-selective electrode system with 3DOM carbon as a solid contact was developed. This system resolved many of the issues of ion-selective electrodes with inner filling solutions (inability to miniaturize the electrode, need to optimize the inner filling solution for the sample solution, high level of maintenance/training required), as well as those that utilize a solid contact (susceptibility to interference, poor signal stability). To construct an ion-selective electrode, a 3DOM carbon electrode was covered with an ionophore-doped sensing membrane. The identity of the ionophore dictates the selectivity of the electrode for a particular analyte. Here, valinomycin was used to produce K^+-selective electrodes, and the use of *o*-xylylenebis(N,N-diisobutyldithiocarbamate) led to electrodes selective for Ag^+. Unprecedented electrode stabilities and detection limits were achieved. After optimization of each component of the system, a detection limit of 4.3 ppt was obtained for Ag^+, which was two orders of magnitude lower than any previously reported Ag^+ system. In addition, the system was resistant to interference from common interferents such as carbon dioxide and light.

The reasons for the excellent performance of the system were investigated using a wide variety of characterization techniques including cryo scanning electron microscopy, quantification of surface functional groups using acid-base titration, cyclic voltammetry, chronopotentiometry, and electrochemical impedance spectroscopy. The important properties which lead to the unprecedented performance of this system include the high surface area of the 3DOM carbon (allowing for a large interfacial area between the carbon and the sensing membrane), and a low concentration of functional groups on the pore walls.

The use 3DOM carbon as a solid contact for sensors will continue to expand because of the excellent performance of the system, as well as its versatility. An electrode for a particular ion or small molecule can (theoretically) be developed as long as an ionophore selective for the analyte of choice is available. Optimization of the system obviously has to occur, but an entirely new electrode system is not required. Since these electrodes do not require the use of an inner filling solution, miniaturization of the electrode system may be possible.

The expansion of applications for 3DOM carbon-based electrodes has already begun to occur. Because of the excellent stability of the system, it has been used in conjunction with an ionic liquid to produce a reference electrode system with 3DOM carbon as the solid contact.[401] A 3DOM carbon ion-selective has also been used to detect perfluorocarbon surfactants (persistent environmental pollutants), and has been demonstrated to perform well with real-world samples.[434]

5.3. Receptor-Based Sensor for 2,4-Dinitrotoluene with 3DOM Carbon as the Foundation

A sensor to selectively detect 2,4-dinitrotoluene (a common byproduct of the explosive material 2,4,6-trinitrotoluene [TNT]), even in the presence of interferents was developed. The pore walls of a 3DOM carbon electrode were modified with a receptor specifically designed for DNT through a series of chemical and electrochemical modification steps. When cyclic voltammetry was used as the electrochemical detection method, selective detection of DNT was observed for receptor-modified electrodes, but the detection limit was rather poor because of the capacitive current observed in the voltammogram (due to the large surface area of the 3DOM carbon). When square wave voltammetry was used as the detection method (which eliminates the capacitive current), the detection limit observed was improved. While many detection methods for DNT exist, most take advantage of the redox activity of the molecule, and use the reduction potential observed to determine identity of the analyte in solution. In this system, the receptor interacts only with the analyte of interest (even in the presence of similar molecules such as nitrobenzene), allowing for selective detection.

While the adaptability of this sensor system is not as straightforward as that of the ion-selective electrode system described above, the detection of other analytes using a similar electrode is feasible. A new receptor would need to be designed for each analyte of interest. Then, a synthesis scheme to attach the receptor to the surface of the carbon (or synthesize the receptor piece-by-piece) would be required. However, this is not as daunting of a task as it initially seems. The initial two steps used in the synthesis of the DNT receptor described here (reaction with an azo compound to form nitro-functionalized carbon, followed by electrochemical reduction to produce amino-functionalized carbon) are well established. The presence of an amine on the surface of the carbon opens the door for a wide variety of further chemical functionalization steps which should allow the synthesis of a wide variety of receptors. After the successful synthesis of a receptor, the solvent and electrolyte also need to be considered. Another potential expansion of this system is to eliminate the need for a solvent altogether and detect small molecules in the gas phase.

References

(1) Stein, A.; Wang, Z.; Fierke, M. A. *Adv. Mater.* **2009**, *21*, 265–293.

(2) Falcao, E. H. L.; Wudl, F. *J. Chem. Technol. Biotechnol.* **2007**, *82*, 524–531.

(3) Kinoshita, K. *Carbon: Electrochemical and Physicochemical Properties*; John Wiley & Sons: New York, 1988.

(4) Yang, X.-Y.; Léonard, A.; Lemaire, A.; Tian, G.; Su, B.-L. *Chem. Commun. (Cambridge, U. K.)* **2011**, *47*, 2763–2786.

(5) Polarz, S.; Antonietti, M. *Chem. Commun. (Cambridge, U. K.)* **2002**, 2593–2604.

(6) Barton, T. J.; Bull, L. M.; Klemperer, W. G.; Loy, D. A.; McEnaney, B.; Misono, M.; Monson, P. A.; Pez, G.; Scherer, G. W.; Vartuli, J. C.; Yaghi, O. M. *Chem. Mater.* **1999**, *11*, 2633–2656.

(7) Sing, K. S. W.; Everett, D. H.; Haul, R. A. W.; Moscou, L.; Pierotti, R. A.; Rouquérol, J.; Siemieniewska, T. *Pure Appl. Chem.* **1985**, *57*, 603–619.

(8) Miura, K.; Hayashi, J. *Carbon* **1991**, *29*, 653–660.

(9) Miura, K.; Hayashi, J.; Hashimoto, K. *Carbon* **1992**, *30*, 946–947.

(10) Su, F.; Zhao, X. S.; Lv, L.; Zhou, Z. *Carbon* **2004**, *42*, 2821–2831.

(11) Zhao, X. S.; Su, F.; Yan, Q.; Guo, W.; Bao, X. Y.; Lv, L.; Zhou, Z. *J. Mater. Chem.* **2006**, *16*, 637–648.

(12) Ryoo, R.; Joo, S. H.; Jun, S. *J. Phys. Chem. B* **1999**, *103*, 7743–7746.

(13) Chuenchom, L.; Kraehnert, R.; Smarsly, B. M. *Soft Matter* **2012**, *8*, 10801–10812.

(14) Liang, C.; Hong, K.; Guiochon, G. A.; Mays, J. W.; Dai, S. *Angew. Chem., Int. Ed.* **2004**, *43*, 5785–5789.

(15) Lee, J.; Kim, J.; Hyeon, T. *Adv. Mater.* **2006**, *18*, 2073–2094.

(16) Huang, Y.; Cai, H.; Feng, D.; Gu, D.; Deng, Y.; Tu, B.; Wang, H.; Webley, P. A.; Zhao, D. *Chem. Commun. (Cambridge, U. K.)* **2008**, 2641–2643.

(17) Velev, O. D.; Kaler, E. W. *Adv. Mater.* **2000**, *12*, 531–534.

(18) Stein, A.; Schroden, R. C. *Curr. Opin. Solid State Mater. Sci.* **2001**, *5*, 553–564.

(19) Stein, A. *Microporous Mesoporous Mater.* **2001**, *44–45*, 227–239.

(20) Xia, Y.; Gates, B.; Yin, Y.; Lu, Y. *Adv. Mater.* **2000**, *12*, 693–713.

(21) Stein, A.; Li, F.; Denny, N. R. *Chem. Mater.* **2008**, *20*, 649–666.

(22) Velev, O. D.; Jede, T. A.; Lobo, R. F.; Lenhoff, A. M. *Nature (London, U.K.)* **1997**, *389*, 447–448.

(23) Velev, O. D.; Jede, T. A.; Lobo, R. F.; Lenhoff, A. M. *Chem. Mater.* **1998**, *10*, 3597–3602.

(24) Imhof, A.; Pine, D. J. *Nature (London, U.K.)* **1997**, *389*, 948–951.

(25) Holland, B. T.; Blanford, C. F.; Stein, A. *Science (Washington, DC, U.S.)* **1998**, *281*, 538–540.

(26) Holland, B. T.; Blanford, C. F.; Do, T.; Stein, A. *Chem. Mater.* **1999**, *11*, 795–805.

(27) Wijnhoven, J. E. G. J.; Vos, W. L. *Science (Washington, DC, U.S.)* **1998**, *281*, 802–804.

(28) Yin, J. S.; Wang, Z. L. *Adv. Mater.* **1999**, *11*, 469–472.

(29) Yang, P. D.; Deng, T.; Zhao, D. Y.; Feng, P. Y.; Pine, D.; Chmelka, B. F.; Whitesides, G. M.; Stucky, G. D. *Science (Washington, DC, U.S.)* **1998**, *282*, 2244–2246.

(30) Yan, H.; Blanford, C. F.; Holland, B. T.; Parent, M.; Smyrl, W. H.; Stein, A. *Adv. Mater.* **1999**, *11*, 1003–1006.

(31) Yan, H.; Blanford, C. F.; Holland, B. T.; Smyrl, W. H.; Stein, A. *Chem. Mater.* **2000**, *12*, 1134–1141.

(32) Wu, Q. Z.; Shen, Y.; Liao, J. F.; Li, Y. G. *Mater. Lett.* **2004**, *58*, 2688–2691.

(33) Meseguer, F.; Blanco, A.; Míguez, H.; García-Santamaría, F.; Ibisate, M.; López, C. *Colloids Surf., A* **2002**, *202*, 281–290.

(34) Zakhidov, A. A.; Baughman, R. H.; Iqbal, Z.; Cui, C.; Khayrullin, I.; Dantas, S. O.; Marti, J.; Ralchenko, V. G. *Science (Washington, DC, U.S.)* **1998**, *282*, 897–901.

(35) Su, F.; Zhao, X. S.; Wang, Y.; Zeng, J.; Zhou, Z.; Lee, J. Y. *J. Phys. Chem. B* **2005**, *109*, 20200–20206.

(36) Yoon, S. B.; Chai, G. S.; Kang, S. K.; Yu, J.-S.; Gierszal, K. P.; Jaroniec, M. *J. Am. Chem. Soc.* **2005**, *127*, 4188–4189.

(37) Rugge, A.; Becker, J. S.; Gordon, R. G.; Tolbert, S. H. *Nano Lett.* **2003**, *3*, 1293–1297.

(38) Romanov, S. G.; Maka, T.; Sotomayor Torres, C. M.; Müller, M.; Zentel, R. *Appl. Phys. Lett.* **2001**, *79*, 731–733.

(39) Kulinowski, K. M.; Jiang, P.; Vaswani, H.; Colvin, V. L. *Adv. Mater.* **2000**, *12*, 833–838.

(40) Denny, N. R.; Han, S. E.; Norris, D. J.; Stein, A. *Chem. Mater.* **2007**, *19*, 4563–4569.

(41) Yu, X.; Lee, Y.-J.; Furstenberg, R.; White, J. O.; Braun, P. V. *Adv. Mater.* **2007**, *19*, 1689–1692.

(42) Jiang, P.; Cizeron, J.; Bertone, J. F.; Colvin, V. L. *J. Am. Chem. Soc.* **1999**, *121*, 7957–7958.

(43) Yan, H.; Blanford, C. F.; Lytle, J. C.; Carter, C. B.; Smyrl, W. H.; Stein, A. *Chem. Mater.* **2001**, *13*, 4314–4321.

(44) Yan, H.; Blanford, C. F.; Smyrl, W. H.; Stein, A. *Chem. Commun. (Cambridge, U.K.)* **2000**, 1477–1478.

(45) Vlasov, Y. A.; Yao, N.; Norris, D. J. *Adv. Mater.* **1999**, *11*, 165–169.

(46) Brown, P. V.; Wiltzius, P. *Nature (London, U.K.)* **1999**, *402*, 603–604.

(47) Park, S. H.; Xia, Y. *Adv. Mater.* **1998**, *10*, 1045–1048.

(48) Jiang, P.; Hwang, K. S.; Mittleman, D. M.; Bertone, J. F.; Colvin, V. L. *J. Am. Chem. Soc.* **1999**, *121*, 11630–11637.

(49) Wang, D.; Caruso, F. *Adv. Mater.* **2001**, *13*, 350–353.

(50) Holtz, J. H.; Asher, S. A. *Nature (London, U.K.)* **1997**, *389*, 829–832.

(51) Barry, R. A.; Wiltzius, P. *Langmuir* **2006**, *22*, 1369–1374.

(52) Zhang, Y.; Wang, S.; Eghtedari, M.; Motamedi, M.; Kotov, N. A. *Adv. Funct. Mater.* **2005**, *15*, 725–731.

(53) Schroden, R. C.; Al-Daous, M.; Blanford, C. F.; Stein, A. *Chem. Mater.* **2002**, *14*, 3305–3315.

(54) Schroden, R. C.; Al-Daous, M.; Sokolov, S.; Melde, B. J.; Lytle, J. C.; Stein, A.; Carbajo, M. C.; Fernández, J. T.; Rodríguez, E. E. *J. Mater. Chem.* **2002**, *12*, 3261–3267.

(55) Guo, Y.; Yang, Y.; Hu, C.; Guo, C.; Wang, E.; Zou, Y.; Feng, S. *J. Mater. Chem.* **2002**, *12*, 3046–3052.

(56) Wang, Z.; Ergang, N. S.; Al-Daous, M. A.; Stein, A. *Chem. Mater.* **2005**, *17*, 6805–6813.

(57) Sorensen, E. M.; Barry, S. J.; Jung, H.-K.; Rondinelli, J. R.; Vaughey, J. T.; Poeppelmeier, K. R. *Chem. Mater.* **2006**, *18*, 482–489.

(58) Waterhouse, G. I. N.; Metson, J. B.; Idriss, H.; Sun-Waterhouse, D. *Chem. Mater.* **2008**, *20*, 1183–1190.

(59) You, B.; Shi, L.; Wen, N.; Liu, X.; Wu, L.; Zi, J. *Macromolecules (Washington, DC, U. S.)* **2008**, *41*, 6624–6626.

(60) Li, J.; Zhao, X.; Wei, H.; Gu, Z.-Z.; Lu, Z. *Anal. Chim. Acta* **2008**, *625*, 63–69.

(61) Kavan, L.; Zukalová, M.; Kalbáč, M.; Graetzel, M. *J. Electrochem. Soc.* **2004**, *151*, A1301–A1307.

(62) Denny, N. R.; Han, S.; Turgeon, R. T.; Lytle, J. C.; Norris, D. J.; Stein, A. *Proc. SPIE* **2005**, *6005*, 60050501–60050513.

(63) Lee, K. T.; Lytle, J. C.; Ergang, N. S.; Oh, S. M.; Stein, A. *Adv. Funct. Mater.* **2005**, *15*, 547–556.

(64) Li, F.; Wang, Z.; Ergang, N. S.; Fyfe, C. A.; Stein, A. *Langmuir* **2007**, *23*, 3996–4004.

(65) Wang, X.; Bozhilov, K. N.; Feng, P. *Chem. Mater.* **2006**, *18*, 6373–6381.

(66) Tabata, S.; Isshiki, Y.; Wantanabe, M. *J. Electrochem. Soc.* **2008**, *155*, K42−K49.

(67) Kamp, U.; Kitaev, V.; von Freymann, G.; Ozin, G. A.; Mabury, S. A. *Adv. Mater.* **2005**, *17*, 438−443.

(68) Li, F.; He, J.; Zhou, W. L.; Wiley, J. B. *J. Am. Chem. Soc.* **2003**, *125*, 16166−16167.

(69) Fu, M.; Zhou, J.; Xiao, Q.; Li, B.; Zong, R.; Chen, W.; Zhang, J. *Adv. Mater.* **2006**, *18*, 1001−1004.

(70) Blanco, A.; Chomski, E.; Grabtchak, S.; Ibisate, M.; John, S.; Leonard, S. W.; Lopez, C.; Meseguer, F.; Miguez, H.; Mondia, J. P.; Ozin, G. A.; Toader, O.; van Driel, H. M. *Nature (London, U.K.)* **2000**, *405*, 437−440.

(71) Vlasov, Y. A.; Bo, X.-Z.; Sturm, J. C.; Norris, D. J. *Nature (London, U.K.)* **2001**, *414*, 289−293.

(72) Li, B.; Zhou, J.; Li, L.; Wang, X. J.; Liu, X. H.; Zi, J. *Appl. Phys. Lett.* **2003**, *83*, 4704–4706.

(73) Blanford, C. F.; Yan, H.; Schroden, R. C.; Al-Daous, M.; Stein, A. *Adv. Mater.* **2001**, *13*, 401–407.

(74) Arsenault, A. C.; Clark, T. J.; von Freymann, G.; Cademartiri, L.; Sapienza, R.; Bertolotti, J.; Vekris, E.; Wong, S.; Kitaev, V.; Manners, I.; Wang, R. Z.; John, S.; Wiersma, D.; Ozin, G. A. *Nat. Mater.* **2006**, *5*, 179−184.

(75) Fudouzi, H.; Xia, Y. *Langmuir* **2003**, *19*, 9653–9660.

(76) Perpall, M. W.; Perera, K. P. U.; DiMaio, J.; Ballato, J.; Foulger, S. H.; Smith Jr., D. W. *Langmuir* **2003**, *19*, 7153–7156.

(77) Scott, R. W. J.; Yang, S. M.; Chabanis, G.; Coombs, N.; Williams, D. E.; Ozin, G. A. *Adv. Mater.* **2001**, *13*, 1468–1472.

(78) Song, Y.-Y.; Zhang, D.; Gao, W.; Xia, X.-H. *Chem. Eur. J.* **2005**, *11*, 2177−2182.

(79) Al-Daous, M. A.; Stein, A. *Chem. Mater.* **2003**, *15*, 2638−2645.

(80) Tian, S.; Wang, J.; Jonas, U.; Knoll, W. *Chem. Mater.* **2005**, *17*, 5726–5730.

(81) Long, J. W.; Dunn, B.; Rolison, D. R.; White, H. S. *Chem. Rev. (Washington, DC, U.S.)* **2004**, *104*, 4463–4492.

(82) Sakamoto, J. S.; Dunn, B. *J. Mater. Chem.* **2002**, *12*, 2859–2861.

(83) Chai, G. S.; Shin, I. S.; Yu, J.-S. *Adv. Mater.* **2004**, *16*, 2057–2061.

(84) Zhang, S.; Chen, L.; Zhou, S.; Zhao, D.; Wu, L. *Chem. Mater.* **2010**, *22*, 3433–3440.

(85) Lei, Z.; Zhang, Y.; Wang, H.; Ke, Y.; Li, J.; Li, F.; Xing, J. *J. Mater. Chem.* **2001**, *11*, 1975–1977.

(86) Take, H.; Matsumoto, T.; Hiwatashi, S.; Nakayama, T.; Niihara, K.; Yoshino, K. *Jpn. J. Appl. Phys.* **2004**, *43*, 4453–4457.

(87) Kang, S.; Yu, J.-S.; Kruk, M.; Jaroniec, M. *Chem. Commun. (Cambridge, U.K.)* **2002**, 1670–1671.

(88) Reculusa, S.; Agricole, B.; Derré, A.; Couzi, M.; Sellier, E.; Delhaès, P.; Ravaine, S. *Electroanalysis* **2007**, *19*, 379–384.

(89) Yu, J.-S.; Kang, S. K.; Yoon, S. B.; Chai, G. S. *J. Am. Chem. Soc.* **2002**, *124*, 9382–9383.

(90) Woo, S.-W.; Dokko, K.; Nakano, H.; Kanamura, K. *J. Mater. Chem.* **2008**, *18*, 1674–1680.

(91) Zhou, Z.; Yan, Q.; Su, F.; Zhao, X. S. *J. Mater. Chem.* **2005**, *15*, 2569–2574.

(92) Wang, Z.; Li, F.; Ergang, N. S.; Stein, A. *Chem. Mater.* **2006**, *18*, 5543–5553.

(93) Taguchi, A.; Smått, J.-H.; Lindén, M. *Adv. Mater.* **2003**, *15*, 1209–1211.

(94) Alvarez, S.; Esquena, J.; Solans, C.; Fuertes, A. B. *Adv. Eng. Mater.* **2004**, *6*, 897–899.

(95) Lu, A.-H.; Smått, J.-H.; Backlund, S.; Lindén, M. *Microporous Mesoporous Mater.* **2004**, *72*, 59–65.

(96) Hu, Y.-S.; Adelhelm, P.; Smarsly, B. M.; Hore, S.; Antonietti, M.; Maier, J. *Adv. Funct. Mater.* **2007**, *17*, 1873–1878.

(97) Tonanon, N.; Siyasukh, A.; Wareenin, Y.; Charinpanitkul, T.; Tanthapanichakoon, W.; Nishihara, H.; Mukai, S. R.; Tamon, H. *Carbon* **2005**, *43*, 2808–2811.

(98) Baumann, T. F.; Worsley, M. A.; Han, T. Y.-J.; Satcher Jr., J. H. *J. Non-Cryst. Solids* **2008**, *354*, 3513–3515.

(99) Cai, X.; Zhu, G.; Zhang, W.; Zhao, H.; Wang, C.; Qiu, S.; Wei, Y. *Eur. J. Inorg. Chem.* **2006**, 3641−3645.

(100) Pierre, A. C. In *Aerogels Handbook*; Aegerter, M. A., Leventis, N., Koebel, M., Eds.; Springer: New York, 2011, p 3–18.

(101) Pekala, R. W. *J. Mater. Sci.* **1989**, *24*, 3221–3227.

(102) Cook, R. C.; Letts, S. A.; Overturf III, G. E.; Lambert, S. M.; Wilemski, G.; Schroen-Carey, D. *Final Report UCRL-LR-105821-97-1*, Lawrence Livermore National Laboratory, 1997.

(103) Pekala, R. W.; Farmer, J. C.; Alviso, C. T.; Tran, T. D.; Mayer, S. T.; Miller, J. M.; Dunn, B. *J. Non-Cryst. Solids* **1998**, *225*, 74–80.

(104) Al-Muhtaseb, S. A.; Ritter, J. A. *Adv. Mater.* **2003**, *15*, 101−114.

(105) Pekala, R. W.; Schaefer, D. W. *Macromolecules (Washington, DC, U. S.)* **1993**, *26*, 5487−5493.

(106) Yamamoto, T.; Nishimura, T.; Suzuki, T.; Tamon, H. *J. Non-Cryst. Solids* **2001**, *288*, 46−55.

(107) Fairén-Jiménez, D.; Carrasco-Martin, F.; Moreno-Castilla, C. *Carbon* **2006**, *44*, 2301−2307.

(108) ElKhatat, A. M.; Al-Muhtaseb, S. A. *Adv. Mater.* **2011**, *23*, 2887–2903.

(109) Brandt, R.; Petricevic, H.; Pröbstle, H.; Fricke, J. *J. Porous Mater.* **2003**, *10*, 171–178.

(110) Scherdel, C.; Scherb, T.; Reichenauer, G. *Carbon* **2009**, *47*, 2244–2252.

(111) Berthon, S.; Barbieri, O.; Ehrburger-Dolle, F.; Geissler, E.; Achard, P.; Bley, F.; Hecht, A.-M.; Livet, F.; Pajonk, G. M.; Pinto, N.; Rigacci, A.; Rochas, C. *J. Non-Cryst. Solids* **2001**, *285*, 154–161.

(112) Pekala, R. W.; Alviso, C. T.; Kong, F. M.; Hulsey, S. S. *J. Non-Cryst. Solids* **1992**, *145*, 90–98.

(113) Lu, X.; Caps, R.; Fricke, J.; Alviso, C. T.; Pekala, R. W. *J. Non-Cryst. Solids* **1995**, *188*, 226–234.

(114) Tamon, H.; Ishizaka, H.; Mikami, M.; Okazaki, M. *Carbon* **1997**, *36*, 791−796.

(115) Sharma, C. S.; Kulkarni, M. M.; Sharma, A.; Madou, M. *Chem. Eng. Sci.* **2009**, *64*, 1536−1543.

(116) Lin, C.; Ritter, J. A. *Carbon* **1997**, *35*, 1271−1278.

(117) Zanto, E. J.; Al-Muhtaseb, S. A.; Ritter, J. A. *Ind. Eng. Chem. Res.* **2002**, *41*, 3151−3162.

(118) Despetis, F.; Barral, K.; Kocon, L.; Phalippou, J. *J. Sol-Gel Sci. Technol.* **2000**, *19*, 829−831.

(119) Czakkel, O.; Marthi, K.; Geissler, E.; László, K. *Microporous Mesoporous Mater.* **2005**, *86*, 124−133.

(120) Job, N.; Théry, A.; Pirard, R.; Marien, J.; Kocon, L.; Rouzaud, J.-N.; Béguin, F.; Pirard, J.-P. *Carbon* **2005**, *43*, 2481−2494.

(121) Liang, C.; Sha, G.; Guo, S. *J. Non-Cryst. Solids* **2000**, *271*, 167−170.

(122) Wei, Y.-Z.; Fang, B.; Iwasa, S.; Kumagai, M. *J. Power Sources* **2005**, *141*, 386−391.

(123) Hwang, S.-W.; Hyun, S.-H. *J. Non-Cryst. Solids* **2004**, *347*, 238−245.

(124) Yamamoto, T.; Sugimoto, T.; Suzuki, T.; Mukai, S. R.; Tamon, H. *Carbon* **2002**, *40*, 1345−1351.

(125) Tamon, H.; Ishizaka, H.; Yamamoto, T.; Suzuki, T. *Carbon* **2000**, *38*, 1099−1105.

(126) Kim, S. J.; Hwang, S. W.; Hyun, S. H. *J. Mater. Sci.* **2005**, *40*, 725−731.

(127) Job, N.; Pirard, R.; Marien, J.; Pirard, J.-P. *Carbon* **2004**, *42*, 619−628.

(128) Lin, C.; Ritter, J. A. *Carbon* **2000**, *38*, 849−861.

(129) Moldonado-Hódar, F. J.; Ferro-García, M. A.; Rivera-Utrilla, J.; Moreno-Castilla, C. *Carbon* **1999**, *37*, 1199−1205.

(130) Horikawa, T.; Hayashi, J. i.; Muroyama, K. *Carbon* **2004**, *42*, 1625−1633.

(131) Rao, C. N. R.; Seshadri, R.; Govindaraj, A.; Sen, R. *Mater. Sci. Enr., R* **1995**, *15*, 209−262.

(132) Dresselhaus, M. S.; Endo, M. *Top. Appl. Phys.* **2001**, *80*, 11–28.

(133) Dresselhaus, M. S.; Avouris, P. *Top. Appl. Phys.* **2001**, *80*, 1–9.

(134) Dai, H. *Acc. Chem. Res.* **2002**, *35*, 1035–1044.

(135) Boehm, H.-P.; Diehl, E.; Heck, W.; Sappok, R. *Angew. Chem., Int. Ed.* **1964**, *3*, 669–677.

(136) Pesin, L. A. *J. Mater. Sci.* **2002**, *37*, 1–28.

(137) Jenkins, G. M.; Kawamura, K. *Nature (London, U.K.)* **1971**, *231*, 175–176.

(138) Liu, Y.; Xue, J. S.; Zheng, T.; Dahn, J. R. *Carbon* **1996**, *34*, 193–200.

(139) Świątkowski, A.; Pakuła, M.; Biniak, S. *Electrochim. Acta* **1997**, *42*, 1441–1447.

(140) Boehm, H. P. *Carbon* **2002**, *40*, 145–149.

(141) Otake, Y.; Jenkins, G. M. *Carbon* **1993**, *31*, 109–121.

(142) Qi, B.; Peng, X.; Fang, J.; Guo, L. *Electroanalysis* **2009**, *21*, 875–880.

(143) Yang, T.; Lua, A. C. *J. Colloid Interface Sci.* **2003**, *267*, 408–417.

(144) Samant, P. V.; Gonçalves, F.; Freitas, M. M. A.; Pereira, M. F. R.; Figueiredo, J. L. *Carbon* **2004**, *42*, 1321–1325.

(145) Hanzawa, Y.; Kaneko, K.; Pekala, R. W.; Dresselhaus, M. S. *Langmuir* **1996**, *12*, 6167–6169.

(146) Salinger, R.; Fischer, U.; Herta, C.; Fricke, J. *J. Non-Cryst. Solids* **1998**, *225*, 81–85.

(147) Lin, C.; Ritter, J. A.; Popov, B. N. *J. Electrochem. Soc.* **1999**, *146*, 3639–3643.

(148) Zou, Y.; Han, B.-X. *Energy Fuels* **2001**, *15*, 1383–1386.

(149) Kandiyoti, R.; Lazaridis, J. I.; Dyrvold, B.; Weerasinghe, C. R. *Fuel* **1984**, *63*, 1583–1587.

(150) Zhu, Y.; Hu, H.; Li, W.; Zhang, X. *Carbon* **2007**, *45*, 160–165.

(151) Ahmadpour, A.; Do, D. D. *Carbon* **1996**, *34*, 471–479.

(152) Hu, Z.; Srinivasan, M. P.; Ni, Y. *Adv. Mater.* **2000**, *12*, 62–65.

(153) Tamai, H.; Kakii, T.; Hirota, Y.; Kumamoto, T.; Yasuda, H. *Chem. Mater.* **1996**, *8*, 454–462.

(154) Marsh, H.; Rand, B. *Carbon* **1971**, *9*, 63–77.

(155) Oya, A.; Yoshida, S.; Alcaniz-Monge, J.; Linares-Solano, A. *Carbon* **1995**, *33*, 1085–1090.

(156) Shrestha, S.; Mustain, W. E. *J. Electrochem. Soc.* **2010**, *157*, B1665–B1672.

(157) Barton, S. S.; Evans, M. J. B.; Halliop, E.; MacDonald, J. A. F. *Carbon* **1997**, *35*, 1361–1366.

(158) Fanning, P. E.; Vannice, M. A. *Carbon* **1993**, *31*, 721–730.

(159) Figueiredo, J. L.; Pereira, M. F. R.; Freitas, M. M. A.; Órfåo, J. J. M. *Carbon* **1999**, *37*, 1379–1389.

(160) Moreno-Castilla, C.; Ferro-García, M. A.; Joly, J. P.; Bautista, T., I.; Carrasco-Marín, F.; Rivera-Utrilla, J. *Langmuir* **1995**, *11*, 4386–4392.

(161) Mahata, N.; Pereira, M. F. R.; Suárez-García, F.; Martínez-Alonso, A.; Tascón, J. M. D.; Figueiredo, J. L. *J. Colloid Interface Sci.* **2008**, *324*, 150–155.

(162) Vinke, P.; van der Eijk, M.; Verbree, M.; Voskamp, A. F.; van Bekkum, H. *Carbon* **1994**, *32*, 675–686.

(163) Pradhan, B. K.; Sandle, N. K. *Carbon* **1999**, *37*, 1323–1332.

(164) Cheng, P.-Z.; Teng, H. *Carbon* **2003**, *41*, 2057–2063.

(165) Bandosz, T. J.; Jagiello, J.; Schwarz, J. A. *Anal. Chem.* **1992**, *64*, 891–895.

(166) Mawhinney, D. B.; Yates Jr., J. T. *Carbon* **2001**, *39*, 1167–1173.

(167) Engstrom, R. C.; Strasser, V. A. *Anal. Chem.* **1984**, *56*, 136–141.

(168) Dekanski, A.; Stevanović, J.; Stevanović, R.; Nikolić, B. Ž.; Jovanović, V. M. *Carbon* **2001**, *39*, 1195–1205.

(169) Tenent, R. C.; Wipf, D. O. *J. Electrochem. Soc.* **2003**, *150*, E131–E139.

(170) Katoh, M.; Miyashita, K.; Ohte, T.; Kaneko, M.; Ohtani, S.; Kojima, A. *J. Photopolym. Sci. Technol.* **1996**, *9*, 213–224.

(171) Arrigo, R.; Hävecker, M.; Wrabetz, S.; Blume, R.; Lerch, M.; McGregor, J.; Parrott, E. P. J.; Zeitler, J. A.; Gladden, L. F.; Knop-Gericke, A.; Schlögl, R.; Su, D. S. *J. Am. Chem. Soc.* **2010**, *132*, 9616–9630.

(172) Boehm, H. P.; Mair, G.; Stoehr, T.; de Rincón, A. R.; Tereczki, B. *Fuel* **1984**, *63*, 1061–1063.

(173) Stöhr, B.; Boehm, H. P. *Carbon* **1991**, *29*, 707–720.

(174) Mangun, C. L.; Benak, K. R.; Economy, J.; Foster, K. L. *Carbon* **2001**, *39*, 1809–1820.

(175) Lee, J.-B.; Park, Y.-K.; Yang, O.-B.; Kang, Y.; Jun, K.-W.; Lee, Y.-J.; Kim, H. Y.; Lee, K.-H.; Choi, W. C. *J. Power Sources* **2006**, *158*, 1251–1255.

(176) Budarin, V. L.; Clark, J. H.; Luque, R.; Macquarrie, D. J. *Chem. Commun. (Cambridge, U.K.)* **2007**, 634–636.

(177) Xing, R.; Liu, Y.; Wang, Y.; Chen, L.; Wu, H.; Jiang, Y.; He, M.; Wu, P. *Microporous Mesoporous Mater.* **2007**, *105*, 41–48.

(178) Coen, M. C.; Keller, B.; Groening, P.; Schlapbach, L. *J. Appl. Phys.* **2002**, *92*, 5077–5083.

(179) Li, Z.; Del Cul, G. D.; Yan, W.; Liang, C.; Dai, S. *J. Am. Chem. Soc.* **2004**, *126*, 12782–12783.

(180) Wang, L.; Zhao, Y.; Lin, K.; Zhao, X.; Shan, Z.; Di, Y.; Sun, Z.; Cao, X.; Zou, Y.; Jiang, D.; Jiang, L.; Xiao, F.-S. *Carbon* **2006**, *44*, 1336–1339.

(181) Mukhopadhyay, S. M.; Pulikollu, R. V.; Roy, A. K. *Appl. Surf. Sci.* **2004**, *225*, 223–228.

(182) Donnet, J. B. *Tanso* **1977**, *88*, 12–33.

(183) Puri, B. R.; Bansal, R. C. *Carbon* **1967**, *5*, 189–194.

(184) Tobias, H.; Soffer, A. *Carbon* **1985**, *23*, 281–289.

(185) Li, Z.; Dai, S. *Chem. Mater.* **2005**, *17*, 1717–1721.

(186) Toupin, M.; Bélanger, D. *J. Phys. Chem. C.* **2007**, *111*, 5394–5401.

(187) Allongue, P.; Delamar, M.; Desbat, B.; Fagebaume, O.; Hitmi, R.; Pinson, J.; Savéant, J.-M. *J. Am. Chem. Soc.* **1997**, *119*, 201–207.

(188) Delamar, M.; Hitmi, R.; Pinson, J.; Savéant, J.-M. *J. Am. Chem. Soc.* **1992**, *114*, 5883–5884.

(189) D'Amours, M.; Bélanger, D. *J. Phys. Chem. B* **2003**, *107*, 4811–4817.

(190) Harnisch, J. A.; Gazda, D. B.; Anderegg, J. W.; Porter, M. D. *Anal. Chem.* **2001**, *73*, 3954–3959.

(191) Saby, C.; Ortiz, B.; Champagne, G. Y.; Bélanger, D. *Langmuir* **1997**, *13*, 6805–6813.

(192) Delamar, M.; Desarmot, G.; Fagebaume, O.; Hitmi, R.; Pinson, J.; Saveant, J.-M. *Carbon* **1997**, *35*, 801–807.

(193) Ray III, K. G.; McCreery, R. L. *J. Electroanal. Chem.* **1999**, *469*, 150–158.

(194) Titirici, M.-M.; Thomas, A.; Antonietti, M. *J. Mater. Chem.* **2007**, *17*, 3412–3418.

(195) Abe, M.; Kawashima, K.; Kozawa, K.; Sakai, H.; Kaneko, K. *Langmuir* **2000**, *16*, 5059–5063.

(196) Wildgoose, G. G.; Leventis, H. C.; Davies, I. J.; Crossley, A.; Lawrence, N. S.; Jiang, L.; Jones, T. G. J.; Compton, R. G. *J. Mater. Chem.* **2005**, *15*, 2375–2382.

(197) Li, J.; Vergne, M. J.; Mowles, E. D.; Zhong, W.-H.; Hercules, D. M.; Lukehart, C. M. *Carbon* **2005**, *43*, 2883–2893.

(198) Pittman Jr., C. U.; He, G.-R.; Wu, B.; Gardner, S. D. *Carbon* **1997**, *35*, 317–331.

(199) Tamai, H.; Shiraki, K.; Shiono, T.; Yasuda, H. *J. Colloid Interface Sci.* **2006**, *295*, 299–302.

(200) Strong, W. R.; Knauff, A. R.; Fravel, B. W.; Samide, M. J. *Carbon* **2006**, *44*, 1936–1941.

(201) Cosnier, F.; Celzard, A.; Furdin, G.; Bégin, D.; Marêché, J. F.; Barrès, O. *Carbon* **2005**, *43*, 2554–2563.

(202) Budarin, V. L.; Clark, J. H.; Tavener, S. J.; Wilson, K. *Chem. Commun. (Cambridge, U. K.)* **2004**, 2736–2737.

(203) Liang, C.; Li, Z.; Dai, S. *Angew. Chem., Int. Ed.* **2008**, *47*, 3696–3717.

(204) Domingo-García, M.; Garzón, F. J. L.; Pérez-Mendoza, M. J. *J. Colloid Interface Sci.* **2002**, *248*, 116–122.

(205) Goertzen, S. L.; Thériault, K. D.; Oickle, A. M.; Tarasuk, A. C.; Andreas, H. A. *Carbon* **2010**, *48*, 1252–1261.

(206) Oickle, A. M.; Goertzen, S. L.; Hopper, K. R.; Abdalla, Y. O.; Andreas, H. A. *Carbon* **2010**, *48*, 3313–3322.

(207) Salame, I. I.; Bandosz, T. J. *J. Colloid Interface Sci.* **2001**, *2001*, 252–258.

(208) Noh, J. S.; Schwarz, J. A. *J. Colloid Interface Sci.* **1989**, *130*, 157–164.

(209) Bandosz, T. J.; Jagiello, J.; Contescu, C.; Schwarz, J. A. *Carbon* **1993**, *31*, 1193–1202.

(210) Beck, N. V.; Meech, S. E.; Norman, P. R.; Pears, L. A. *Carbon* **2002**, *40*, 531–540.

(211) Biniak, S.; Szymański, G.; Siedlewski, J.; Świątkowski, A. *Carbon* **1997**, *35*, 1799–1810.

(212) Liu, Y.-C.; McCreery, R. L. *J. Am. Chem. Soc.* **1995**, *117*, 11254–11259.

(213) Sellitti, C.; Koenig, J. L.; Ishida, H. *Carbon* **1990**, *28*, 221–228.

(214) Fryling, M. A.; Zhao, J.; McCreery, R. L. *Anal. Chem.* **1995**, *67*, 967–975.

(215) Paredes, J. I.; Martínez-Alonso, A.; Tascón, J. M. D. *Langmuir* **2003**, *19*, 7665–7668.

(216) Menéndez, J. A.; Phillips, J.; Xia, B.; Radovic, L. R. *Langmuir* **1996**, *12*, 4404–4410.

(217) Li, W.; Reichenauer, G.; Fricke, J. *Carbon* **2002**, *40*, 2955–2959.

(218) Ruiz, V.; Blanco, C.; Santamaría, R.; Ramos-Fernández, J. M.; Martínez-Escandell, M.; Sepúlveda-Escribano, A.; Rodríguez-Reinoso, F. *Carbon* **2009**, *47*, 195–200.

(219) Bakker, E. *Anal. Chem.* **2004**, *76*, 3285–3298.

(220) Ozawa, K. *Solid State Ionics* **1994**, *69*, 212–221.

(221) Cheng, F.; Tao, Z.; Liang, J.; Chen, J. *Chem. Mater.* **2008**, *20*, 667–681.

(222) Garcia-Gomez, A.; Miles, P.; Centeno, T. A.; Rojo, J. M. *Electrochem. Solid-State Lett.* **2010**, *13*, A112–A114.

(223) Walcarius, A. *Anal. Bioanal. Chem.* **2010**, *396*, 261–272.

(224) Winter, M.; Brodd, R. J. *Chem. Rev. (Washington, DC, U.S.)* **2004**, *104*, 4245–4269.

(225) Pandolfo, A. G.; Hollenkamp, A. F. *J. Power Sources* **2006**, *157*, 11–27.

(226) Mayer, S. T.; Pekala, R. W.; Kaschmitter, J. L. *J. Electrochem. Soc.* **1993**, *140*, 446–451.

(227) Moriguchi, I.; Nakahara, F.; Furukawa, H.; Yamada, H.; Kudo, T. *Electrochem. Solid-State Lett.* **2004**, *7*, A221–A223.

(228) Yamada, H.; Nakamura, H.; Nakahara, F.; Moriguchi, I.; Kudo, T. *J. Phys. Chem. C* **2007**, *111*, 227–233.

(229) Jurewicz, K.; Vix-Guterl, C.; Frackowiak, E.; Saadallah, S.; Reda, M.; Parmentier, J.; Patarin, J.; Béguin, F. *J. Phys. Chem. Solids* **2004**, *65*, 287–293.

(230) Li, H.; Xi, H. a.; Zhu, S.; Wen, Z.; Wang, R. *Microporous Mesoporous Mater.* **2006**, *96*, 357–362.

(231) Oda, H.; Yamashita, A.; Minoura, S.; Okamoto, M.; Morimoto, T. *J. Power Sources* **2006**, *158*, 1510–1516.

(232) Kim, C.-H.; Pyun, S.-I.; Shin, H.-C. *J. Electrochem. Soc.* **2002**, *149*, A93–A98.

(233) Sevilla, M.; Álvarez, S.; Centeno, T. A.; Fuertes, A. B.; Stoeckli, F. *Electrochim. Acta* **2007**, *52*, 3207–3215.

(234) Fang, B.; Binder, L. *J. Phys. Chem. B* **2006**, *110*, 7877–7882.

(235) Hussain, M.; Yun, J. S.; Ihm, S.-K.; Russo, N.; Geobaldo, F. *Ind. Eng. Chem. Res.* **2011**, *50*, 2530–2535.

(236) Dell, R. M.; Rand, D. A. J. *Understanding Batteries*; The Royal Society of Chemistry: Cambridge, 2001.

(237) Wakihara, M.; Yamamoto, O. *Lithium Ion Batteries: Fundamentals and Performance*; Wiley-VCH: Weinheim, 1998.

(238) Xu, K. *Chem. Rev. (Washington, DC, U.S.)* **2004**, *104*, 4303–4417.

(239) Ergang, N. S.; Lytle, J. C.; Lee, K. T.; Oh, S. M.; Smyrl, W. H.; Stein, A. *Adv. Mater.* **2006**, *18*, 1750–1753.

(240) Nathan, M.; Golodnitsky, D.; Yufit, V.; Strauss, E.; Ripenbein, T.; Shectman, I.; Menkin, S.; Peled, E. *J. Microelectromech. Syst.* **2005**, *14*, 879–885.

(241) Rhodes, C. P.; Long, J. W.; Pettigrew, K. A.; Stroud, R. M.; Rolison, D. R. *Nanoscale* **2011**, *3*, 1731–1740.

(242) Baggetto, L.; Niessen, R. A. H.; Roozeboom, F.; Notten, P. H. L. *Adv. Funct. Mater.* **2008**, *18*, 1057–1066.

(243) Yan, H.; Sokolov, S.; Lytle, J. C.; Stein, A.; Zhang, F.; Smyrl, W. H. *J. Electrochem. Soc.* **2003**, *150*, A1102–A1107.

(244) Ergang, N. S.; Fierke, M. A.; Wang, Z.; Smyrl, W. H.; Stein, A. *J. Electrochem. Soc.* **2007**, *154*, A1135–A1139.

(245) McCarley, R. L.; Thomas, R. E.; Irene, E. A.; Murray, R. W. *J. Electroanal. Chem.* **1990**, *290*, 79–92.

(246) Oyama, N.; Ohsaka, T.; Ohnuki, Y.; Suzuki, T. *J. Electrochem. Soc.* **1987**, *134*, 3068–3073.

(247) Rhodes, C. P.; Long, J. W.; Doescher, M. S.; Dening, B. M.; Rolison, D. R. *J. Non-Cryst. Solids* **2004**, *350*, 73–79.

(248) Zhang, F.; Passerini, S.; Owens, B. B.; Smyrl, W. H. *Electrochem. Solid-State Lett.* **2001**, *4*, A221–A223.

(249) Zheng, J. P.; Cygan, P. J.; Jow, T. R. *J. Electrochem. Soc.* **1995**, *142*, 2699–2703.

(250) Lytle, J. C.; Rhodes, C. P.; Long, J. W.; Pettigrew, K. A.; Stroud, R. M.; Rolison, D. R. *J. Mater. Chem.* **2007**, *17*, 1292–1299.

(251) Long, J. W.; Swider, K. E.; Merzbacher, C. I.; Rolison, D. R. *Langmuir* **1999**, *15*, 780–785.

(252) Ryan, J. V.; Berry, A. D.; Anderson, M. L.; Long, J. W.; Stroud, R. M.; Cepak, V. M.; Browning, V. M.; Rolison, D. R.; Merzbacher, C. I. *Nature (London, U.K.)* **2000**, *406*, 169–172.

(253) Carewska, M.; Appetecci, G. B.; Cardellini, F.; Passerini, S. *Solid State Ionics* **2001**, *139*, 211–218.

(254) Jang, J. H.; Han, S.; Hyeon, T.; Oh, S. M. *J. Power Sources* **2003**, *123*, 79–85.

(255) Balaya, P.; Li, H.; Kienle, L.; Maier, J. *Adv. Funct. Mater.* **2003**, *13*, 621–625.

(256) Li, J. X.; Ness, J. N.; Cheung, W. L. *J. Appl. Polym. Sci.* **1996**, *59*, 1733–1740.

(257) Bakker, E.; Bühlmann, P.; Pretsch, E. *Chem. Rev. (Washington, DC, U.S.)* **1997**, *97*, 3083–3132.

(258) Johnson, R. D.; Bachas, L. G. *Anal. Bioanal. Chem.* **2003**, *376*, 328–341.

(259) Bakker, E.; Bühlmann, P.; Pretsch, E. *Electroanalysis* **1999**, *11*, 915–933.

(260) Yim, H.-S.; Kibbey, C. E.; Ma, S.-C.; Kliza, D. M.; Liu, D.; Park, S.-B.; Torre, C. E.; Meyerhoff, M. E. *Biosens. Bioelectron.* **1993**, *8*, 1–38.

(261) Bakker, E.; Diamond, D.; Lewenstam, A.; Pretsch, E. *Anal. Chim. Acta* **1999**, *393*, 11–18.

(262) Lai, C.-Z.; Fierke, M. A.; Stein, A.; Bühlmann, P. *Anal. Chem.* **2007**, *79*, 4621–4626.

(263) Brett, C. M. A.; Brett, A. M. O. *Electrochemistry: Principles, Methods, and Applications*; Oxford University Press: Oxford, 1993.

(264) Nikolskii, B. P.; Materova, E. A. *Ion-Sel. Electrode Rev.* **1985**, *7*, 3–39.

(265) Bobacka, J. *Electroanalysis* **2006**, *18*, 7–18.

(266) Cadogan, A.; Gao, Z.; Lewenstam, A.; Ivaska, A. *Anal. Chem.* **1992**, *64*, 2496–2501.

(267) Fibbioli, M.; Bandyopadhyay, K.; Liu, S.-G.; Echegoyen, L.; Enger, O.; Diederich, F.; Bühlmann, P.; Pretsch, E. *Chem. Commun. (Cambridge, U.K.)* **2000**, 339–340.

(268) Cattrall, R. W.; Freiser, H. *Anal. Chem.* **1971**, *43*, 1905–1906.

(269) Lindner, E.; Cosofret, V. V.; Ufer, S.; Johnson, T. A.; Ash, R. B.; Nagle, H. T.; Neuman, M. R.; Buck, R. P. *Fresenius' J. Anal. Chem.* **1993**, *346*, 584–588.

(270) Buck, R. P. In *Ion-Selective Electrodes in Analytical Chemistry*; Freiser, H., Ed.; Plenum Press: New York and London, 1978; Vol. 1, p 1–142.

(271) Kovács, B.; Csóka, B.; Nagy, G.; Ivaska, A. *Anal. Chim. Acta* **2001**, *437*, 67–76.

(272) Gyurcsányi, R. E.; Nybäck, A.-S.; Tóth, K.; Nagy, G.; Ivaska, A. *Analyst (Cambridge, U. K.)* **1998**, *123*, 1339–1344.

(273) Gyurcsányi, R. E.; Rangisetty, N.; Clifton, S.; Pendley, B. D.; Lindner, E. *Talanta* **2004**, *63*, 89–99.

(274) Michalska, A.; Hulanicki, A.; Lewenstam, A. *Microchem. J.* **1997**, *57*, 59–64.

(275) Momma, T.; Yamamoto, M.; Komaba, S.; Osaka, T. *J. Electroanal. Chem.* **1996**, *407*, 91–96.

(276) Sutter, J.; Lindner, E.; Gyurcsányi, R. E.; Pretsch, E. *Anal. Bioanal. Chem.* **2004**, *380*, 7–14.

(277) Sutter, J.; Pretsch, E. *Electroanalysis* **2006**, *18*, 19–25.

(278) Bobacka, J.; Lindfors, T.; McCarrick, M.; Ivaska, A.; Lewenstam, A. *Anal. Chem.* **1995**, *67*, 3819–3823.

(279) Bobacka, J.; McCarrick, M.; Lewenstam, A.; Ivaska, A. *Analyst (Cambridge, U.K.)* **1994**, *119*, 1985–1991.

(280) Chumbimuni-Torres, K. Y.; Rubinova, N.; Radu, A.; Kubota, L. T.; Bakker, E. *Anal. Chem.* **2006**, *78*, 1318–1322.

(281) Lindfors, T.; Ivaska, A. *Anal. Chem.* **2004**, *76*, 4387–4394.

(282) Vázquez, M.; Bobacka, J.; Ivaska, A.; Lewenstam, A. *Sens. Actuators, B* **2002**, *82*, 7–13.

(283) Bobacka, J. *Anal. Chem.* **1999**, *71*, 4932–4937.

(284) Aquino-Binag, C. N.; Kumar, N.; Lamb, R. N. *Chem. Mater.* **1996**, *8*, 2579–2585.

(285) Faria, R. C.; Bulhões, L. O. S. *Anal. Chim. Acta* **1998**, *377*, 21–27.

(286) Lindino, C. A.; Bulhões, L. O. S. *Anal. Chim. Acta* **1996**, *334*, 317–322.

(287) Pandey, P. C.; Singh, G. *Talanta* **2001**, *55*, 773–782.

(288) Pei, Q.; Qian, R. *Electrochim. Acta.* **1992**, *37*, 1075–1081.

(289) Zhang, X.; Ogorevc, B.; Wang, J. *Anal. Chim. Acta* **2002**, *452*, 1–10.

(290) Vázquez, M.; Danielsson, P.; Bobacka, J.; Lewenstam, A.; Ivaska, A. *Sens. Actuators, B* **2004**, *97*, 182–189.

(291) Li, Y.; Qian, R. *Synth. Met.* **1993**, *53*, 149–154.

(292) Kankare, J.; Vinokurov, I. A. *Anal. Chem.* **1997**, *69*, 2337–2342.

(293) Zhao, X.; Wang, M. *Eur. Polym. J.* **2006**, *42*, 247–253.

(294) Bühlmann, P.; Pretsch, E.; Bakker, E. *Chem. Rev. (Washington, DC, U.S.)* **1998**, *98*, 1593–1687.

(295) Spichiger-Keller, U. E. *Anal. Chim. Acta* **1999**, *400*, 65–72.

(296) Bocheńska, M. *J. Mol. Struct.* **1998**, *450*, 107–115.

(297) Bernhardt, P. V.; Moore, E. G. *Aust. J. Chem.* **2003**, *56*, 239–258.

(298) Anslyn, E. V. *J. Org. Chem.* **2007**, *72*, 687–699.

(299) Lehn, J.-M. *Supramolecular Chemistry: Concepts and Perspectives*; Wiley-VCH: Weinheim, 1995.

(300) Fabbrizzi, L.; Licchelli, M.; Pallavicini, P.; Perotti, A.; Sacchi, D. *Angew. Chem., Int. Ed.* **1994**, *33*, 1975–1977.

(301) Fabbrizzi, L.; Poggi, A. *Chem. Soc. Rev.* **1995**, *24*, 197–202.

(302) Inouye, M.; Hashimoto, K.-i.; Isagawa, K. *J. Am. Chem. Soc.* **1994**, *116*, 5517–5518.

(303) Metzger, A.; Lynch, V. M.; Anslyn, E. V. *Angew. Chem., Int. Ed.* **1997**, *36*, 862–865.

(304) Wiskur, S. L.; Ait-Haddou, H.; Lavigne, J. J.; Anslyn, E. V. *Acc. Chem. Res.* **2001**, *34*, 963–972.

(305) Niikura, K.; Bisson, A. P.; Anslyn, E. V. *J. Chem. Soc., Perkin Trans. 2* **1999**, 1111–1114.

(306) Wright, A. T.; Zhong, Z.; Anslyn, E. V. *Angew. Chem., Int. Ed.* **2005**, *44*, 5679–5682.

(307) Schneider, S. E.; O'Neil, S. N.; Anslyn, E. V. *J. Am. Chem. Soc.* **2000**, *122*, 542–543.

(308) Pickup, J. C.; Hussain, F.; Evans, N. D.; Rolinski, O. J.; Birch, D. J. S. *Biosens. Bioelectron.* **2005**, *20*, 2555–2565.

(309) Mohr, G. J. *Chem. Eur. J.* **2004**, *10*, 1082–1090.

(310) Schneider, H.-J.; Yatsimirsky, A. K. *Chem. Soc. Rev.* **2008**, *37*, 263–277.

(311) Czarnik, A. W. *Chem. Biol. (Oxford, U. K.)* **1995**, *2*, 423–428.

(312) Yang, X.; Du, X.-X.; Shi, J.; Swanson, B. *Talanta* **2001**, *54*, 439–445.

(313) Winter, M.; Besenhard, J. O.; Spahr, M. E.; Novák, P. *Adv. Mater.* **1998**, *10*, 725–763.

(314) Coustier, F.; Jarero, G.; Passerini, S.; Smyrl, W. H. *J. Power Sources* **1999**, *83*, 9–14.

(315) Rhodes, C. P.; Long, J. W.; Doescher, M. S.; Fontanella, J. J.; Rolison, D. R. *J. Phys. Chem. B* **2004**, *108*, 13079–13087.

(316) Brumfield, J. C.; Goss, C. A.; Irene, E. A.; Murray, R. W. *Langmuir* **1992**, *8*, 2810–2817.

(317) Lai, C.-Z.; Joyer, M. M.; Fierke, M. A.; Petkovich, N. D.; Stein, A.; Bühlmann, P. *J. Solid State Electrochem.* **2009**, *13*, 123–128.

(318) Fierke, M. A.; Lai, C.-Z.; Bühlmann, P.; Stein, A. *Anal. Chem.* **2010**, *82*, 680–688.

(319) Diamond, D. *Anal. Chem.* **2004**, *76*, 278A–286A.

(320) Buck, R. P.; Lindner, E. *Anal. Chem.* **2001**, *73*, 88A–97A.

(321) Kurihara, K.; Nakamura, K.; Hirayama, E.; Suzuki, K. *Anal. Chem.* **2002**, *74*, 6323–6333.

(322) Ammann, D. *Ion-Selective Microelectrodes*; Springer-Verlag: Berlin, 1986.

(323) Sokalski, T.; Ceresa, A.; Zwickl, T.; Pretsch, E. *J. Am. Chem. Soc.* **1997**, *119*, 11347–11348.

(324) Mathison, S.; Bakker, E. *Anal. Chem.* **1998**, *70*, 303–309.

(325) Ion, A. C.; Bakker, E.; Pretsch, E. *Anal. Chim. Acta* **2001**, *440*, 71–79.

(326) Ceresa, A.; Bakker, E.; Hattendorf, B.; Günther, D.; Pretsch, E. *Anal. Chem.* **2001**, *73*, 343–351.

(327) Ceresa, A.; Radu, A.; Peper, S.; Bakker, E.; Pretsch, E. *Anal. Chem.* **2002**, *74*, 4027–4036.

(328) Wang, C.-Y.; Hu, X.-Y.; Leng, Z.-Z.; Jin, G.-D. *Electroanalysis* **2003**, *15*, 709–714.

(329) Malon, A.; Radu, A.; Qin, W.; Qin, Y.; Ceresa, A.; Maj-Zurawska, M.; Bakker, E.; Pretsch, E. *Anal. Chem.* **2003**, *75*, 3865–3871.

(330) Qin, W.; Zwickl, T.; Pretsch, E. *Anal. Chem.* **2000**, *72*, 3236–3240.

(331) Lindner, E.; Gyurcsányi, R. E.; Buck, R. P. *Electroanalysis* **1999**, *11*, 695–702.

(332) Pergel, E.; Gyurcsányi, R. E.; Tóth, K.; Lindner, E. *Anal. Chem.* **2001**, *73*, 4249–4253.

(333) Zwickl, T.; Sokalski, T.; Pretsch, E. *Electroanalysis* **1999**, *11*, 673–680.

(334) Sokalski, T.; Zwickl, T.; Bakker, E.; Pretsch, E. *Anal. Chem.* **1999**, *71*, 1204–1209.

(335) Sokalski, T.; Ceresa, A.; Fibbioli, M.; Zwickl, T.; Bakker, E.; Pretsch, E. *Anal. Chem.* **1999**, *71*, 1210–1214.

(336) Cattrall, R. W.; Drew, D. M.; Hamilton, I. C. *Anal. Chim. Acta* **1975**, *76*, 269–277.

(337) Schnierle, P.; Kappes, T.; Hauser, P. C. *Anal. Chem.* **1998**, *70*, 3585–3589.

(338) Dimitrakopoulos, T.; Farrell, J. R.; Iles, P. *Electroanalysis* **1996**, *8*, 391–395.

(339) Cosofret, V. V.; Erdösy, M.; Johnson, T. A.; Buck, R. P. *Anal. Chem.* **1995**, *67*, 1647–1653.

(340) Lynch, A.; Diamond, D.; Leader, M. *Analyst (Cambridge, U. K.)* **2000**, *125*, 2264–2267.

(341) Pandey, P. C.; Upadhyay, S.; Singh, G.; Prakash, R.; Srivastava, R. C.; Seth, P. K. *Electroanalysis* **2000**, *12*, 517–521.

(342) Fibbioli, M.; Bandyopadhyay, K.; Liu, S.-G.; Echegoyen, L.; Enger, O.; Diederich, F.; Gingery, D.; Bühlmann, P.; Persson, H.; Suter, U. W.; Pretsch, E. *Chem. Mater.* **2002**, *14*, 1721–1729.

(343) Michalska, A.; Konopka, A.; Maj-Zurawska, M. *Anal. Chem.* **2003**, *75*, 141–144.

(344) Konopka, A.; Sokalski, T.; Michalska, A.; Lewenstam, A.; Maj-Zurawska, M. *Anal. Chem.* **2004**, *76*, 6410–6418.

(345) Michalska, A.; Dumańska, J.; Maksymiuk, K. *Anal. Chem.* **2003**, *75*, 4964–4974.

(346) Michalska, A.; Appaih-Kusi, C.; Heng, L. Y.; Walkiewicz, S.; Hall, E. A. H. *Anal. Chem.* **2004**, *76*, 2031–2039.

(347) Sutter, J.; Radu, A.; Peper, S.; Bakker, E.; Pretsch, E. *Anal. Chim. Acta* **2004**, *523*, 53–59.

(348) Heng, L. Y.; Toth, K.; Hall, E. A. H. *Talanta* **2004**, *63*, 73–87.

(349) Konopka, A.; Sokalski, T.; Lewenstam, A.; Maj-Zurawska, M. *Electroanalysis* **2006**, *18*, 2232–2242.

(350) Růžička, J.; Lamm, C. G.; Tjell, J. C. *Anal. Chim. Acta* **1972**, *62*, 15–28.

(351) Fiedler, U.; Růžička, J. *Anal. Chim. Acta* **1973**, *67*, 179–193.

(352) Crespo, G. A.; Macho, S.; Bobacka, J.; Rius, F. X. *Anal. Chem.* **2009**, *81*, 676–681.

(353) Crespo, G. A.; Macho, S.; Rius, F. X. *Anal. Chem.* **2008**, *80*, 1316–1322.

(354) Mousavi, Z.; Bobacka, J.; Lewenstam, A.; Ivaska, A. *J. Electroanal. Chem.* **2009**, *633*, 246–252.

(355) Zhu, J.; Qin, Y.; Zhang, Y. *Electrochem. Commun.* **2009**, *11*, 1684–1687.

(356) Fouskaki, M.; Chaniotakis, N. *Analyst (Cambridge, U.K.)* **2008**, *133*, 1072–1075.

(357) van der Pauw, L. J. *Philips Tech. Rev.* **1958/59**, *20*, 220–224.

(358) Morf, W. E. *The Principles of Ion-Selective Electrodes and of Membrane Transport*; Elsevier: New York, 1981.

(359) Meier, P. C. *Anal. Chim. Acta* **1982**, *136*, 363–368.

(360) Fibbioli, M.; Morf, W. E.; Badertscher, M.; De Rooij, N. F.; Pretsch, E. *Electroanalysis* **2000**, *12*, 1286–1292.

(361) Environmental Protection Agency In: EPA Drinking Water Criteria Document for Silver; EPA, Washington, DC, 1989, EPA CASRN 7440-7422-7444.

(362) Bobacka, J.; Lahtinen, T.; Nordman, J.; Häggström, S.; Rissanen, K.; Lewenstam, A.; Ivaska, A. *Electroanalysis* **2001**, *13*, 723–726.

(363) Bobacka, J.; Väänänen, V.; Lewenstam, A.; Ivaska, A. *Talanta* **2004**, *63*, 135–138.

(364) Oesch, U.; Simon, W. *Anal. Chem.* **1980**, *52*, 692–700.

(365) Fu, B.; Bakker, E.; Yun, J. H.; Yang, V. C.; Meyerhoff, M. E. *Anal. Chem.* **1994**, *66*, 2250–2259.

(366) Ceresa, A.; Sokalski, T.; Pretsch, E. *J. Electroanal. Chem.* **2001**, *501*, 70–76.

(367) Meier, P. C.; Morf, W. E.; Läubli, M.; Simon, W. *Anal. Chim. Acta* **1984**, *156*, 1–8.

(368) Amemiya, S.; Bühlmann, P.; Pretsch, E.; Rusterholz, B.; Umezawa, Y. *Anal. Chem.* **2000**, *72*, 1618–1631.

(369) Szigeti, Z.; Malon, A.; Vigassy, T.; Csokai, V.; Grün, A.; Wygladacz, K.; Ye, N.; Xu, C.; Chebny, V. J.; Bitter, I.; Rathore, R.; Bakker, E.; Pretsch, E. *Anal. Chim. Acta* **2006**, *572*, 1–10.

(370) Tóth, K.; Gráf, E.; Horvai, G.; Pungor, E.; Buck, R. P. *Anal. Chem.* **1986**, *58*, 2741–2744.

(371) Ye, Q.; Borbély, S.; Horvai, G. *Anal. Chem.* **1999**, *71*, 4313–4320.

(372) De Marco, R.; Veder, J.-P.; Clarke, G.; Nelson, A.; Prince, K.; Pretsch, E.; Bakker, E. *Phys. Chem. Chem. Phys.* **2008**, *10*, 73–76.

(373) Pejcic, B.; De Marco, R. *Electrochim. Acta* **2006**, *51*, 6217–6229.

(374) Orazem, M. E.; Tribollet, B. *Electrochemical Impedance Spectroscopy*; Wiley-Interscience: Hoboken, NJ, 2008.

(375) Vanysek, P. *ECS Trans.* **2008**, *13*, 101–113.

(376) McCreery, R. L. *Chem. Rev. (Washington, DC, U.S.)* **2008**, *108*, 2646–2687.

(377) Lindner, E.; Gyurcsanyi, R. E. *J. Solid State Electrochem.* **2009**, *13*, 51–68.

(378) Fierke, M. A.; Olson, E. J.; Bühlmann, P.; Stein, A. *ACS Appl. Mater. Interfaces* **2012**, *4*, 4731–4739.

(379) Yinon, J. *Trends Anal. Chem.* **2002**, *21*, 292–301.

(380) Steinfield, J. I.; Wormhoudt, J. *Annu. Rev. Phys. Chem.* **1998**, *49*, 203–232.

(381) Yinon, J. *Anal. Chem.* **2003**, *75*, 99A–105A.

(382) Moore, D. S. *Rev. Sci. Instrum.* **2004**, *75*, 2499–2512.

(383) Harper, R. J.; Almirall, J. R.; Furton, K. G. *Talanta* **2005**, *67*, 313–327.

(384) Phelan, J. M.; Barnett, J. L. *Proc. SPIE* **2002**, *4742*, 532–543.

(385) Sohn, H.; Sailor, M. J.; Magde, D.; Trogler, W. C. *J. Am. Chem. Soc.* **2003**, *125*, 3821–3830.

(386) Naddo, T.; Che, Y.; Zhang, W.; Balakrishnan, K.; Yang, X.; Yen, M.; Zhao, J.; Moore, J. S.; Zang, L. *J. Am. Chem. Soc.* **2007**, *129*, 6978–6979.

(387) Eastwood, D.; Fernandez, C.; Yoon, B. Y.; Sheaff, C. N.; Wai, C. M. *Appl. Spectrosc.* **2006**, *60*, 958–963.

(388) Forzani, E. S.; Lu, D.; Leright, M. J.; Aguilar, A. D.; Tsow, F.; Iglesias, R. A.; Zhang, Q.; Lu, J.; Li, J.; Tao, N. *J. Am. Chem. Soc.* **2009**, *131*, 1390–1391.

(389) Rodríguez, M. C.; Monti, M. R.; Argaraña, C. E.; Rivas, G. A. *Talanta* **2006**, *68*, 1671–1676.

(390) Pinnaduwage, L. A.; Thundat, T.; Hawk, J. E.; Hedden, D. L.; Britt, P. F.; Houser, E. J.; Stepnowski, S.; McGill, R. A.; Bubb, D. *Sens. Actuators, B* **2004**, *99*, 223–229.

(391) Albert, K. J.; Myrick, M. L.; Brown, S. B.; James, D. L.; Milanovich, F. P.; Walt, D. R. *Environ. Sci. Technol.* **2001**, *35*, 3193–3200.

(392) Masunaga, K.; Hayama, K.; Onodera, T.; Hayashi, K.; Miura, N.; Matsumoto, K.; Toko, K. *Sens. Actuators, B* **2005**, *108*, 427–434.

(393) Nie, D.; Li, P.; Zhang, D.; Zhou, T.; Liang, Y.; Shi, G. *Electrophoresis* **2010**, *31*, 2981–2988.

(394) Saravanan, N. P.; Venugopalan, S.; Senthilkumar, N.; Santhosh, P.; Kavita, B.; Prabu, H. G. *Talanta* **2006**, *69*, 656–662.

(395) Honeychurch, K. C.; Hart, J. P.; Pritchard, P. R. J.; Hawkins, S. J.; Ratcliffe, N. M. *Biosens. Bioelectron.* **2003**, *19*, 305–312.

(396) Agüí, L.; Vega-Montenegro, D.; Yáñez-Sedeño, P.; Pingarrón, J. M. *Anal. Bioanal. Chem.* **2005**, *382*, 381–387.

(397) Huang, M.-J.; Leszczynski, J. *J. Mol. Struct.: THEOCHEM* **2002**, *592*, 105–113.

(398) Shankaran, D. R.; Kawaguchi, T.; Kim, S. J.; Matsumoto, K.; Toko, K.; Miura, N. *Anal. Bioanal. Chem.* **2006**, *108*, 1313–1320.

(399) Walcarius, A. *Trends Anal. Chem.* **2012**, *38*, 79–97.

(400) Wang, Z.; Fierke, M. A.; Stein, A. *J. Electrochem. Soc.* **2008**, *155*, A658–A663.

(401) Zhang, T.; Lai, C.-Z.; Fierke, M. A.; Stein, A.; Bühlmann, P. *Anal. Chem.* **2012**, *84*, 7771–7778.

(402) Bühlmann, P.; Nishizawa, S.; Xiao, K. P.; Umezawa, Y. *Tetrahedron* **1997**, *53*, 1647–1654.

(403) Olson, E. J.; Xiong, T. T.; Cramer, C. J.; Bühlmann, P. *J. Am. Chem. Soc.* **2011**, *133*, 12858–12865.

(404) Boswell, P. G.; Bühlmann, P. *J. Am. Chem. Soc.* **2005**, *127*, 8958–8959.

(405) Nishida, H.; Takada, N.; Yoshimura, M.; Sonoda, T.; Kobayashi, H. *Bull. Chem. Soc. Jpn.* **1984**, *57*, 2600–2604.

(406) Yakelis, N. A.; Bergman, R. G. *Organometallics* **2005**, *24*, 3579–3581.

(407) Hill, M. G.; Lamanna, W. M.; Mann, K. R. *Inorg. Chem.* **1991**, *30*, 4687–4690.

(408) Yu, S. S. C.; Tan, E. S. Q.; Jane, R. T.; Downard, A. J. *Langmuir* **2007**, *23*, 11074–11082.

(409) Hurley, B. L.; McCreery, R. L. *J. Electrochem. Soc.* **2004**, *151*, B252–B259.

(410) Doppelt, P.; Hallais, G.; Pinson, J.; Podvorica, F.; Verneyre, S. *Chem. Mater.* **2007**, *19*, 4570–4575.

(411) Brooksby, P. A.; Downard, A. J. *J. Phys. Chem. B* **2005**, *109*, 8791–8798.

(412) Ortiz, B.; Saby, C.; Champagne, G. Y.; Bélanger, D. *J. Electroanal. Chem.* **1998**, *455*, 75–81.

(413) Boehm, H. P. In *Graphite and Precursors*; Delhaes, P., Ed.; Gordon and Breach Science Publishers: Amsterdam, The Netherlands, 2001; Vol. 1, p 141−178.

(414) Prest, J. W. M.; Mosher, R. A. In *Colloids and Surfaces in Reprographic Technology*; Hair, M., Croucher, M. D., Eds.; American Chemical Society: Washington, 1982, p 225–247.

(415) Liu, L.; Qin, Y.; Guo, Z.-X.; Zhu, D. *Carbon* **2003**, *41*, 331−335.

(416) Sainsbury, T.; Fitzmaurice, D. *Chem. Mater.* **2004**, *16*, 3780−3790.

(417) Shaffer, M. S. P.; Fan, X.; Windle, A. H. *Carbon* **1998**, *36*, 1603−1612.

(418) Pretsch, E.; Bühlmann, P.; Badertscher, M. *Structure Determination of Organic Compounds: Tables of Spectral Data*; 4th ed.; Springer: Berlin, 2009.

(419) Silverstein, R. M.; Webster, F. X. *Spectrometric Identification of Organic Compounds*; 6th ed.; John Wiley & Sons: Hoboken, 1998.

(420) Krausa, M.; Doll, J.; Schorb, K.; Böke, W.; Hambitzer, G. *Propellants, Explos., Pyrotech.* **1997**, *22*, 156–159.

(421) Zhang, H.-X.; Zhang, J.-H. *Can. J. Chem.* **2011**, *89*, 8−12.

(422) Zang, J.; Guo, C. X.; Hu, F.; Yu, L.; Li, C. M. *Anal. Chim. Acta* **2011**, *683*, 187–191.

(423) Zhang, H.-X.; Cao, A.-M.; Hu, J.-S.; Wan, L.-J.; Lee, S.-T. *Anal. Chem.* **2006**, *78*, 1967−1971.

(424) Fry, A. J. *J. Electroanal. Chem.* **2003**, *546*, 35–39.

(425) Helfrick, J. J. C.; Bottomley, L. A. *Anal. Chem.* **2009**, *81*, 9041−9047.

(426) Bard, A. J.; Faulkner, L. R. *Electrochemical Methods: Fundamentals and Applications*; 2nd ed.; Wiley: New York, 2001.

(427) O'Dea, J. J.; Osteryoung, J.; Lane, T. *J. Phys. Chem.* **1986**, *90*, 2761−2764.

(428) O'Dea, J. J.; Osteryoung, J.; Osteryoung, R. A. *Anal. Chem.* **1981**, *53*, 695−701.

(429) O'Dea, J. J.; Osteryoung, J.; Osteryoung, R. A. *J. Phys. Chem.* **1983**, *87*, 3911–3918.

(430) O'Dea, J. J.; Wikiel, K.; Osteryoung, J. *J. Phys. Chem.* **1990**, *94*, 3628−3636.

(431) Chuang, M.-C.; Windmiller, J. R.; Santhosh, P.; Ramírez, G. V.; Galik, M.; Chou, T.-Y.; Wang, J. *Electroanalysis* **2010**, *22*, 2511−2518.

(432) Bozic, R. G.; West, A. C.; Levicky, R. *Sens. Actuators, B* **2008**, *133*, 509−515.

(433) Osteryoung, J. G.; Osteryoung, R. A. *Anal. Chem.* **1985**, *57*, 101A−110A.

(434) Chen, L. D.; Lai, C.-Z.; Granda, L. P.; Fierke, M. A.; Mandal, D.; Stein, A.; Gladysz, J. A.; Bühlmann, P. *Anal. Chem.* **2013**, *in press*, dx.doi.org/10.1021/ac401424j.

(435) Biener, J.; Stadermann, M.; Suss, M.; Worsley, M. A.; Biener, M. M.; Rose, K. A.; Baumann, T. F. *Energy Environ. Sci.* **2011**, *4*, 656−667.

(436) Fischer, U.; Salinger, R.; Bock, V.; Petricevic, R.; Fricke, J. *J. Porous Mater.* **1997**, *4*, 281−285.

Appendix A

Investigation of Conductivity of Three-Dimensionally Ordered Macroporous Carbon

A.1. Method of Conductivity Measurement

The conductivity of 3DOM carbon monoliths was measured using the van der Pauw method developed to allow for the analysis of materials with arbitrary shape (but uniform thickness).[357] In this method, the 3DOM carbon monolith (typically square or rectangular in shape, and polished with fine grit sand paper to ensure a uniform thickness), was contacted at the four corners with copper wires. The electrical connection was improved by addition of colloidal silver at the contact points. The other end of each copper wire was affixed to the edges of a substrate, allowing for electrical connections to be made with alligator clips connected to an Arbin battery cycler. The substrate was typically a glass plate (approximately 10 cm × 15 cm). Copper tape (with adhesive on one side) was affixed to the edges of the plate, and the copper wires were wound into a flat coil and soldered to the copper tape to ensure a good electrical connection. The contact points were labeled M, N, O, and P around the monolith (with M and O at opposite corners). Current was applied at point M and taken off at point N, and the potential difference was measured between O and P. A current step program was used, with currents of 1 mA to 10 mA (step size of 1 or 2 mA) applied for one minute each, and the potential measured at least twice for each step. The alligator clip connections were then moved to allow the same current step program to be used, but with the current applied from N to O and the potential difference being measured between M and P. The resistances, R, across the carbon monolith can be defined by

$$R_{MN,OP} = \frac{V_P - V_O}{i_{MN}}$$

and

$$R_{NO,PM} = \frac{V_M - V_P}{i_{NO}}$$

where the potential differences *(V_P – V_O)* and *(V_M – V_P)* are measured in volts, and the current applied (i_{MN} and i_{NO}) are measured in amperes. If the thickness, *d*, of the monolith is measured in cm, the resistivity, ρ, can be determined by

$$e^{\left(-\frac{\pi d}{\rho} R_{MN,OP}\right)} + e^{\left(-\frac{\pi d}{\rho} R_{NO,PM}\right)} = 1$$

with units of Ω·cm. The conductivity (with units of $\mathrm{S \cdot cm^{-1}}$) is calculated by taking the inverse of the resistivity.

A.2. Conductivity of 3DOM Carbon Samples

A.2.1. Variation of Composite Drying Time

The relationship between drying time of 3DOM carbon and electrical conductivity was examined. 3DOM carbon samples were prepared as described in Chapter 3 (section 3.2.2.) with a small variation. After the resorcinol-formaldehyde/colloidal crystal composites were heated for 3 days at 85 °C in a closed container to allow for crosslinking, the containers were opened and returned to the oven at 85 °C for varying amounts of time (from 0 to 20 hours). After carbonization of each sample at 900 °C under flowing nitrogen, the electrical conductivity of the samples was then measured as described above. The results are summarized in Table A.1.

The highest conductivity was observed in the samples that were not dried prior to pyrolysis. Drying in an open container removes excess solvent rapidly and causes the resorcinol-formaldehyde to crack within the colloidal crystal template. As the drying time is increased, the amount of cracks increases. After pyrolysis, the samples with more cracks collapse more than those with fewer cracks, resulting in a slightly more dense structure. This more dense structure has better electrical conductivity than a less dense structure. This helps to explain why the samples with drying times over two hours have higher conductivity values than the sample dried for 0.5 hours. However, the sample that was not dried had the highest conductivity, probably because fewer cracks formed and the monolith maintained good connectivity.[435]

Table A.1. Relationship between drying time of 3DOM carbon at 85 °C before pyrolysis and the electrical conductivity of the samples.

Drying Time (h)	Conductivity ($S \cdot cm^{-1}$)
0	0.338
0.5	0.230
2.0	0.251
5.0	0.261
20	0.260

The effect of varying the drying time before carbonization on the surface area of the 3DOM carbon monoliths was also investigated (Table A.2.). As the drying time increased from zero hours to two hours, the surface area increased, mostly due to the formation of micropores, because of the cracks that form during solvent evaporation. When the drying time was longer than two hours, the surface area began to decrease, likely due to the partial collapse of the weakened structure caused by cracking.

Table A.2. BET surface area, mesopore surface area, micropore surface area, mesopore volume, micropore volume, and average pore diameter of 3DOM carbon samples dried for varying times at 85 °C before pyrolysis. These data were collected by Zhiyong Wang.

drying time (h)	BET surface area ($m^2 \cdot g^{-1}$)	mesopore surface area ($m^2 \cdot g^{-1}$)	micropore surface area ($m^2 \cdot g^{-1}$)	mesopore volume ($cm^3 \cdot g^{-1}$)	micropore volume ($cm^3 \cdot g^{-1}$)	average pore diameter (nm)
0	247	25	192	0.031	0.088	1.8
0.5	272	30	219	0.035	0.100	1.7
2	338	29	283	0.034	0.130	1.7
5	304	33	242	0.040	0.111	1.7
20	295	23	238	0.027	0.109	1.6

A.2.1. Variation of Carbonization Temperature

3DOM carbon samples were prepared as described in Section 3.2.2. Since the highest conductivity was achieved without drying the resorcinol-formaldehyde/colloidal crystal composites in an open container at 85 °C, the samples used for all future studies were not dried. A large batch of resorcinol-formaldehyde/colloidal crystal composites was prepared, and the pyrolysis temperature was varied. The ramp rate (5 $°C \cdot min^{-1}$), dwell time (2 h), and nitrogen flow rate (0.5 L·min^{-1}) were kept constant for all samples, while the pyrolysis temperature was varied from 600 to 1100 °C. The conductivity of each sample was then measured (Table A.3.).

When pyrolyzed at 600 °C, the samples had a conductivity too low to be measured. As the pyrolysis temperature increased up to 1000 °C, the conductivity of the samples continued to increase, likely because the number of organic functional groups in the material decreased, creating a more dense graphite-like structure.[126,436] Once the samples were heated above 1000 °C, the conductivity began to decrease.

Table A.3. Relationship between pyrolysis temperature of 3DOM carbon monoliths and the electrical conductivity of the samples.

Pyrolysis temperature (°C)	**Conductivity (S·cm^{-1})**
600	n/a[a]
650	0.050
700	0.343
750	0.509
800	0.556
850	0.579
900	0.571
950	0.574
1000	0.604
1050	0.572
1100	0.553

[a]Conductivity of the sample was too small to be measured.